THE ENERGY TRANSFER DUE TO AIR-INPUT, NON-LINEAR WAVE-WAVE INTERACTION AND WHITE-CAP DISSIPATION ASSOCIATED WITH WIND-GENERATED WAVES

by

Hong-Ye Wu

En Yun Hsu

Robert L. Street

D D C

RECEIVED

APR 14 1977

C

February 1977

Department of CIVIL ENGINEERING
STANFORD UNIVERSITY

Department of Civil Engineering

Stanford University

Stanford, California

THE ENERGY TRANSFER DUE TO AIR-INPUT, NON-LINEAR WAVE-WAVE INTERACTION AND WHITE-CAP DISSIPATION ASSOCIATED WITH WIND-GENERATED WAVES.
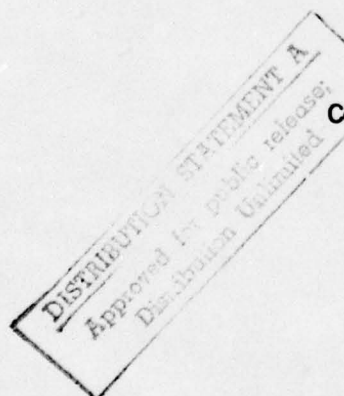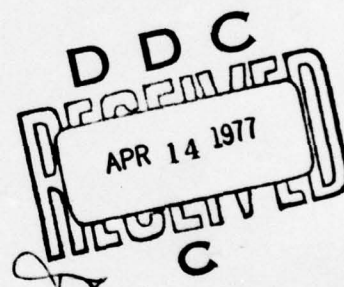
by

Hong-Ye Wu

En Yun Hsu

Robert L. Street

D D C
APR 14 1977

Technical Report No. 207

TR

175p.

February 1977

ABSTRACT

Miles' theory is unsatisfactory for the prediction of ocean wave
growth under wind action. Hasselmann's nonlinear wave-wave inter-
actions theory may offer another physical mechanism for constructing
a reasonable wave prediction model. An experimental program was
designed to investigate this possibility in the context of the momem-
tum and energy transfer from wind to waves, nonlinear wave-wave
interactions and white-capping dissipation. The wind field (mean
velocity profiles and fluctuating pressure and velocity components)
and wave field (wave height) were measured simultaneously in a fixed
reference frame and as a function of fetch along the Stanford wind-
wave channel under the conditions of steady wind and stationary wave
spectrum. All the data were obtained 5 mm above the highest point of
the wind waves for five stations (3 m apart on average) and at three
wind speeds (7.09, 8.01 and 8.88 m/sec). The wave height, fluctuating
pressure and velocity components were measured by a capacitance wave
height gauge, a crystal pressure transducer and a cross hot film probe,
respectively.

The normalized parameters of a wave field such as spectral peak
frequency $\hat{f}_m$, total energy $\hat{\epsilon}$ and the Phillips equilibrium constant α
of the wave spectrum were found to be fetch and wind speed dependent.
The power spectra of turbulent velocity components in the inertial sub-
range were consistent with Kolmogorov $-5/3$ power law. The small scale
structure of the power spectra of turbulent velocities seemed to be
wind speed dependent but fetch independent.

iii

The energy and momentum transfer from wind to waves were confirmed to be dominated by the normal pressure acting on the wave surface. In addition, the oscillating wave-associated turbulent stresses accounted for about 30% of the total momentum transferred into waves, but made a negligible contribution to the energy transfer from wind to waves. The average ratio of momentum transferred into waves over the total momentum transferred across the wind-wave interface was found to be about 0.65. The remaining 35% of the total momentum transfer goes directly to currents.

Based on the experimental results, Hasselmann's nonlinear wave-wave interaction theory appears to be valid. Barnett's approximate parametric equation for calculating the energy transfer of nonlinear wave-wave interaction and Hasselmann's white-capping dissipation model were also verified and appeared to be applicable in the relatively low and intermediate frequency region of a wave spectrum for a normalized fetch range of $100 < \hat{x} < 500$.

A method of modifying Barnett's parametric equation representing the nonlinear wave-wave interaction in the relatively high frequency region was suggested. Based on the results of overall energy balance of a gravity wind wave spectrum, the nonlinear wave-wave interaction mechanism was confirmed to play a dominant role in the energy transfer processes after the wave spectrum is generated.

iv

ACKNOWLEDGEMENTS

v

TABLE OF CONTENTS

LIST OF FIGURES

LIST OF TABLES

NOMENCLATURE

c	phase speed of wave $(=g/\omega)$ (cm/sec)
c_p	wave speed of the peak frequency of the wave spectrum (cm/sec)
Co_{xy}	cospectrum of variables x and y
d	a constant for a given wave state in Hasselmann's white capping dissipation model defined by equation (2.21)
D	transfer coefficient defined by equations (4.9) and (4.10) of Hasselmann's (1962) paper
$D'(\theta)$	normalized directional spreading factor
e	energy parameter of Barnett's parametric equation (cm^2)
E	voltage output of the Constant Temperature Anemometer (volt)
$E(f)$	one-dimensional wave spectrum (cm^2/Hz)
$E'(k)$	wave-number energy spectrum
f	frequency (Hz)
f_m	peak frequency of wave spectrum (Hz)
$\tilde{f}_m$	normalized peak frequency of wave spectrum $(= f_m \, u_{10}/g)$
$\hat{f}_m$	normalized peak frequency of wave spectrum $(= f_m \, u_*/g)$
f_o	mean frequency parameter of Barnett's parametric equation (Hz)
f_{so}	the beginning frequency at which the net energy and momentum transfer equal zero (Hz)
$f(k,\theta)$	two-dimensional wave spectrum defined by equation (2.12)
$F(f,\theta)$	two-dimensional wave spectrum $(cm^2/Hz - radian)$

g	gravitational acceleration $(= 980.66 \text{ cm/sec}^2)$
$h(t)$	transfer function of the modified system of crystal pressure transducer
$H(f)$	Fourier transform of the transfer function $h(t)$
k	wave number (cm^{-1})
$\bar{k}_x$	the average value of wave number k_x integrated over the normalized directional distribution of $E(f)$ (cm^{-1})
M_c, M_w	mean momentum transfer from wind to currents and waves (dyne/cm^2)
n_α, n_ϵ, n_f	exponent of $\hat{x}$ corresponding to α, $\hat{\epsilon}$ and $\hat{f}_m$
p, $\tilde{p}$	desired time signals of total and wave-induced normal pressure (dyne/cm^2)
p_m, $\tilde{p}_m$	measured time signals of total and wave-induced normal pressure (dyne/cm^2)
P, $\tilde{P}$	Fourier transform of p and $\tilde{p}$
P_m, $\tilde{P}_m$	Fourier transform of p_m and $\tilde{p}_m$
Qu_{xy}	quadrature spectrum of variables x and y
R_{xy}	coherence between variables x and y
S_{ds}, S_{in}, S_{nl}	one-dimensional (frequency dependent) rate of energy transfer of white-capping, air-input and nonlinear wave-wave interaction $(\text{erg-cm}^{-2}\text{-sec}^{-1})$
S	one-dimensional net rate of energy transfer $(\text{erg-cm}^{-2}\text{-sec}^{-1})$
S', S'_{ds}, S'_{in}, S'_{nl}	two-dimensional (frequency and direction dependent) rate of energy transfer corresponding to S, S_{ds}, S_{in} and S_{nl}
S'_{re}	two-dimensional rate of energy transfer associated with mean current field $(\text{erg-cm}^{-2}\text{-sec}^{-1})$

$\hat{S}_{ds}$, $\hat{S}_{n1}$	experimental results of S_{ds} and S_{n1} (erg-cm^{-2}-sec^{-1})
S_{ds}^{hf}, S_{in}^{hf}, S_{n1}^{hf}	rate of energy transfer of white-capping, air-input and nonlinear wave-wave interaction in the high frequency region (erg-cm^{-2}-sec^{-1})
$S_{in}''(t)$	energy transfer from wind to waves
$S_{ds}''(k)$	Hasselmann's white-capping dissipation wave-number spectrum defined by equation (2.20)
$S_x(f)$	power spectrum of variable x
$S_{xy}(f)$	cross spectrum of variables x and y
t	time (sec.)
T	transfer function defined by equation (2.13)
u, $\bar{u}$, $\tilde{u}$, u'	time signals of total, mean, wave-induced and background turbulent horizontal velocity component (cm/sec)
u_∞	free stream velocity (cm/sec)
u_*	friction velocity (cm/sec)
u_5, u_{10}	mean velocities above five and ten meters of the water surface (cm/sec)
U, $\tilde{U}$	Fourier transform of u and $\tilde{u}$
U_{eff}	effective velocity normal to the hot film (cm/sec)
$\tilde{U}\tilde{U}$	Fourier transform of $\tilde{u}^2$
v, $\tilde{v}$, v'	time signals of total, wave-induced and background turbulent vertical velocity component (cm/sec)
V, $\tilde{V}$	Fourier transform of v and $\tilde{v}$
$\vec{V}(f,\theta)$	group velocity vector (cm/sec)
$\overline{V}_x(f)$	mean group velocity in x-direction (cm/sec)
x	fetch measured from the junction of flate plate and water surface (cm)
$\tilde{x}$	normalized fetch $(= xg/u_{10}^2)$

$\hat{x}$	normalized fetch $(= xg/u_*^2)$
$\vec{x}$	vector space (cm)
$X^*(f)$	conjugate Fourier component of $X(f)$
$\tilde{X}(f)$, $X'(f)$	Fourier transform of $\tilde{x}(t)$ and $x'(t)$
$x(t)$, $y(t)$	any variables in time domain
$X(f)$, $Y(f)$	Fourier transform of $x(t)$ and $y(t)$

Greek symbols

α	Phillips equilibrium constant of wave spectrum
α'	Phillips equilibrium constant of wave spectrum $(= 16 \cdot \pi^4 \cdot \alpha)$
β	angle between $\vec{k}_2$ and $(\vec{k}_1 - \vec{k}_4)$ (radian)
γ	ratio of momentum transferred into waves over total momentum transfer across the wind-wave interface
γ_E	ratio of energy transferred into waves over total energy transfer across the wind-wave interface
γ'	damping factor in Hasselmann's white-capping dissipation model $(= d (2\pi f)^2)$
Γ, Γ'	one and two dimensional functions in Barnett's parametric equation defined by equations (2.18) and (2.15)
Δp	pressure difference from the pitot-static tube measured across the Pace pressure transducer (psi)
ϵ	total wave energy $(= \int E(f) \, df)$ (cm^2)
$\tilde{\epsilon}$	normalized total wave energy $(= \epsilon g^2/u_{10}^4)$
$\hat{\epsilon}$	normalized total wave energy $(= \epsilon g^2/u_*^4)$
η	water surface (wave) elevation (cm)
$\pi(f)$	Fourier transform of η

$\pi^*(f)$	conjugate Fourier component of $\pi(f)$
θ	directional angle measured from north (radian)
θ_o	mean direction parameter of Barnett's parametric equation (radian)
θ_{xy}	phase angle between variables x and y (degree)
κ	von Karman constant ($= 0.4$)
λ	a linear factor between $\tilde{X}(f)$ and $\pi(f)$
ν	kinematic viscosity (cm^2/sec)
ρ_a	density of air (gm/cm^3)
ρ_w	density of water (gm/cm^3)
$\tau,\ \tau'$	one and two dimensional functions in Barnett's parametric equation defined by equations (2.19) and (2.16)
$\bar{\tau}_{ds}^{hf},\ \bar{\tau}_{in}^{hf},\ \bar{\tau}_{nl}^{hf}$	mean momentum transfer due to white-capping dissipation, air-input and nonlinear wave-wave interaction in the high frequency region ($dyne/cm^2$)
τ_w	mean momentum transfer from wind to waves due to normal pressure acting on wave surface ($dyne/cm^2$)
ϕ	phase angle of the transfer function $H(f)$ of the modified system of crystal pressure transducer (degree)
ω	radiant frequency ($= 2\pi f$) (radian $-$ Hz)

I. INTRODUCTION

1.1 History and Motivation

In recent years many scientists from varied backgrounds have been working on problems of wind wave generation. Although important advances have been made in the wind wave field during the last twenty years, a basic understanding of the dynamical processes occurring at the air-sea interface has not been achieved. The difficulties which impede the progress of the air-sea interaction problem are the lack of fundamental knowledge of the nature of interaction between the turbulence in the air stream and the perturbed water surface, and the complex and elusive nature of the non-linear water wave-wave interactions. In addition, accurate experimental data is limited. Therefore, a complete theory covering all the stages of wind wave generation processes has not yet been established.

Ideally, a comprehensive theory of wind wave generation should give adequate predictions during the various stages of wave growth for a given fetch, wind speed, and direction. In other words, a complete theory should be able to determine the state of the sea for a given wind field. The dynamical wave theory is concerned with the local interactions of the wave field in a coupled ocean-atmosphere system. That the wind-wave problem is similar to that of an instability between fluids with a density discontinuity and moving relative to each other was first suggested by Helmholtz (1868). The problem was treated in more detail by Thomson (Lord Kelvin, 1871). The well known "Kelvin-Helmholtz Instability" was the first theory to explain the wind-wave

-1-

generation. The problem was further studied by Jeffrey (1925), Wuest (1949), Lock (1954), Eckart (1953) and Ursell (1956). Recently, the most significant contributions to solution of this problem were Phillips' (1957) and Miles' (1957) theories of wave generation which considered the momentum transfer from the wind field into the waves. Phillips (1960) and Hasselmann (1960, 1962, 1963) made further contributions to the nonlinear wave-wave interaction theory which considered the energy transfer among different wave components in a wave spectrum.

Phillips' (1957) linear theory assumed that the water motions are inviscid, irrotational, small amplitude, two-dimensional, and the excitations of the water surface are not affected by the wave-induced perturbation in the air. This so-called "resonance model" was constructed by considering turbulent wind flow over a water surface which is initially flat. The turbulent pressure fluctuations in the wind field generate oscillations of the water travelling in all directions and having all the wave numbers appearing in the air pressure spectrum. When a water wave's speed matches with the speed of translation of the corresponding air pressure fluctuation, the wave will resonate with the pressure field and grow as long as the pressure fluctuations retain their phase relative to the wave. This model results in a linear growth of the wave spectrum with time in the initial growth stage and gives order of magnitude agreement with the observed wave growth. The model becomes invalid when the wave amplitude is sufficiently large, since the neglected wave-induced perturbation in the air should be taken into account for the later stage of wave growth.

Miles (1957) assumed an incompressible, inviscid air shear flow

over single frequency progressive water waves. He considered the feed-
back of the wave-induced velocities and pressure, but the turbulence in
the air was neglected except its role in establishing the turbulent
logrithmic velocity profile. The water motion is assumed to be invis-
cid, irrotational, two-dimensional and of small amplitude. The
governing equations for the wave-induced perturbations in the air stream
are exactly the same as those in the laminar instability theory (Orr-
Sommerfeld equation). The theoretical result is that the momentum
transferred to the waves by the action of the wave-induced Reynolds
stresses working against the mean velocity gradient is evaluated inside
the critical layer where the mean wind velocity equals the wave propaga-
tion speed. The theory is applicable for those wave components whose
critical layer lies outside the viscous sublayer and in the region where
the gradient and the curvature of the mean velocity profile and the
magnitude of the wave-induced vertical velocity are large.

In recent years, Miles' theory was compared with experimental data
on wave-induced pressure and wave growth rate obtained both in labora-
tories and in the field. Shemdin and Hsu (1967) measured the wave-induced
pressure distribution over mechanically generated waves in the labora-
tory and inferred that the wave growth rate was larger by a factor of
about two than that predicted by Miles' theory. Bole and Hsu (1969)
measured the wave height of mechanically generated waves along the wind-
water channel and found that the growth rate was underpredicted by
Miles' theory by about one-order of magnitude. Similar results were
obtained in the field by Snyder and Cox (1966), Barnett and Wilkerson
(1967), and Dobson (1969). Based on the existing experimental results

-3-

we can conclude that Miles' theory is inadequate for the prediction of wind-wave growth. Consequently, investigators have been devoting their efforts to investigate the neglected effects of turbulence as well as nonlinear mechanisms on wave growth.

Three nonlinear mechanisms were proposed. First, Miles (1967) improved his own model by considering the turbulence which was neglected in his laminar model. The expected result is that the turbulent structure over the wavy boundary will be affected by the interaction with wave-induced perturbation field, and the oscillating wave associated turbulent stresses may be essential to the processes of energy transfer to the water waves. Good turbulence and wave-induced perturbation data are needed for modeling the relationship between these two fields. Furthermore, in order to solve the modified Orr-Sommerfeld equation containing the unknown terms associated with the oscillating wave-induced turbulent stresses, ad-hoc closure conditions would have to be assumed. Efforts were made by Hussain and Reynolds (1970), Davis (1970, 1972) and Chao, et al. (1976). As we know, this is one of the basic unsolved problems associated with the process of the generation of turbulent stresses. Therefore, more effort is needed before we truly understand the role of the oscillating-wave-associated turbulent stresses.

Second, Longuet-Higgins (1969a) proposed a nonlinear "Maser mechanism" based on the commonly observed phenomenon: long waves sweeping over short waves and causing short waves to break on the forward face of the long wave crests and to give up their energy to the long waves. The energy transfer rate is proportional to the orbital velocity of the long waves since the orbital motion is forward at the forward face of the

-4-

long wave crest, the short wave therefore supplied a positive amount of energy to the long waves. However, Hasselmann (1971) proved that this positive energy transfer is almost exactly balanced by the loss of potential energy arising from the mass transfer. Analyzing the field data, Barnett (1971) failed to identify the energy transfer caused by this mechanism, he concluded that "maser mechanism" is not of first order importance to the energy balance of the wave spectrum.

Third, Hasselmann (1962, 1963) proposed the nonlinear wave-wave interaction theory which shows that the energy can be transferred among different wave components in a gravity-wave spectrum. He employed perturbation technique to find the nonstationary growth in the initial energy spectrum. Appreciable modification of the initial sea state was found from the solution of the fifth-order perturbation equation. The rate of change of the energy spectrum can be expressed by an integral expression in terms of wave spectral density and a transfer function.

Figure 1.1 (Barnett 1971) shows the comparison of energy transfer calculated from Hasselmann's nonlinear wave-wave interaction theory by using an empirical fully developed Pierson-Moskowitz spectrum and observed field spectrum. For the broader Pierson-Moskowitz spectrum, the major transfer acts to sharpen the spectral peak, while the nonlinear transfer in the observed spectrum acts to maintain the low frequency steep forward face of the spectrum and serves as an influential growth mechanism. The figures show an important fact, namely, the energy transfer is always from the high frequency portion to the low frequency portion of the spectrum. Based on JONSWAP (Joint North Sea Wave

Project) data, Barnett (1971) found that from 30% to 90% of the observed wave growth is accounted for by the nonlinear wave-wave interaction theory. Therefore, Barnett suggests that the nonlinear wave-wave inter-action mechanism will dominate all the energy transfer soon after the wave spectrum generated by Phillips' resonance mechanism. Because it takes excessive computer time to integrate the triple integral equation for the nonlinear energy transfer, Barnett (1966) proposed a parame-terized equation to approximate Hasselmann's theoretical results for practical applications. This parametric equation is applicable for both fully and partially developed wave spectra. Mitsuyasu (1968b) employed Barnett's parametric equation in his investigation of nonlinear energy transfer in a wave decaying region and indicated the importance of this mechanism.

Barnett (1968) developed a wave prediction model based on the radia-tive transfer equation. This model takes into account energy transfer by both resonance and instability mechanisms, the nonlinear wave-wave interaction mechanism, and the wave-breaking dissipative mechanism. Although it was only a first attempt to establish a framework for ra-tional wave prediction, reasonable results were obtained.

It will be shown later that successful prediction of a wave spec-trum evolution depends not only on the source function S'_{nl} (associa-ted with the nonlinear wave-wave interaction), but also on the source function S'_{in} (turbulent air-input to waves) and S'_{ds} (wave dissipa-tion due to white-capping). Hasselmann(1974) proposed a white-capping dissipative model which could be useful for a wave energy balance scheme. If the appropriate air-input model could be constructed, then

we should be able to formulate a more complete wave prediction model based on the radiative transfer equation with source terms of air-input, nonlinear wave-wave interaction, and white-capping dissipation.

One of the most important questions, which must be answered, in the wave generation process is "What fraction of the momentum available in the air can be transferred directly into the wave field?" Stewart (1961) reanalyzed some older wave data measured at known fetches and wind speeds and came to the conclusion that the lower limit is about 0.2 and the upper limit is unity. Based on Miles' theory, Phillips (1966) estimated this fraction for waves with $c/u_* > 5$, where c is the wave speed and u_* is the friction velocity, and found the fraction to be less than or equal to 0.1. Such a small fraction of momentum flux to the wave field must be associated with an underestimation of the energy transfer in Miles theory. Wu Jin (1968) measured the wind generated waves in the laboratory and his results were in the range from 0.1 to 0.4 for $c_p/u_* < 7.5$, where c_p is the wave speed of the peak frequency of the wave spectrum. Based on this field measurements, Dobson's results are in the range from 0.6 to 1.6 for $9.6 < c_p/u_* < 49$. The average fraction is 1.1, which is greater than 1 and seems unreasonable. One of his most reliable sets of data yield a value of 0.8. The momentum in the air was estimated from the empirical formula, $\rho_a c_d u_5^2$ (where ρ_a is air density, the drag coefficient c_d equals 0.0012, and u_5 is the mean velocity above five meters of the water surface). The uncertainty in drag coefficient may be a main source contributing to the large apparent error. Because of differences in the range of c_p/u_* values, comparisons between Dobson's

-7-

and Wu's experimental data can not be made. Barnett (1971) analyzed the field data by computing the atmosphere external source function in the energy balance equation and found that the average values of the momentum fraction varied from 0.1 to 0.2. There are close to the Phillips' prediction and Wu's data, but deviate considerably from Dobson's results. The recent JONSWAP results presented by Hasselmann, et al. (1973) showed that the fractions are at least 0.8 for $\tilde{x} \approx 10^2$, and 0.2 for $10^3 \leq \tilde{x} < 10^4$, where $\tilde{x}$ is nondimensional fetch ($\tilde{x} = xg/u_{10}^2$, x is fetch, g is the gravitational acceleration and u_{10} is the mean velocity at ten meters above the water surface). Therefore, these fraction could be fetch and wind speed dependent. Careful and direct measurement of this fraction must be done in order to supply correct information to establish a complete wave generation theory.

1.2 Objectives

Based upon the previous discussion, we conclude that Miles' model alone can not predict wave growth successfully. The relative importance of the nonlinear wave-wave interaction mechanism should be investigated, especially as the basis for a practical wave prediction scheme. There have been no systematic experiments designed to investigate this mechanism in the laboratory. Although there are some preliminary field data on nonlinear transfer, the limited accuracy of the field data makes the interpretation of the experimental results difficult, leading to some reservation about the results. It seems to be expedient to verify presence of the non-linear wave-wave interaction process, to obtain a

-8-

quantitative determination of the momentum and energy transfer from wind to waves, and to examine Hasselmann's proposed dissipation mechanism due to white-capping of a gravity wind wave spectrum in a laboratory under controlled conditions. Therefore, a complete experimental program was proposed and carried out. The main objectives are as follows:

(1) To obtain the simultaneous experimental data of wave height, fluctuating pressure and velocity components in close proximity to a wave-perturbed air-water interface in order to evaluate the momentum and energy transfer from wind to waves.

(2) To study and verify Hasselmann's nonlinear wave-wave interaction mechanism experimentally, and to verify Barnett's approximate parameterized equation for practical applications in calculating energy transfer due to nonlinear wave-wave interactions.

(3) To study and verify Hasselmann's white-capping dissipative mechanism experimentally.

2.   THEORETICAL BACKGROUND

The energy balance equation of a gravity wind wave field during its generation processes is described. The relevant source functions associated with the wave generation are also presented.

2.1 Energy Balance Equation of Wind Wave Spectrum

The energy balance equation (radiative transfer equation) for deep water gravity wave was proposed independently by Gelci, et al. (1956), Hasselmann (1960) and Groves and Melcer (1961). This equation describes the propagation and the processes of generation and dissipation of a wind wave spectrum and can be represented by [The more complete form formulated by Hasselmann (1968) is presented in Appendix B.]

$$\frac{dF}{dt} = \frac{\partial F}{\partial t}(f,\theta,\vec{x},t) + \vec{V}(f,\theta) \; \vec{\nabla}F(f,\theta,\vec{x},t) = S'(f,\theta,\vec{x},t)$$

$$= S'_{in}(f,\theta,\vec{x},t) + S'_{nl}(f,\theta,\vec{x},t) + S'_{ds}(f,\theta,\vec{x},t)$$

$$+ S'_{re}(f,\theta,\vec{x},t) \qquad (2.1)$$

where F is the two-dimensional (frequency f and angle θ) energy spectrum defined by the ensemble average (denoted by the bracket < >) of the wave height η , i.e.,

$$\int_{-\pi}^{\pi} \int_{0}^{\infty} F(f,\theta) \; dfd\theta = \int_{0}^{\infty} E(f) \; df = <\eta^2> \qquad (2.2)$$

and $\vec{V}(f,\theta)$ is the group velocity of the wave with frequency f and propagating at an angle θ measured clockwise from the wind (x-) direction.

-10-

In equation (2.1), S' is the net rate of energy transfer due to all the interaction processes existing in the fields of wind, wave, current, etc. S'_{in} is the rate of energy transfer from wind to waves, which includes the linear mechanisms proposed by Phillips (1957) and Miles (1957), and nonlinear interactions between the wave-induced field and background turbulent field. S'_{nl} is the rate of energy transfer resulting from Hasselmann's (1962, 1963) nonlinear wave-wave interactions. S'_{ds} is the rate of energy dissipation caused by white-capping; the theoretical model of this transfer was proposed by Hasselmann (1974). S'_{re} is the rate of energy transfer between wind-mean current and wave-mean current fields, etc.

Because of the extremely limited variation of energy spectra with respect to θ in laboratory channels, one-dimensional (frequency f) energy spectra were measured and used in the equation. Consequently, equation (2.1) should be simplified to one-dimensional form for this study. It is commonly assumed that under the assumption of the independence of frequency, f and direction, θ, $F(f,\theta)$ can be approximated by the product of the one-dimensional energy spectrum $E(f)$ and the normalized directional spreading factor $D'(\theta)$, expressed as

$$F(f,\theta) = E(f) \, D'(\theta) \tag{2.3}$$

where $E(f)$ is defined by equation (2.2) and $D'(\theta)$ is chosen (Hasselmann, 1963b; Mitsuyasu, 1968b) for the narrow directional distribution of a wind-wave channel as

-11-

$$D'(\theta) = (8/3\pi) \, \text{Cos}^4\theta \qquad \text{for} \quad |\theta| \leq \pi$$

$$= 0 \qquad \text{for} \quad |\theta| > \pi \qquad (2.4)$$

and $\qquad \displaystyle\int_{-\pi}^{\pi} D'(\theta)d\theta = 1$

Substituting equations (2.3) and (2.4) into (2.1) and integrating with respect to θ from $-\pi/2$ to $\pi/2$, by assuming the absence of backward scatter in the wind-wave channel, we can reduce equation (2.1) to a one-dimensional equation (frequency dependent only). After the integration, equation (2.1) can be further simplified, in the x-direction along the channel and for a stationary deep water gravity wave spectrum, to

$$\rho_w \, g \, \overline{V}_x(f) \, \frac{\partial E(f)}{\partial x} = S(f) = S_{in}(f) + S_{nl}(f) + S_{ds}(f) \qquad (2.5)$$

where $\overline{V}_x(f) = \displaystyle\int_{-\pi/2}^{\pi/2} V(f) \, \text{Cos}\theta \, F(f,\theta) \, d\theta \, / \, E(f) = 32g \, / \, (45\pi^2 f)$ is the mean group velocity in x-direction, $V(f) = g \, /4\pi f$ is the group velocity of the wave with frequency f and is equal to half of the phase speed in deep water and ρ_w is the water density. Because of the small drift-current in the channel and weak interaction between wave and current, S'_{re} in equation (2.1) is neglected. $S_{in}(f)$, $S_{nl}(f)$ and $S_{ds}(f)$ in equation (2.5) represent the first order processes of the energy transfer associated with a wave spectrum. The detailed description of these transfer processes is given in the following sections.

-12-

2.2 Energy Transfer from Wind to Waves

The energy transfer from wind to waves in a turbulent developing boundary layer is derived in Appendix D. The work done by the normal pressure in quadrature with the wave height (Stewart 1961) is

$$S_{in}^{''}(t) = -p(t) \frac{\partial \eta(t)}{\partial t} \tag{2.6}$$

where $p(t)$ is the pressure at the interface, $\partial \eta(t) / \partial t$ is the vertical velocity of the water surface. [The negative sign is associated with a defined positive upward cartesian co-ordinate system.] Because of the limitation of the present laboratory instrumentation and the difficulties of following the whole wave spectrum, it is exceeding difficult to measure the pressure at the interface. The alternative is to use a fixed-frame of reference and to measure the pressure as close to water surface as possible.

The energy transfer spectrum can be obtained by taking the Fourier Transform of equation (2.6), viz.,

$$S_{in}(f) = 2\pi f \, Qu_{p\eta}(f) \tag{2.7}$$

where $Qu_{p\eta}(f)$ is the quadrature spectrum of pressure and wave height. Since the ratio of energy to momentum for a deep water gravity wave is equal to its phase speed c, Stewart (1961) suggested the spectrum of momentum transfer can be expressed as (see also Dobson, 1971)

$$\tau_w(f) = S_{in}(f) \, / \, c = 2\pi f \, S_{in}(f) \, / \, g \tag{2.8}$$

-13-

where $c = g / 2\pi f$ is the phase speed of the deep water gravity wave.
Based on equations (2.7) and (2.8), we can evaluate the energy and
momentum transfer from wind to waves due to normal pressure acting on
water surface.

2.3 Energy Transfer of Nonlinear Wave-Wave Interactions

2.3.1 Theoretical Expression of Energy Transfer of Nonlinear Wave-Wave Interactions

Hasselmann (1962) proposed the conservative nonlinear wave-
wave interactions mechanism for the gravity wind wave spectrum. As a
result of this interaction, energy can be transferred and redistributed
among different wave components. The theoretical derivation was based
on the assumptions of inviscid fluid, two-dimensional and irrotational
water motion. The velocity potential $\Phi(x,t)$ and free surface $\eta(x,t)$
were used as the perturbation parameters. Hence they were expanded
in a series and substituted in the governing Laplace equation, kinema-
tical and dynamical boundary conditions, as well as in initial condi-
tions to generate higher order perturbation equations. The aim of his
investigation was to determine the change (nonstationary growth) in the
initial energy spectrum brought about by the nonsteady higher-order
perturbations. On using a fifth order perturbation, the nonstationary
solution was found to grow continually with time, resulting in an
appreciable modification of the initial sea state. The rate of change
of the energy spectrum was determined by the following equations
(Hasselmann 1963).

$$\frac{\partial}{\partial t}[f(k_4,\theta_4)] = \int_o^\infty \int_o^\infty \int_{-\pi}^{\pi} \{\sum_{j=1}^{2} \omega_4 \ T[\ \frac{\omega_4 k_4}{k_3} f(k_1,\theta_1)\ f(k_2,\theta_2^{(j)});\ f(k_3,\theta_3^{(j)})$$

$$+ \omega_3\ f(k_1,\theta_1)\ f(k_2,\theta_2^{(j)})\ f(k_4,\theta_4)$$

$$- \omega_2(k_2/k_1)\ f(k_3,\theta_3^{(j)})\ f(k_4,\theta_4)\ f(k_1,\theta_1)$$

$$- \omega_1(k_1/k_2)\ f(k_3,\theta_3^{(j)})\ f(k_4,\theta_4)\ f(k_2,\theta_2^{(j)})]\}\ d\theta_1 dk_1 dk_2$$

$$(2.9)$$

where k and ω are the wave number and frequency, respectively.
The resonance conditions are

$$\vec{k}_1 + \vec{k}_2 = \vec{k}_3 + \vec{k}_4$$

and

$$\omega_1 + \omega_2 = \omega_3 + \omega_4$$

The dispersion relation for a deep water wave is

$$\omega_j = 2\pi f_j = (gk_j)^{1/2} \qquad (2.10)$$

The equations of resonance conditions and dispersion relation can be
reduced to the single equation (Hasselmann, 1963b)

$$2 \, \text{Cos}\beta \, |\vec{k}_2| \, |\vec{k}_1 - \vec{k}_4| = (\sqrt{k_1} + \sqrt{k_2} - \sqrt{k_4})^4 - k_2^2 - (\vec{k}_1 - \vec{k}_4)^2 \qquad (2.11)$$

with β being the angle between $\vec{k}_2$ and $(\vec{k}_1 - \vec{k}_4)$. Since the interaction surface is three dimensional in $(\vec{k}_1, \vec{k}_2)$-space, the transformation to the surface integral can be affected simply by introducing polar coordinates, i.e. $\vec{k}_j = (k_j, \theta_j)$. In examining equation (2.9) for fixed k_4 and θ_4, and the given values of the integral variables, k_1, k_2, and θ_1, it is seen that θ_2, k_3 and θ_3 are the remaining undetermined variables for completing the integration. β can be determined from equation (2.11) by giving the values of k_1, θ_1, k_4, θ_4 and k_2. Since β is the angle between $\vec{k}_2$ and $(\vec{k}_1 - \vec{k}_4)$, θ_2 can be determined by providing the values of k_2, k_1, k_4, θ_1, θ_4 and β. Finally, k_3 and θ_3 can be calculated by equation (2.10) for all determined values of k_1, θ_1, k_2, θ_2, k_4, and θ_4. $\theta_2^{(1)}$, $\theta_3^{(1)}$ and $\theta_2^{(2)}$, $\theta_3^{(2)}$ are correspondent to the values of $+\beta$ and $-\beta$ respectively. The spectral density in polar co-ordinates is

$$f(k,\theta) = \rho_w g f \, F(f,\theta) \, / \, 2k \qquad (2.12)$$

and the function T can be expressed as

$$T = \pi \left(\frac{3gD}{2\rho_w \, \omega_1 \omega_2 \omega_3 \omega_4} \right)^2 \frac{2\omega_3^3}{k_2 \, |\vec{k}_1 - \vec{k}_4| \, |\text{Sin}\beta| \, g^2} \qquad \text{for} \quad |\text{Cos}\beta| < 1$$

$$= 0 \qquad \text{for} \quad |\text{Cos}\beta| \geq 1$$

$$(2.13)$$

where $D = D^{+, +, -}_{\vec{k}_1, \vec{k}_2, -\vec{k}_3}$ is the transfer coefficient. The full expressions for D were given by equations (4.9) and (4.10) in Hasselmann (1962). Based on the described relationship of all θ and k and the defined functions of $f(k,\theta)$ and T, we can calculate the rate of nonlinear energy transfer due to water wave-wave interaction by equation (2.9).

The results of nonlinear energy transfer (equation(2.9)) were interpreted by Hasselmann (1962) in terms of quadruple interactions between three "active" wave components which determine the interaction rate, and a "passive" fourth component which receives energy from the first three components but has no direct influence on the interaction. The numerical calculations of a fully developed Neumann spectrum were performed by Hasselmann (1963b). The results showed that the transfer process tends to reduce sharp peaks in the spectrum and redistribute the energy more uniformly over all wave components by transferring the energy from the middle frequency range into the lower and higher frequency ranges.

2.3.2 Parametric Approximation of Energy Transfer of Nonlinear Wave-Wave Interactions

The evaluation of the nonlinear wave-wave interactions involves complicated numerical computations with equation (2.9), requiring six hours computer time (Hasselmann 1963b) on a CDC 1604. Even the newly developed program by JONSWAP still takes 20 minutes of computer time on a CDC 6600. Thus, it seems to be uneconomical and impractical for field application. In addition, the new program

-17-

provided by Dr. Sell can not be directly used for this study because of the differences in frequency scales. Efforts were made to change to frequency scales consistent with this study, but unfortunately, this did not succeed. Consequently, Barnett's (1966) parametric equations to approximate Hasselmann's theoretical results were used in this study.

The parameters to characterize the wave field are defined as

Energy:
$$e = \int_{-\pi}^{\pi} \int_{0}^{\infty} F(f,\theta) df d\theta$$

Mean frequency:
$$f_{o} = [\frac{1}{e} \int_{-\pi}^{\pi} \int_{0}^{\infty} F(f,\theta) \ f^2 \ df d\theta]^{1/2}$$

Mean direction:
$$\theta_{o} = \frac{1}{e} \int_{-\pi}^{\pi} \int_{0}^{\infty} F(f,\theta) \ \theta \ df d\theta$$

The parametric equation of energy transfer associated with non-linear wave-wave interactions is

$$S'_{nl}(f,\theta) \simeq [\Gamma'(f,\theta) - \tau'(f,\theta) \ F(f,\theta)] \ \rho_{w}g \qquad (2.14)$$

where Γ' and τ' are integral functions of F. This approximation was considered to be the sum of two processes as originally demonstrated by Hasselmann (1962). Γ' was related to the passive components which receive energy from other components, while τ' F was related to the active components which transfer energy to other components. Using dimensional analysis and the qualitative features of Hasselmann's theory, Barnett proposed the following forms of Γ' and τ' for the case of fully developed sea:

-18-

$$\Gamma'(f,\theta) = \frac{4.4 \cdot 10^8 e^3 f_o^8}{g^4} \ \text{Cos}^4(\theta - \theta_o) \ (\frac{f - 0.42f_o}{f})^3 \ \cdot$$

$$\cdot \ \exp[-4(1 - \frac{f_o}{f})^2 + 0.1(\frac{f_o}{f})^5]$$

$$\text{for} \quad f > 0.42f_o \quad \text{and} \quad |\theta - \theta_o| < \pi/2$$

$$= 0 \quad \text{otherwise} \tag{2.15}$$

$$\tau'(f,\theta) = \frac{7.5 \cdot 10^7 e^2}{g^4 f} \ (1 + 16 \ |\text{Cos}(\theta - \theta_o)|) \ f_o^7 \ (f - 0.53f_o)^3$$

$$\text{for} \quad f > 0.53f_o$$

$$= 0 \quad \text{otherwise} \tag{2.16}$$

The one-dimensional form of the nonlinear energy transfer equation can be derived by substituting equations (2.4), (2.15) and (2.16) into equation (2.14) and integrating it with respect to θ from $-\pi/2$ to $\pi/2$. The resulting form can be expressed as

$$S_{nl}(f) \simeq [\Gamma(f) - \tau(f) \ E(f)] \ \rho_w g \tag{2.17}$$

where

$$\Gamma(f) = \frac{4.4 \cdot 10^8 e^3 f_o^8}{g^4} \ \frac{3\pi}{8} \ (\frac{f - 0.42f_o}{f})^3 \ \cdot$$

$$\cdot \ \exp[-4(1 - \frac{f_o}{f})^2 + 0.1(\frac{f_o}{f})^5]$$

$$\text{for} \quad f > 0.42f_o \quad \text{and} \quad |\theta - \theta_o| < \pi/2$$

$$= 0 \quad \text{otherwise} \tag{2.18}$$

and

$$\tau(f) = \frac{7.5 \cdot 10^7 e^2}{g^4 f} \ (1 + \frac{16^{2 \cdot 8}}{45\pi}) \ f_o^{\ 7} \ (f - 0.53f_o)^3$$

$$\text{for} \quad f > 0.53f_o$$

$$= 0 \quad \text{otherwise} \tag{2.19}$$

The results of nonlinear energy transfer calculated with the parameterized equation (2.17) compared well with those of Hasselmann's theoretical equation for the fully developed and partially developed seas. The comparison for a typical fully developed sea is shown in Figure 2.1.

2.4 Energy Dissipation of White Capping

Because dissipative processes such as molecular viscosity and turbulence (Phillips 1959, Hasselmann 1968) are inadequate to account for the observed energy removal from wind waves, the white capping is generally believed to be the dominant dissipative mechanism in a wave field at moderate and higher wind speeds. The effect of white capping on the spectral energy distribution was investigated by Hasselmann (1974). The problem was treated by expressing the white-cap interactions in terms of an equivalent ensemble of random pressure pulses. It is first shown that the source functions S_{ds}'' for any non-expansible interaction process which is strongly nonlinear locally but still weak-in-the-mean is quasi-linear with respect to the wave spectrum, i.e.,

$$S_{ds}''(\vec{k}) = -\gamma' E'(\vec{k}) \tag{2.20}$$

-20-

where γ' is the damping factor which depends on the entire wave spectrum; γ' is found to be $\gamma' = d (2\pi f)^2$, under the assumptions that the space-time scales of a white cap are small compared with the wave-heights and periods of the waves. Here, d is a constant for a given wave state and can be determined indirectly from the energy and momentum balance in the high-frequency equilibrium range. Finally, the dissipation spectra of ocean waves due to white capping can be expressed in the frequency domain by assuming that d is independent of the direction θ; the spectra is then

$$S_{ds}(f) = -d (2\pi f)^2 E(f) \rho_w g \qquad (2.21)$$

We can measure the net rate of energy transfer S (equation (2.5)) and the rate of energy transfer from wind to waves S_{in} (equation (2.7)). Based on equation (2.5), we can subtract S_{in} from S to obtain experimentally the sum $S_{nl} + S_{ds}$. It is clear that in order to separate the sum of the experimentally determined $S_{nl} + S_{ds}$, either S_{ds} or S_{nl} would have to be assumed. Based on the measured wind wave spectrum in the channel, equations (2.17) and (2.21) were used alternately in calculating the S_{nl} and S_{ds}, respectively.

2.5 Mean Momentum Transfer from Wind to Waves

The momentum transfer across the wind-wave surface in a turbulent developing boundary layer is derived in Appendix C. By neglecting the relatively small viscous terms, the final results of momentum transferred into current and waves, in the direction of wave propagation, can

-21-

be expressed as

$$M_c = - \rho_a \overline{u'v'} \qquad (2.22)$$

$$M_w = \overline{\tilde{p} \frac{\partial \eta}{\partial x}} + \rho_a \overline{\widetilde{u'^2} \frac{\partial \eta}{\partial x}} \qquad (2.23)$$

where M_c and M_w are momenta transferred to the current and waves
respectively. From these, we find the momentum transferred into waves
is not due only to the normal air pressure acting on water surface but
also due to the oscillating turbulent Reynolds stresses (wave associated
turbulent stresses) in the air. Finally, the ratio of the momentum
transferred into the waves (or supported by the wave form) over the
total momentum transferred across the interface in the direction of
the wave propagation can be estimated by the following equation

$$\gamma = M_w / (M_c + M_w) \qquad (2.24)$$

3. EXPERIMENTAL APPARATUS

Based on the objectives and theoretical background, the required data are water wave height, fluctuating pressure and velocities in the wind stream and the mean velocity profiles along the wind-wave channel as a function of fetch for a range of wind speeds. The facilities and instrumentation relevant to this experimental study are presented in the following sections.

3.1 Channel Description

All the experiments were conducted in the Stanford Wind-Wave Channel (Hsu, 1965) in the Hydraulics Laboratory at Stanford University. A schematic is shown in Figure 3.1. The channel is 37.7 m long with a rectangular cross section which is 2 m high and 0.98 m wide. The glass-walled test section is approximately 23 m long. Baskets of stainless steel machine turnings are located at the end of the channel and serve as a beach to absorb wave energy. An airfoil-bladed fan located at the channel exit draws air through the test section. A honeycomb is placed at the end of the channel to suppress secondary flows caused by the centrifugal action of the fan. The air inlet contains a curved section with a series of turning vanes, a 5.1 cm thick honeycomb with a 0.64 cm hexagonal mesh, and a group of small size screens to produce a relatively uniform flow. A 1.5 m long flat plate was mounted at the base of the last screen to provide a smooth transition for incoming air to the test section. The depth of water was approximately one meter and was adjusted until it coincided with elevation of the plate; thus, excessive

-23-

inlet disturbances were eliminated and the fetch could be determined precisely.

3.2 Instrumentation

3.2.1 Mean Velocity

The mean velocity profiles were measured with a 0.238 cm o.d. United Sensor pitot-static tube connected to a Pace differential transducer (model P90D) with a maximum pressure differential of 0.037 psid. The transducer served as one leg of a Sanborn 650 Recorder inductive bridge which converts pressure differential to electrical signals. A Combustion Institute micromanometer with resolution of $\pm$ 0.00127 cm of silicone oil (r.d. 0.82) was used to calibrate the transducer. A typical calibration curve is shown in Figure 3.2. The variation of the slope of calibration curve was less than 3% over the past three years. The transducer is extremely stable and reliable. The mean velocity was calculated using the expression

$$U = \sqrt{2\Delta p \ / \ \rho_a} \tag{3.1}$$

where Δp is differential pressure and ρ_a is the local air density.

3.2.2 Wave Height

The elevation of the instantaneous water surface was measured by a capacitance wave-height gauge. The wire gauge is an Isonel-insulated 0.1 mm diameter copper conductor. Variation of water levels produces a corresponding change in the capacitance of the

-24-

insulted wire. A complete description of the wave gauge can be found in Colonell (1966).

Calibration of the wave gauge was carried out by varying the depth of the submergence of the wire in the still water. The wave gauge was mounted on an accurate vertical positioning device located on an instrumentation carriage in the wave channel. The distance x(fetch) variation can be achieved by moving the carriage along the channel. The accuracy of measuring the vertical submergence of the wave gauge is 0.254 mm. Figure 3.3 shows a typical calibration curve of wave height.

3.2.3 Velocity Fluctuations

Thermo-Systems, Model 1010 constant temperature anemometer and a platinum cross-hot-film probe (X-array) having a diameter of 0.0508 mm were used to obtain the fluctuating velocity components measurements. The frequency response of the cross-hot-film (X-array) is 40,000 Hz. The longitudinal and vertical turbulent velocity components were determined by the sum or difference of the X-array signals.

The hot films were calibrated against the pitot-static tube (Section 3.2.1) in the free stream of the wind-wave channel. The voltage output E from the anemometers and the effective velocity U_{eff} normal to the hot film can be represented by

$$E^2 = A + B \, U_{eff}^n \tag{3.2}$$

where A, B and n are constants to be determined from the calibration. The effective velocity can be determined by resolving the

-25-

measured free stream velocity normal to each hot-film. The least
square method was employed to determine these constants for each film
by providing the data of E and U_{eff} for ten wind speeds. Although
the calibrations were found to be quite repeatable, a check of the wire
calibration was carried out before and after each run. A typical cali-
bration curve of E^2 versus U^n_{eff} is shown in Figure 3.4.

3.2.4 Pressure Fluctuation

The pressure signal was measured by a crystal pressure
transducer manufactured by the Cornell Aeronautical Laboratory. The
assembly consists of a thin disc-shaped pressure probe, connecting tube,
and phenolic disc-shaped housing which contains the crystal transducer
sensor and high impedance converter. The output from the high impedance
converter was connected to a 1000 gain box to complete the pressure
measuring system. The probe is a 0.159 cm thick, 0.635 cm in diameter
streamlined thin disc with a 0.033 cm diameter piezometric hole at the
center of disc on each side. A small stainless-steel tube of the same
diameter as the piezometric hole was used to connect the probe and the
transducer sensing element. The small size of the connecting tubing is
necessary to minimize the inertia effect of the air mass in the system.
A larger (0.159 cm diameter) outer tube was used to protect the inner
tube and also provide better supporting strength. The detailed struc-
ture of this transducer is shown in Figure 3.5.

The crystal pressure transducer has a linear input-output response
and a sensitivity of 2.0 volts per psi with a noise level of 50 micro-
volts peak-to-peak. The output of this transducer is very sensitive to

-26-

the effect of dirt and humidity so special care was taken to maintain its normal operation.

The pressure transducer was calibrated dynamically against the Pace transducer, while the Pace transducer was calibrated statically by a combust micromanometer (Section 3.2.1). The dynamic calibration was performed in a pressure chamber 1.32 m long with a 12.7 cm inner diameter. A sinusoidal pressure signal was generated by the reciprocal motion of a small piston-cylinder assembly mounted on the end of the pressure chamber and connected to a rotating wheel driven by a D. C. servo motor through a D. C. function generator. During calibration both the pressure sensing probes connected to the crystal sensor and to the reference Pace transducer were placed at the end of the pressure chamber opposite to the piston-cylinder assembly. Three different amplitudes of the sinusoidal input signal can be obtained by changing the stroke of the piston. A typical calibration curve of the crystal transducer output versus the Pace transducer output is shown in Figure 3.6. The frequency response of the crystal pressure transducer is constant over the range of 1 to 20 Hz which was satisfactory for this present study. Figure 3.7 shows the frequency responses at the three different amplitudes. The magnitude of the transfer function ($|H(f)|$) associated with the pressure sensing system was defined in Section (4.2.3). The phase shift of the pressure sensing system (including the 1000 gain box) was calibrated against a pulse signal triggered by the light passing through a hole in the rotating wheel and to a photo-electric cell located at the other side of the wheel. Both the pressure and pulse signals were recorded simultaneously on a Sanborn

-27-

recording oscillograph to deduce the phase shift of the pressure sensing system. Figure 3.8 shows the phase shift induced by the crystal transducer, 1000 gain box and high impedance converter as a lag of the sensing system behind the actual pressure wave.

3.2.5 Sensor Arrangement

The wave-height gauge, the hot film and the crystal pressure sensor were installed in the channel at the same fetch. The wave-height gauge was installed at the center line of the channel. The hot film and the pressure sensor were located 1.5 cm to each side of the wave-height gauge and mounted on a vertical positioning device which can be adjusted by a control panel outside the channel.

3.3 Traversing Mechanism

In order to measure the mean velocity profiles for each stations, the pitot-static tube was mounted on the instrument carriage. The carriage and its traversing mechanism could be moved in either horizontal or vertical directions. The vertical positioning of the traverse was remote controlled with a resolution of 0.25 mm. The details of the carriage and traversing mechanism are given by Chambers, et al (1970).

3.4 Data Acquisition-Reduction System

A Hewlett-Packard 2100A computer system was used for data acquisition and analysis. This real-time data acquisition-reduction system includes a computer, analog-to-digital converter, magnetic tape drive,

-28

output terminal, disc operating system, etc. The dynamic range of the analog-to-digital converter is $\pm$ 10 volts. Sixteen active input channels to the converter are available. The maximum sampling rate is 45,000 samples per second. The accuracy of the system is $\pm$ 0.01 volts with a resolution of $\pm$ 5 mv. The statistical evaluation of this system performance was made by Takeuchi and Mogel (1974), and the excellent agreement with theoretical predictions was obtained.

All the data taken by this system were digitized and stored on magnetic tape for later analysis.

4. DATA ACQUISITION AND REDUCTION METHODS

4.1 Data Acquisition Procedure

In this study, experimental data were taken at five stations along the channel with fetches of 3.46 m, 6.51 m, 9.48 m, 12.61 m and 15.66 m and three wind speeds of 7.09, 8.01 and 8.88 m/sec. The channel was filled with water at least two days before each experiment to allow ample time for deaeration. Otherwise the dissolved air in the water adheres to the wire of the wave height gauge and affects its normal operation.

The normal operating procedure was to set the desired wind speed and run the channel for approximate thirty minutes before data acquisition to insure development of a stationary wave height spectrum. The highest point of the wave was then determined and the hot film and crystal pressure transducer probe was set 0.508 cm above this highest point. The fluctuating pressures, velocities, and wave height data were simultaneously taken and recorded by the HP 2100A data acquisition-reduction system. All the signals were appropriately amplified and low pass filtered with the 3 db point at 20 Hz; they were then sampled every 0.025 seconds for 10 minutes and stored on magnetic tape. The measurements were made at five different elevations (0.058 cm apart each) above the highest point of the wave. The computation of the experimental results was based on the data taken at the lowest elevation, i.e., 0.508 cm above the highest wave. The remaining data was used as a check to reveal any abnormality during the data taking process. However, in order to reveal the full

frequency range of the turbulence characteristics in the air stream, one extra set of velocity fluctuation data was taken at the lowest elevation with a 5000 Hz sampling rate and 2500 Hz cutoff frequency for four minutes. There were six runs (five elevations and one extra velocity at lowest elevation) for each wind speed. After finishing experiments at the three selected wind speeds, the instrumentation was moved to another station until data taking at the five stations was completed.

The mean velocity profiles were measured independently by pitot-static tube after completing the data taking discussed previously. The mean velocity was obtained by averaging the readings which were taken every 0.01 second for two minutes. The experimental conditions were, of course, kept the same as those used previously.

4.2 Data Reduction Procedure

4.2.1 Auto and Cross Spectra, Coherence and Phase

The auto and cross spectra of wave height, wave-induced velocities and pressure were computed via FFT method with a cosine window and a 512 point block size for a 50 spectra average. The auto spectrum $S_x(f)$ of the random variable $x(t)$ can be estimated as

$$S_x(f) \simeq <X^*(f)X(f)> \qquad (4.1)$$

where $X(f)$ is the Fourier Transform of $x(t)$ and $X^*(f)$ is the complex conjugate of $X(f)$. The bracket represents the ensemble average or spectra average, which is the averaging process over the

-31-

total number of measurements of $X^*(f)X(f)$ at each frequency.

The cross-spectrum of the variables $x(t)$ and $y(t)$ is

$$S_{xy}(f) \simeq <X^*(f)Y(f)> = Co_{xy}(f) + i\, Qu_{xy}(f) \qquad (4.2)$$

where $Co_{xy}(f)$ is the cospectrum and $Qu_{xy}(f)$ is the quadrature spectrum.

The coherence and phase spectra can be defined as

$$R_{xy}(f) = \{[Co^2_{xy}(f) + Qu^2_{xy}(f)] / [S_x(f) \cdot S_y(f)]\}^{1/2} \qquad (4.3)$$

$$\Theta_{xy}(f) = \tan^{-1} [Qu_{xy}(f) / Co_{xy}(f)] \qquad (4.4)$$

4.2.2 Auto Spectrum of Wave-Induced Velocity Fluctuations

The measured velocity signal $x(t)$ can be considered (Chang, Plate and Hidy, 1971) as the sum of the mean quantity $\overline{x}$, the wave-induced perturbation $\tilde{x}(t)$, and the background turbulence $x'(t)$. The Fourier Transform of $x(t)$, after removal of the mean part $\overline{x}$, can be expressed as

$$X(f) = \tilde{X}(f) + X'(f) \qquad (4.5)$$

where $\tilde{X}(f)$ is the quantity correlated with the wave, and $X'(f)$ is the random component.

The auto spectra of wave-induced velocities can be derived under

-32-

the assumption of the statistical independence of background turbulence and wave height η (Chang, Plate and Hidy, 1971), i.e. $\langle X'^{*}(f)\Pi(f)\rangle = 0$, where the bracket denotes an ensemble average and $\Pi(f)$ is the Fourier Transform of $\eta(t)$. The derivation is as follows:

$$S_{x\eta} \cdot S_{\eta x} \simeq \langle X^{*}\Pi \rangle \cdot \langle \Pi^{*}X \rangle = (Co_{x\eta} + i\ Qu_{x\eta})\ (Co_{x\eta} - i\ Qu_{x\eta})$$

$$= Co_{x\eta}^{2} + Qu_{x\eta}^{2} \tag{4.6}$$

By appling the assumption $\langle X'^{*}\Pi \rangle = 0$, equation (4.6) can be written as follows after we take a sufficient number of spectrum averages (a 50 spectra average was used for this data reduction):

$$S_{x\eta} \cdot S_{\eta x} \simeq \langle X^{*}\Pi \rangle \cdot \langle \Pi^{*}X \rangle \simeq \langle \tilde{X}^{*}\Pi \rangle \cdot \langle \Pi^{*}\tilde{X} \rangle$$

$$\simeq \langle \tilde{X}^{*}\tilde{X} \rangle \cdot \langle \Pi^{*}\Pi \rangle \simeq S_{\tilde{X}} \cdot S_{\eta} \tag{4.7}$$

Equating equations (4.6) and (4.7), one finds the auto spectra of the wave-induced velocities as

$$S_{\tilde{X}}(f) \simeq \langle \tilde{X}^{*}(f)\tilde{X}(f) \rangle = (Co_{x\eta}^{2}(f) + Qu_{x\eta}^{2}(f))\ /\ S_{\eta}(f) \tag{4.8}$$

Another technique could be employed for this particular analysis and the same result obtained. If one assumes that the $\tilde{X}(f)$ response to $\Pi(f)$ is a linear process, i.e., $\tilde{X}(f) = \lambda(f)\ \Pi(f)$, the randomness in $\tilde{X}(f)$ is similar to that in $\Pi(f)$. The factor [or the transfer

-33-

function] $\lambda(f)$ may contain information of phase shift and amplitude attenuation of $\tilde{X}(f)$ with respect to $\Pi(f)$. If one multiplys $\Pi^*(f)$ with $\tilde{X}(f)$ in the assumed linear relationship, one obtains

$$\tilde{X}(f) \ \Pi^*(f) = \lambda(f) \ \Pi(f) \ \Pi^*(f)$$

Taking the ensemble average of the above equation produces

$$\langle \tilde{X}(f) \ \Pi^*(f) \rangle = \lambda(f) \ \langle \Pi(f)\Pi^*(f) \rangle$$

Solving for $\lambda(f)$, one obtains

$$\lambda(f) = \frac{\langle \tilde{X}(f)\Pi^*(f) \rangle}{\langle \Pi(f)\Pi^*(f) \rangle}$$

Consequently, the wave related signal $\tilde{X}(f)$ can be expressed as

$$\tilde{X}(f) = \frac{\langle \tilde{X}(f)\Pi^*(f) \rangle}{\langle \Pi(f)\Pi^*(f) \rangle} \ \Pi(f)$$

$$\simeq \frac{\langle X(f)\Pi^*(f) \rangle}{\langle \Pi(f)\Pi^*(f) \rangle} \ \Pi(f) \qquad (4.9)$$

since $\langle X'(f)\Pi^*(f) \rangle = 0$. Based upon equation (4.9), the averaged power spectrum of a wave-induced quantity can be expressed as

$$S_{\tilde{x}}(f) \simeq \langle \tilde{X}^*(f)\tilde{X}(f)\rangle = \left\langle \frac{\langle X^*\Pi\rangle\cdot\Pi^*}{\langle\Pi^*\Pi\rangle} \frac{\langle X\Pi^*\rangle\cdot\Pi}{\langle\Pi^*\Pi\rangle}\right\rangle$$

$$= \langle X^*\Pi\rangle\cdot\langle X\Pi^*\rangle / \langle\Pi^*\Pi\rangle$$

$$= (Co_{x\eta}^2(f) + Qu_{x\eta}^2(f)) / S_\eta(f)$$

This expression is the same as equation (4.8), which reveals that the linear assumption is reasonable and acceptable. This assumption will be employed latter for analyzing the energy and momentum transfer from wind to waves due to the oscillating wave-associated turbulent stresses.

4.2.3 Auto Spectrum of Wave-Induced Pressure Fluctuation

The desired pressure signals $p(t)$ are modified by a transfer function $h(t)$ of the system which includes the crystal transducer, high impedance converter and the 1000 gain amplifier. Therefore, the measured pressure signals $p_m(t)$ equal the convolution of $p(t)$ and $h(t)$, viz.,

$$p_m(t) = \int_{-\infty}^{\infty} p(t-t')\, h(t')\, dt'$$

The Fourier Transform of above equation is

$$P_m(f) = P(f)\, H(f)$$

where $P(f)$, $H(f)$ and $P_m(f)$ are the Fourier Transforms of $p(t)$,

-35-

$h(t)$ and $p_m(t)$, respectively. The magnitude of $H(f)$ can be defined as

$$|H(f)| \simeq |P_m(f)| \; / \; |P(f)|$$

Applying the assumption that $<P'^*\tilde{\eta}> = 0$, we can derive the auto spectrum of wave-induced pressure as follows:

$$S_{p_m\eta} \cdot S_{\eta p_m} \simeq <P_m^*\tilde{\eta}> \cdot <\tilde{\eta}^* P_m> = <P^* H^* \tilde{\eta}> \cdot <\tilde{\eta}^* PH>$$

$$\simeq <P^* \tilde{\eta}> \cdot <\tilde{\eta}^* P> \simeq <\tilde{P}^* \tilde{\eta}> \cdot <\tilde{\eta}^* \tilde{P}> \simeq <\tilde{P}^* \tilde{P}> \cdot <\tilde{\eta}^* \tilde{\eta}>$$

$$\simeq S_{\tilde{p}} \cdot S_\eta \qquad (4.10)$$

Therefore,

$$S_{\tilde{p}}(f) \simeq S_{p_m\eta} \cdot S_{\eta p_m} \; / \; S_\eta \simeq [\, Co_{p_m\eta}^2(f) + Qu_{p_m\eta}^2(f)] / \; S_\eta(f) \qquad (4.11)$$

where $H^*(f) H(f) = |H(f)|^2 = 1$, which was shown in Figure 3.7.

4.2.4 Cross Spectrum between Wave Height and Pressure Fluctuation

The cross spectra between wave height and pressure fluctuation can be used to calculate the energy and momentum transfer from wind to waves due to the normal pressure acting on the water surface. The cross spectrum between wave height and the measured pressure signal is

$$S_{p_m\eta}(f) \simeq <P_m^*(f)\tilde{\eta}(f)> = Co_{p_m\eta}(f) + i \; Qu_{p_m\eta}(f) \qquad (4.12)$$

-36-

while the cross spectrum between wave height and the desired pressure signal is

$$S_{p\eta}(f) \simeq <P^*(f)\Pi(f)> = S_{P_m\eta}(f) \, H(f) = Co_{p\eta}(f) + i \, Qu_{p\eta}(f) \qquad (4.13)$$

where $H(f) = |H(f)| \, e^{i\phi(f)} = Cos \, \phi(f) + Sin \, \phi(f)$. Here $\phi(f)$ is the phase angle of the transfer function $H(f)$ and was determined during calibration of the pressure measuring system as shown in Figure 3.8. Substituting $H(f)$ and equation (4.12) into equation (4.13) gives

$$S_{p\eta}(f) = (Co_{P_m\eta}(f) \cdot Cos \, \phi(f) - Qu_{P_m\eta}(f) \cdot Sin \, \phi(f))$$

$$+ i \, (Co_{P_m\eta}(f) \cdot Sin \, \phi(f) + Qu_{P_m\eta}(f) \cdot Cos \, \phi(f)) \qquad (4.14)$$

By comparing the real and imaginary parts of equations (4.13) and (4.14), the cospectrum and quadrature spectrum between the wave height and pressure fluctuation are seen to be

$$Co_{p\eta}(f) = Co_{P_m\eta}(f) \cdot Cos \, \phi(f) - Qu_{P_m\eta}(f) \cdot Sin \, \phi(f) \qquad (4.15)$$

$$Qu_{p\eta}(f) = Co_{P_m\eta}(f) \cdot Sin \, \phi(f) + Qu_{P_m\eta}(f) \cdot Cos \, \phi(f) \qquad (4.16)$$

Based on equations (4.15) and (4.16), the coherence spectrum and phase between wave height and pressure fluctuation are

$$R_{p\eta}(f) = [(Co_{p\eta}^2(f) + Qu_{p\eta}^2(f)) \, / \, (S_p(f) \cdot S_\eta(f))]^{1/2} \qquad (4.17)$$

$$\Theta_{p\eta}(f) = tan^{-1} \, (Qu_{p\eta}(f) \, / \, Co_{p\eta}(f)) \qquad (4.18)$$

-37-

where $S_p(f) \approx \left\langle \dfrac{P_m^*(f)}{H^*(f)} \cdot \dfrac{P_m(f)}{H(f)} \right\rangle = <P_m^*(f)P_m(f)> \approx S_{p_m}(f)$

In processing any functional relationship involving the measured pressure signal, it is necessary to account for the pressure system response as indicated by the results of calibration. However, system response is not a factor for the hot-film data, and equations (4.2), (4.3) and (4.4) can be used directly for calculating cross spectrum, coherence spectrum and phase difference between wave height and velocity fluctuations, respectively.

4.2.5 Energy Transfer from Wind to Waves

Since it is the pressure components out of phase with the progressive waves that transfer energy and momentum from the wind to the wave field, the quadrature spectrum between wave height and pressure in equation (4.16) is the key quantity in the process. By substituting equation (4.16) into equations (2.7) and (2.8), the energy and momentum transfer from wind to waves due to normal pressure acting on water surface can be expressed as

$$S_{in}(f) = 2\pi f \cdot (Co_{p_m\eta}(f) \cdot Sin\ \phi(f) + Qu_{p_m\eta}(f) \cdot Cos\ \phi(f)) \qquad (4.19)$$

$$\tau_w(f) = 4\pi^2 f^2 \cdot (Co_{p_m\eta}(f) \cdot Sin\ \phi(f) + Qu_{p_m\eta}(f) \cdot Cos\ \phi(f))\ /\ g \qquad (4.20)$$

It can be seen that the measured pressure fluctuation $p_m(t)$, wave height $\eta(t)$, and the calibration values of the pressure measuring system $H(f)$ and $\phi(f)$ are needed for such a calculation.

-38-

4.2.6 Energy Transfer of Nonlinear Wave-Wave Interactions

Since Barnett's parameterized equation (2.17) yields satisfactory agreement compared with Hasselmann's theoretical formulation, Barnett's approximate equations are used in this study. With the experimentally determined one-dimensional energy spectrum $E(f)$ at a certain fetch and the commonly adopted spreading factor $D'(\theta)$ for laboratory data, the wave parameters e, f_o and θ_o can be calculated. Consequently, τ and Γ can be evaluated from equations (2.18) and (2.19), and the non-linear wave-wave interaction $S_{nl}(f)$ can be calculated from equation (2.17). Because the direction of wave propagation is from shorter fetch to longer fetch, the information for waves at shorter fetch could be considered as the initial condition for the rate of change of energy between two consecutive stations. Therefore, the wave height spectrum $E(f)$ at shorter fetch was used in equations (2.17), (2.21), (4.22), and (4.23) to calculate $S_{nl}(f)$, $S_{ds}(f)$, $S_{nl}(f)$, and $S_{ds}(f)$, respectively.

It is to be noted from equation (2.5) that the net source function $S(f)$ can be calculated from the experimentally measured wave spectrum between two consecutive stations along the channel and can be expressed as

$$S(f) = \overline{V}_x(f) \; \rho_w g \; \frac{\Delta E(f)}{\Delta x} = \frac{32 \; g}{45 \pi^2 f} \; \rho_w g \; \frac{\Delta E(f)}{\Delta x}$$

In addition, the energy input to the wave from the air stream $S_{in}(f)$ was measured and can be calculated from equation (4.19). Consequently, the experimental results of the sum of source terms $S_{nl}(f)$ and

-39-

$S_{ds}(f)$ can be evaluated as

$$\hat{S}_{nl}(f) + \hat{S}_{ds}(f) = S(f) - S_{in}(f) \qquad (4.21)$$

Unless separate and independent experimental measurements of either $S_{nl}(f)$ or $S_{ds}(f)$ are made, it is not possible to separate these two functions. Futhermore, it seems extremely difficult to separate these functions experimentally. In order to calculate the non-linear wave-wave interaction based on an experimental data, $S_{ds}(f)$ must be assumed. If Hasselmann's white-capping dissipation model is adopted and $S_{ds}(f) = -d(2\pi f)^2 E(f)\rho_w g$ is calculated from equation (2.21), then the "experimental" $S_{nl}(f)$ can be represented by

$$\hat{S}_{nl}(f) = S(f) - S_{in}(f) - S_{ds}(f) \qquad (4.22)$$

The determination of the constant d in $S_{ds}(f)$ will be discussed in the next section.

4.2.7 Energy Dissipation of White Capping

As discussed in the previous section, in order to verify Hasselmann's white capping dissipation model, the source term $S_{nl}(f)$ would have to be assumed known. If Barnett's approximate representation of $S_{nl}(f)$ is adopted, the calculated or "experimental" white capping dissipation can be represented as

$$\hat{S}_{ds}(f) = S(f) - S_{in}(f) - S_{nl}(f) \qquad (4.23)$$

-40-

The white capping dissipation represented by equation (2.21) contains an unknown constant d which must be determined from the experimental data. In the high-frequency equilibrium range of a wave spectrum, the net source term $S^{hf}(f)$ must be zero. Therefore, we can express the energy and mean momentum transfer in the high frequency range as

$$S_{ds}^{hf}(f) = -S_{in}^{hf}(f) - S_{n1}^{hf}(f)$$

or

$$\overline{\tau}_{ds}^{hf}(f) = -\overline{\tau}_{in}^{hf}(f) - \overline{\tau}_{n1}^{hf}(f) \qquad (4.24)$$

where the superscript hf indicates the high frequency regime.

Since the energy spectrum in the equilibrium range can be approximated by the one-dimensional form $\alpha g^2 f^{-5}$, the mean momentum transfer (in the x-direction) due to white capping in the high-frequency equilibrium range can then be represented through the use of equation (2.21) as (Hasselmann, 1974)

$$\overline{\tau}_{ds}^{hf} = \int_{f_{so}}^{\infty} S_{ds}^{hf}(f) \,/\, \overline{c}_x(f) \; df$$

$$= \int_{f_{so}}^{\infty} -d \; (2\pi f)^2 \; (\alpha g^2 f^{-5}) \; \rho_w g \; (\overline{k}_x \,/\, 2\pi f) \; df$$

$$= (128 \,/\, 45\pi) \; d \; \rho_w g^2 \alpha \; 16\pi^4 \,/\, 2\pi f_{so} \qquad (4.25)$$

-41-

where $1 / \overline{c}_x(f) = \overline{k}_x / 2\pi f = \int_{-\pi/2}^{\pi/2} (k_x / 2\pi f) \, F(f,\theta) \, d\theta / E(f)$

$$= \int_{-\pi/2}^{\pi/2} (k / 2\pi f) \cdot \cos \theta \cdot (8/3\pi) \cdot \cos^4 \theta \cdot E(f) \, d\theta / E(f)$$

$$= (k / 2\pi f) (128 / 45\pi) = (2\pi f / g) (128 / 45\pi)$$

Here $\overline{k}_x$ is the average value of wave number k_x integrated over the normalized directional distribution of $E(f)$, ρ_w is the water density, g is the gravitational acceleration, α is Phillips constant of the equilibrium range of wave spectrum, and f_{so} is the lowest frequency at which the net energy transfer $S(f)$ equals to zero. Both α and f_{so} can be determined by the experimental results of wave height spectrum and net energy transfer spectrum $S(f)$. Substituting equation (4.24) into equation (4.25), the constant d can be expressed as

$$d = \frac{45\,\pi}{128} \; \frac{2\pi\,f_{so}}{\rho_w g^2 \alpha\;16\pi^4} \; (- \overline{\tau}_{in}^{hf} - \overline{\tau}_{nl}^{hf}) \tag{4.26}$$

where $\overline{\tau}_{in}^{hf} = \int_{f_{so}}^{\infty} 2\pi f \; Qu_{p\eta}(f) \; \dfrac{\overline{k}_x}{2\pi f} \; df$ can be evaluated from the experimental value of $Qu_{p\eta}(f)$ with a chosen f_{so}.

The evaluation of the term $\overline{\tau}_{nl}^{hf}$ needs further discussion. The theoretical results of non-linear wave-wave interaction $S_{nl}(f)$ cal-culated by Barnett's approximate parametric equation seem not to be adequate in the high frequency range [as we will see in Figures(5.20)

-42-

through (5.31)]. Some modification in calculating the $\overline{\tau}_{nl}^{hf}$ terms can be made, based upon Hasselmann's original assumption of conservative wave-wave interaction. This may be represented as

$$\int_o^\infty S_{nl}(f) \, \frac{\overline{k_x}}{2\pi f} \, df = \int_o^{f_{so}} S_{nl}(f) \, \frac{\overline{k_x}}{2\pi f} \, df + \int_{f_{so}}^\infty S_{nl}(f) \, \frac{\overline{k_x}}{2\pi f} \, df = 0 \tag{4.27}$$

Consequently, the required term $\overline{\tau}_{nl}^{hf}$ for evaluating d in equation (4.26) may be represented as

$$\overline{\tau}_{nl}^{hf} = \int_{f_{so}}^\infty S_{nl}(f) \, \frac{\overline{k_x}}{2\pi f} \, df = - \int_o^{f_{so}} S_{nl}(f) \, \frac{\overline{k_x}}{2\pi f} \, df \tag{4.28}$$

After d was determined, the "theoretical" results for $S_{ds}(f)$ were calculated by equation (2.21) and compared with "experimental" results computed by equation (4.23).

4.2.8 Mean Momentum Transfer from Wind to Waves

The ratio γ defined in equation (2.24) represents the magnitude of the fraction of mean momentum transferred to waves divided by the total mean momentum transferred across the wind-wave interface. It is shown in Appendix C that the mean momentum transferred into the wave field can be expressed as [c.f., equation (C.7)]

$$M_w = \overline{\tilde{p} \, \frac{\partial \eta}{\partial x}} + \overline{\rho_a \, \widetilde{u'^2} \, \frac{\partial \eta}{\partial x}}$$

-43-

and the total mean momentum transferred across the wind-wave interface is, [c.f. equation (C.6)]

$$M_w + M_c = \overline{\tilde{p} \frac{\partial \eta}{\partial x}} + \rho_a \overline{\widetilde{u'^2} \frac{\partial \eta}{\partial x}} - \rho_a \overline{u'v'}$$

In order to estimate the value of γ, three time-average terms in the above equation, i.e., $\overline{\tilde{p} \, \partial \eta / \partial x}$, $\overline{\widetilde{u'^2} \, \partial \eta / \partial x}$ and $\overline{u'v'}$, have to be evaluated. The data $\tilde{p}(t)$, $u'(t)$, $v'(t)$ and $\eta(t)$ required for calculating these three terms are in the time domain. Since it is extremely difficult to deduce the wave-induced (tilda-term) and background turbulent (prime-term) terms from the total signal for the wind wave spectrum, an alternative way was employed to calculate these three terms. Dobson (1971) showed that the time-average results of these terms equals the real part of the integration of their cross spectra over the appropriate frequency range. Therefore, the cross spectra between $\tilde{p}$ and $\partial \eta / \partial x$ (or $\tilde{p}$ and η), $\widetilde{u'^2}$ and $\partial \eta / \partial x$ (or $\widetilde{u'^2}$ and η), and u' and v' (or $\tilde{u}$ and $\tilde{v}$) should be calculated first and then integrated between certain lower and upper frequency limits. The lower limit of the integration is 0.078 Hz which is the bandwidth of the corresponding spectral estimates calculated from the relation $\Delta f = 1/(\tau N) = 1/(0.025 \times 512) = 0.078$ Hz, where τ (0.025 sec) is the sampling rate and N(512) is the number of data for each block of the Fourier Transform. The upper limit is 10.0 Hz which is the upper limit for a gravity wind-wave. The cross spectra associated with the derivative term $\partial \eta / \partial x$ can be simplified to that of η only by multiplying a factor of $(-ik)$ as a consequence of the form of the Fourier

-44-

Transform of $\partial\eta/\partial x$. Because of appearence of i $(= \sqrt{-1})$, the quadrature spectrum $iQu(f)$ was adopted in order to obtain the real-value results.

The detailed expressions for calculating the three key terms were then formulated as follows. The first term $\overline{\tilde{p}\ \partial\eta/\partial x}$ can be expressed as

$$\overline{\tilde{p}\ \frac{\partial\eta}{\partial x}} = \int (-ik)\ [i\ Qu_{p\eta}(f)]\ df$$

$$\simeq \sum_{f_i=0.078}^{10.0} k_i\ Qu_{p\eta}(f_i)\ \Delta f$$

where $k_i = (2\pi f_i)^2 / g$ is the wave number, $Qu_{p\eta}(f)$ is the quadrature spectrum between pressure and wave height, and $\Delta f = 0.078$ Hz is the bandwith of the spectrum estimates. The more explicit form of $\overline{\tilde{p}\ \partial\eta/\partial x}$ can also be written as

$$\overline{\tilde{p}\ \frac{\partial\eta}{\partial x}} \simeq \sum_{f_i=0.078}^{10.0} (4\pi^2\ f_i^2\ /\ g)\ Qu_{p\eta}(f_i)\ \Delta f \qquad (4.29)$$

The quadrature spectrum $Qu_{p\eta}(f_i)$ can be calculated based on equation (4.16).

The calculation of the second term, $\overline{\rho_a\ \widetilde{u'^2}\ \partial\eta/\partial x}$ involved extreme difficulty in calculating the Fourier component of $\widetilde{u'^2}$, i.e. $\widetilde{U'U'}(f)$, so the following relation was applied to simplify the calculation:

$$\widetilde{(u - \overline{u})^2} - \widetilde{\tilde{u}^2} = \widetilde{(\tilde{u} + u')^2} - \widetilde{\tilde{u}^2} = \widetilde{\tilde{u}^2} + \widetilde{2\tilde{u}u'} + \widetilde{u'^2} - \widetilde{\tilde{u}^2} = \widetilde{u'^2}$$

-45-

where the total signal u equal $(\bar{u} + \tilde{u} + u')$ and the quantities with the bar, tilda and prime represent mean, wave-induced, and background turbulent quantities respectively. Through the use of the above relations, the second term (in the time domain) can be rewritten as

$$\rho_a \overline{u'^2 \frac{\partial \eta}{\partial x}} = \rho_a \overline{[(u - \bar{u})^2 - \tilde{u}^2] \frac{\partial \eta}{\partial x}}$$

$$= \rho_a \overline{(u - \bar{u})^2 \frac{\partial \eta}{\partial x}} - \rho_a \overline{\tilde{u}^2 \frac{\partial \eta}{\partial x}}$$

Based on the previous discussion, these two terms can be expressed in the frequency domain in a form similar to equation (4.29), viz.,

$$\rho_a \overline{(u - \bar{u})^2 \frac{\partial \eta}{\partial x}} \simeq \rho_a \sum_{f_i=0.078}^{10.0} (4\pi^2 f_i^2 \, / \, g) \, Qu_{(u-\bar{u})^2 \eta}(f_i) \, \Delta f$$

and

$$\rho_a \overline{\tilde{u}^2 \frac{\partial \eta}{\partial x}} \simeq \rho_a \sum_{f_i=0.078}^{10.0} (4\pi^2 f_i^2 \, / \, g) \, Qu_{\tilde{u}^2 \eta}(f_i) \, \Delta f$$

or

$$\rho_a \overline{u'^2 \frac{\partial \eta}{\partial x}} \simeq \rho_a \sum_{f_i=0.078}^{10.0} (4\pi^2 f_i^2 \, / \, g) \, \Delta f [Qu_{(u-\bar{u})^2 \eta}(f_i) - Qu_{\tilde{u}^2 \eta}(f_i)]$$

$$(4.30)$$

where $Qu_{(u-\bar{u})^2 \eta}$ and $Qu_{\tilde{u}^2 \eta}$ are the quadrature spectra of $(u - \bar{u})^2$ and $\tilde{u}^2$ with respect to η, respectively. Since the time average quantity $\bar{u}$ can be easily obtained, $Qu_{(u-\bar{u})^2 \eta}$ can be calculated from equation

-46-

(4.2) by replacing x and y by $(u - \bar{u})^2$ and η respectively.

Because of the difficulties involved in decomposing the wave induced signal $\tilde{u}(t)$ (or $\tilde{U}(f)$), related to the wave spectrum, from the total signal $u(t)$, the quantity $Q_{u^2 \eta}$ can not be calculated directly from equation (4.2). Therefore, the assumption described by equation (4.9) in Section 4.2.2, i.e., $\tilde{U}(f) \simeq <U(f)\ \Pi^*(f)> \Pi(f)\ /\ <\Pi^*(f)\ \Pi(f)>$ is employed to calculate the Fourier Transform of $\tilde{u}^2(t)$, denoted as $\widetilde{UU}(f)$, then the cross spectrum between $\tilde{u}^2(t)$ and $\eta(t)$, i.e., $[\widetilde{UU}(f)]^* \Pi(f)$, and its quadrature spectrum $Q_{\tilde{u}^2 \eta}(f)$. The derivation are shown below.

If $a(t)$ and $b(t)$ are any two time signals and $A(f)$ and $B(f)$ are their respective Fourier Transforms, then the Fourier Transform of the convolution of $a(t)$ and $b(t)$ is (Bracewell, 1965)

$$F\{a(t) * b(t)\} = A(f)\ B(f)$$

The convolution of the Fourier Transform of $a(t)$ and $b(t)$ is

$$A(f) * B(f) = F\{a(t)\ b(t)\}$$

where $*$ denotes convolution and $F\{\ \}$ represents Fourier Transform. The definition of convolution is

$$a(t) * b(t) = \int_{-\infty}^{\infty} a(t-t_1)\ b(t_1)\ dt_1$$

or

$$A(f) * B(f) = \int_{-\infty}^{\infty} A(f-f_1)\ B(f_1)\ df_1$$

-47-

Based on the definition of convolution and the relationship described above, we can express the Fourier transform of $\tilde{u}^2(t)$ as

$$\tilde{U}\tilde{U}(f) = F\{\tilde{u}(t)\ \tilde{u}(t)\} = \tilde{U}(f) * \tilde{U}(f) = \int_{-\infty}^{\infty} \tilde{U}(f-f_1)\ \tilde{U}(f_1)\ df_1$$

or

$$\tilde{U}\tilde{U}(f_i) = \sum_{f_j=-10.0}^{10.0} \tilde{U}(f_i-f_j)\ \tilde{U}(f_j)\ \Delta f \qquad (4.31)$$

where $i = 1, 128$, $f_1 = 0.078$ Hz, $f_{128} = 10.0$ Hz, $\Delta f = 0.078$ Hz

The procedure for calculating $Qu_{\tilde{u}^2\eta}(f)$ can be summarized as follows. The spectral average $<U(f)^* \Pi(f)>$, Fourier components $\Pi(f)$ and the average wave spectrum $<\Pi^*(f)\ \Pi(f)>$ are calculated first in order to approximate the Fourier components of wave-induced velocity $\tilde{U}(f)$. Then the Fourier component of $\tilde{u}^2(t)$, i.e., $\tilde{U}\tilde{U}(f)$, can be evaluated by equation (4.31) and hence the cross spectrum between $\tilde{u}^2(t)$ and $\eta(t)$, i.e., $\tilde{U}\tilde{U}^*(f)\ \Pi(f)$. Finally, the quadrature spectrum $Qu_{\tilde{u}^2\eta}(f)$ is determined by the imaginary part of the cross spectrum $\tilde{U}\tilde{U}^*(f)\ \Pi(f)$. After determining $Qu_{(u-\overline{u})^2\eta}(f)$ and $Qu_{\tilde{u}^2\eta}(f)$, the mean momentum transfer from wind to waves due to the wave-induced turbulent stresses $\rho_a \overline{\tilde{u'}^2\ \partial\eta/\partial x}$ can be calculated by equation (4.30).

The third term $-\rho_a \overline{u'v'}$ can be rewritten by applying the properties of $\overline{\tilde{u}\ v'} = 0$ and $\overline{\tilde{v}\ u'} = 0$ and the relations $u = \overline{u} + \tilde{u} + u'$ and $v = \overline{v} + \tilde{v} + v'$, namely,

$$-\rho_a \overline{u'v'} = -\rho_a[\overline{(\tilde{u} + u')\ (\tilde{v} + v')} - \overline{\tilde{u}\tilde{v}}]$$

$$= -\rho_a[\overline{(u - \overline{u})\ (v - \overline{v})} - \overline{\tilde{u}\tilde{v}}] \qquad (4.32)$$

-48-

The total Reynolds stresses $\overline{(u - \overline{u})\,(v - \overline{v})}$ can be calculated by multiplying the time signals of $u(t)$ and $v(t)$ after removing their mean values. The wave-induced Reynolds stresses $\overline{\tilde{u}\tilde{v}}$ can be evaluated by integrating the real part of the cross spectrum of $\tilde{u}$ and $\tilde{v}$, i.e., $\mathrm{Re}\{\tilde{U}^{*}(f)\,\tilde{V}(f)\}$ or $\mathrm{Co}_{\tilde{u}\tilde{v}}(f)$, over the interested frequency range. Thus,

$$\overline{\tilde{u}\tilde{v}} = \int \mathrm{Re}\{\tilde{U}^{*}(f)\,\tilde{V}(f)\}\,df$$

$$\simeq \sum_{f_i = 0.078}^{10.0} \mathrm{Co}_{\tilde{u}\tilde{v}}(f_i)\,\Delta f \tag{4.33}$$

where $\mathrm{Co}_{\tilde{u}\tilde{v}}(f)$ is the cospectrum of $\tilde{U}^{*}(f)\,\tilde{V}(f)$. Similarly, the assumptions of $\tilde{U}(f) \simeq \langle U(f)\,\pi^{*}(f)\rangle\,\pi(f)\,/\,\langle \pi^{*}(f)\,\pi(f)\rangle$ and $\tilde{V}(f) \simeq \langle V(f)\,\pi^{*}(f)\rangle\,\pi(f)\,/\,\langle \pi^{*}(f)\,\pi(f)\rangle$ are employed to calculate $\tilde{U}^{*}(f)\,\tilde{V}(f)$.

The mean momentum transferred into waves M_w can be determined by the sum of equations (4.29) and (4.30). The total mean momentum transferred across the wind-wave interface $M_w + M_c$ can be determined by the sum of equations (4.29), (4.30) and (4.32). Finally, the value γ can be evaluated by taking the ratio of M_w over $(M_w + M_c)$.

4.2.9 Mean Velocity Profile and Friction Velocity

The mean velocity profiles were calculated by equation (3.1) using the averaged outputs of the pitot-static tube. Many experimental investigators in both laboratory and field have shown that the mean

velocity profile u/u^* is logarithmic with u_*y/ν and may be represented by

$$\frac{u}{u_*} = \frac{1}{\kappa} \ell n \frac{u_*y}{\nu} + c \tag{4.34}$$

where y is the distance measured from mean water surface, $\kappa = 0.4$ is von Karman constant, and ν is the kinematic viscosity of air. The friction velocity u_* and constant c were determined by a least square fit from the experimental data. The measured velocity profiles are shown in Figures 4.1 and 4.2. The velocity profiles near the water surface deviate from the assumed logarithmic distribution, due mainly to the effects of the waves. Similar results were also found by Wu (1968), Sutherland (1967) and Chao, et al. (1976). Consequently, the data in this region were excluded in the least square fit. Only the data in the central portion of the profiles were used to determine u_*.

4.2.10 Equilibrium Constant, Spectral Peak Frequency, and Total Energy of Wave Spectrum

Phillips (1958) found that the functional form of the wave spectrum in the equilibrium range can be represented as

$$E(f) = \alpha \, g^2 \, f^{-5} \quad \text{or} \quad E(\omega) = \alpha' \, g^2 \, \omega^{-5} \tag{4.35}$$

where $\alpha' = \alpha(2\pi)^4$ is a constant, g is gravitational acceleration, and $\omega = 2\pi f$.

The constant α in this study was calculated by two different

-50-

methods. The first method is to use the least square fit of the measured wave height spectrum $E(f)$ to equation (4.35) in a given frequency range. Pierson (1959) and Sutherland (1967) found that the appropriate frequency range is that lying between the second harmonic of the dominant wave frequency and the highest limiting frequency of the gravity wave spectrum. The maximum frequency of a gravity wave spectrum in this study is about 10 Hz. The second method is based on an average technique. Since α equals $E(f) / (g^2 f^{-5})$, a series of α values can be obtained as a function of frequency f in the equilibrium range of a given gravity wave spectrum. Then an average value of α can be obtained over the range of the frequencies. The results obtained from both techniques are presented in next chapter.

The spectral peak frequency of each wave spectrum is the frequency at which the spectral density is a maximum. A simple relationship that exists between the peak frequency f_m and fetch x may be expressed as

$$\hat{f}_m = c_1 \hat{x}^{-n} \tag{4.36}$$

where $\hat{f}_m = f_m u_* / g$ is the nondimensional peak frequency and $\hat{x} = x g / u_*^2$ is the nondimensional fetch. The constant c_1 and the exponent n were determined by a least squares fit of the experimental data.

Similarly, a simple relationship between the total energy $\varepsilon = \int_0^\infty E(f)\, df$ in a wave spectrum and the fetch also exists and can be represented in nondimensional form as

-51-

$$\hat{\epsilon} = c_2 \; \hat{x}^m$$

where $\hat{\epsilon} = \epsilon \; g^2 / u_*^4$ is the nondimensional total energy of the wave spectrum and $\hat{x}$ is the nondimensional fetch. Again the constant c_2 and the exponent m were determined from the experimental data by a least squares fit.

5. PRESENTATION, COMPARISON, AND DISCUSSION OF RESULTS

In this chapter, the general characteristics of the wave, wind and wave-induced fields are presented first. Then, the major subjects of this study including the energy and momentum transfer from wind to waves, nonlinear wave-wave interactions and white-capping dissipation are given. The comparison and discussion of the results are also provided in each section.

5.1 Characteristics of the Wave Field

5.1.1 Wave Height Spectrum

The measured power spectra of wave height at five stations along the channel are shown in Figure 5.1 (a), (b), (c) for three wind velocities 7.09, 8.01 and 8.88 m/sec. The mean wind velocities were measured at a fetch of 12.61 m. All the spectra have the common characteristics of a steep forward face, a sharp peak at the dominant frequency, and the second hump at the second harmonic.

Since the waves are growing along the channel, stations at larger fetch have a higher spectral peak implying more energy per frequency band. The normalized total wave energy $\hat{\epsilon}$ for three wind speeds as a function of the normalized fetch $\hat{x}$ is presented in Figure 5.2 (a). The least square fitted curve indicates the approximately linear relationship between the normalized total wave energy and the normalized fetch, i.e., $\hat{\epsilon} \propto \hat{x}^{1.23}$. This curve is comparable with other measurements carried out both in the ocean and laboratory. Our experimental results were also plotted in Figure 5.3 (b) whose form was

-53-

introduced by Hasselmann, et al. (1973), for comparison.

The spectral peak frequencies shift from high to low frequency along the channel as shown in Figure 5.1. Similar behavior also occurs in the ocean wave spectrum measured at a fixed location with increasing wind or measured along the fetch in the direction of wave propagation for a fixed wind speed. This effect is shown later to be caused by the nonlinear wave-wave interaction mechanism which transfers energy from the intermediate frequency to the lower frequency range. The non-dimensional spectral peaks $\hat{f}_m$ as a function of nondimensional fetch $\hat{x}$ are presented in Figure 5.2 (b). Figure 5.3 (c) shows also the comparison of our laboratory data for $\hat{f}_m$ vs. $\hat{x}$ with field data. Most of the results indicate that the normalized spectral peak $\hat{f}_m$ is proportional to the -0.33 power of the normalized fetch $\hat{x}$, i.e., $\hat{f}_m \propto \hat{x}^{-0.33}$. The present data can be also fitted to this relationship very well, although the best curve fit results in $\hat{f}_m \propto \hat{x}^{-0.44}$. Finally, according to the previous and present results of $\hat{\epsilon}$, $\hat{f}_m$ and $\hat{x}$, the fetch dependence of $\hat{f}_m$ and $\hat{\epsilon}$ is established.

The variations of some spectral components (1.5 Hz to 10 Hz) of the wave at five stations are shown in Figure 5.4 for wind speeds of 7.09, 8.01 and 8.88 m/sec. The graphs indicate that the frequency components equal to or less than 2.5 Hz are still growing and not yet saturated. The components larger than 2.5 Hz are sometimes growing and sometimes decaying, which reveals the exchange of energy among different wave components associated with the nonlinear wave-wave interactions. Not much variation was found for the frequency compo-nents larger than 10 Hz which is in the capillary wave range.

5.1.2 Equilibrium Constant of Wave Height Spectrum

The growth of waves under the action of wind can not continue indefinitely. The existing experimental data for wind wave spectra obtained in both the laboratory and the field indicate that there exists a "saturated" or equilibrium range at high frequency. Phillips (1966) argued that there are two possible physical reasons which prohibit the growth of the wave spectrum and lead it to an equilibrium state. First, if the waves become too steep, local instability causes the wave to break. Consequently, energy is lost from the wave field. The appearance of intermittent patches of white caps on the ocean surface indicates the local instability leading to wave breaking. Another mechanism for the limitation of wave growth arises from the formation of capillary waves in the front of steep primary waves. The lower limit of the frequency of a capillary wave is about 10 Hz. Therefore, the frequency range of the equilibrium portion of a wave spectrum is between the frequency of the second harmonic in the wave spectrum (Pierson, 1959) and 10 Hz. Figure 5.1 shows the wave spectrum at five stations along the channel for three wind speeds of 7.09, 8.01 and 8.88 m/sec and indicates the existence of this equilibrium range.

Based upon purely dimensional consideration, Phillips (1958) proposed equation (4.35) representing the one-dimensional equilibrium range spectrum. Furthermore, Phillips found α to be a universal constant based on the existing wave spectra data. On the other hand, recent JONSWAP ocean spectrum data (Hasselmann, et al, 1973) indicated that the equilibrium range of an ocean spectrum is represented

-55-

by the energy balance between the energy input from turbulent air, the white capping or wave breaking, and nonlinear wave-wave interactions. Hasselmann (1974) proposed the dissipation by white capping as $S''(\vec{k}) = - d \ (2\pi f) \ E(\vec{k})$, and found the equilibrium range of a wave spectrum can be approximated by f^{-5}.

The values of α in the equilibrium range wave spectrum were determined by two different methods as discussed in Section 4.2.10. Figure 5.2 (c) shows the variation of α as a function of non-dimensional fetch, $\hat{x}$. It indicates that α is not a universal constant and is definitely fetch dependent. The experimental results indicate $\alpha \propto \hat{x}^{-0.65}$. The same set of data ($\alpha$ vs. $\hat{x}$) was replotted in Figure 5.3 (a) for comparison with the results of other investigators. This set of data is in the region of small non-dimensional fetch and compares quite favorably with other existing data.

From the results of Section 5.1.1 and this section, we find the nondimensional peak frequency $\hat{f}_m$, nondimensional total wave energy $\hat{\epsilon}$, and Phillips equilibrium constant α to be fetch dependent. The best curve fit for these variables with respect to the nondimensional fetch $\hat{x}$ yield

$$\hat{f}_m \propto \hat{x}^{-0.44}, \qquad \hat{\epsilon} \propto \hat{x}^{1.23} \quad \text{and} \quad \alpha \propto \hat{x}^{-0.65}$$

For a self-similar spectrum $\hat{\epsilon} \sim \alpha \hat{f}_m^{-4}$; accordingly, the relationship among $\hat{f}_m$, $\hat{\epsilon}$ and α can be constructed and the exponents n_f, n_ϵ and n_α in the power laws for $\hat{f}_m$, $\hat{\epsilon}$ and α should satisfy the following relation:

$$4n_f - n_\alpha + n_\epsilon = 0$$

Here $n_f = -0.44$, $n_\alpha = -0.65$, and $n_\epsilon = 1.23$ for the present
experimental results. Substituting these values into the above rela-
tion yields

$$4 \, (-0.44) - (-0.65) + 1.23 = 0.12$$

The resultant value 0.12 lies within the error of about ± 0.24 esti-
mated from the individual error band of each curve fitted exponent.
Finally, based on the JONSWAP's (Hasselmann, et al. 1973) and the
present results of the relationships of $\hat{f}_m$, $\hat{\epsilon}$ and α to $\hat{x}$, the
fetch dependence of $\hat{f}_m$, $\hat{\epsilon}$ and α is again established.

5.2 Characteristics of the Wind Field

The mean velocity profile and the power spectra of the fluc-
tuating velocity components u' and v' characterize the mean and
fluctuating wind fields. The mean air velocity profiles were
presented in Figures 4.1 and 4.2. The vertical line in the upper
part of the profile is the free stream region. The central part
represents the logarithmic region of a typical turbulent velocity
profile. The lower region of the velocity profile close to the air-
water interface deviates from the logarithmic profile. There the
velocity magnitudes are larger than those represented by a logarith-
mic law. The deviation from a conventional logarithmic profile
and the increase in magnitude may be caused by the generation of the

surface drift current. Consequently, the friction velocity u_* was evaluated from the best fit of equation (4.34) based on the experimental data in the logarithmic region. The calculated results of u_* are tabulated in Table (5.1).

The power spectra of the turbulent velocity components u' and v' were evaluated from the experimental data taken closest to the air-water interface (i.e., 0.508 cm above the highest wave) and sampled at a rate of 5000 Hz for a duration of five minutes. The spectra were normalized with respect to their respective variance and are shown in Figures 5.5 to 5.8. Figures 5.5 (a), (b), and (c) and 5.6 (a), (b), and (c) represent the u' and v' normalized power spectra for three wind speeds at the two fetches of 6.51 m and 15.66 m, respectively. The u'-component is consistently larger than the v'-component in the lower frequency range. However, for frequencies higher than approximately 20 Hz, the trend is reversed. Figures 5.7 (a) and (b) show the comparison of the normalized u' and v' spectra for three different wind speeds at the two fixed fetches of 6.51 m and 15.66 m, respectively. Both the u' and v' spectra are independent of wind speed in the inertia subrange where the -5/3-law holds. However, such is not the case in the high frequency range. In order to reveal more details of the spectra variation in the high frequency range, the u' and v' component spectra were replotted for a fixed wind speed at 5 different fetches as shown in Figures 5.8 (a), (b), and (c). The spectra indicate that there is a consistent fetch dependence for all wind speeds tested.

-58-

According to a discussion of the general behavior of a turbu-
lence power spectrum by Hinze (1975), the low frequency portion of
a turbulence spectrum is governed by the characteristics of the large
eddies and is dependent on the conditions of the formation of the
spectrum. On the other hand, the high frequency portion of a
turbulence power spectrum is governed by the turbulence energy and
viscous dissipation and is independent of the condition of the for-
mation of the spectrum. The normalized power spectra presented in
Figures 5.5 to 5.7 are used to study the direct wave effect on the
turbulence. As indicated in Figures 5.5 to 5.7, the u'-component
spectrum seems not to be affected by the wave. The spectrum shape
of u' is proportional to f^{-1} and is consistent with the results
of Tchen's (1953) study of turbulent kinetic energy in a shear flow.
The eddy diffusivity determined by larger eddies might be regarded
as a governing parameter in determining the characteristics of the
turbulence spectrum. Upon examination of the wind wave spectrum as
shown in Figure 5.1, the range of the wave frequency (f < 10 Hz)
is in the low frequency portion of the turbulent spectrum. The
non-dimensional v'-component spectrum deviates consistently from
the f^{-1} law, and a spectral peak appears around the dominant wave
frequency. It shows the strong wave effect on the v'-component
spectrum and reveals the significant contribution of the wave to the
formation of v'-component spectrum in the low frequency range.
Similar results were obtained by Young, et al. (1973) and McIntosh,
et al. (1975).

In the inertial subrange where the spectra obey the $f^{-5/3}$ law,

-59-

the total energy supply to the turbulence is practically equal to the total viscous dissipation. It is clear in Figures 5.7 (a) and (b) that such equilibrium conditions were established for both u' and v' components (20 Hz < f < 500 Hz) along the channel [6.51 m, short fetch; 15.66 m, largest fetch] at all three wind speeds. In addition, the existence of the log-region of the mean velocity profile as shown in Figures 4.1 and 4.2 is consistent with the existence of the inertial subrange of the u' and v' turbulence power spectra. For frequencies higher than those of inertial sub-range, the power spectra decays as f^{-7} if the viscous dissipation is the only governing parameter. It can be seen clearly from Figures 5.8 (a), (b), and (c) that the measured spectra have not reached the viscous dissipation range as evidenced by their spectra decay rate. The measured spectra depend on fetch at all wind speeds.

5.3 Characteristics of the Wave-Induced Field

The wave-induced field is represented by the power spectra of the wave-induced velocity components $\tilde{u}$ and $\tilde{v}$ and the wave-induced pressure $\tilde{p}$, as well as the coherence and phase difference between wave height η and these wave-induced quantities. The power spectra of wave-induced velocity components $\tilde{u}$ and $\tilde{v}$ and the wav-induced pressure are calculated from equations (4.8) and (4.11) respectively. The coherence and phase relations between η and $\tilde{u}$ and $\tilde{v}$ are obtained from equations (4.3) and (4.4), whereas the coherence and phase relations between η and $\tilde{p}$ are calculated by equations (4.17) and (4.18). Because all of the plots are similar, typical

-60-

sets of these data taken at 0.508 cm above the highest waves at a
short fetch of 6.51 m and at the longest fetch of 15.66 m for three
wind speeds of 7.09, 8.01 and 8.88 m/sec are shown in Figures 5.9 to
5.14.

The power spectra of wave-induced pressure and fluctuating
velocities have shapes similar to that of the wave height spectrum
as shown in parts (a) and (b) of these figures. Therefore, the flow-
field near the wave surface is strongly coupled to the interfacial
wave motion.

The first and second peaks in the coherence spectra, as shown
in parts (c), (d), and (e) of these figures, are associated with the
corresponding harmonics of the wave spectrum. These indicate the
strong coupling between the wave-induced field and wave motion at the
dominant wave frequency (first harmonic) and its second harmonic.
In addition, the high values of coherence imply that the measured
phase relationships between the wave-induced quantities and the wave
motion are reliable. As shown in parts (c), (d) and (e) of these
figures, the phase angles are nearly constant near the wave dominant
frequencies. The phase angles scatter beyond the dominant fre-
quencies. The weak interactions between the two flowfields may be
responsible for the phase angle scatter. The coherences of $\tilde{p}$, $\tilde{u}$
and $\tilde{v}$ with respect to η ranged from 0.70 to 0.95, 0.54 to 0.84
and 0.87 to 0.95, respectively, at the dominant frequency along the
channel for all cases. The plots of coherences R against non-
dimensional fetch $\hat{x}$ are shown in parts (a), (d) and (e) of Figure
5.15. It was found that the coherences between η and $\tilde{p}$ and η

-61-

and $\tilde{u}$ increase very slightly with increasing $\hat{x}$, whereas the co-
herences between η and $\tilde{v}$ are almost fetch independent. The
coherences of $\tilde{v}$ and $\tilde{p}$ with respect to η are larger than that
of $\tilde{u}$ with respect to η. It can hardly be explained by the
present data. One possible reason may be due to the effect of the
interactions among the mean air, wave-induced and turbulence fields.
Further study about these interaction fields is needed in order to
fully understand the dynamic structure of the air-sea interface.

It can be seen from the parts (c), (d), and (e) of Figures
5.9 to 5.14 that the phase angles between $\tilde{p}$, $\tilde{u}$ and $\tilde{v}$ with
respect to η are consistent along the channel (from $x = 6.51$ m
to $x = 15.66$ m) at all wind speeds, namely $\tilde{p}$ leads η by 220°
to 230° (or $\tilde{p}$ lags η by 130° to 140°), $\tilde{u}$ leads η by 10° to
40° (or $\tilde{u}$ lags η by 320° to 350°) and η leads $\tilde{v}$ by 65° to
75° (or η lags $\tilde{v}$ by 285° to 295°). The experimental data for
the phase angles between η and $\tilde{p}$, $\tilde{u}$ and $\tilde{v}$ at the dominant
wave frequency along the channel were shown in parts (b), (c) and (f)
of Figure 5.15. It seems that the phase angles between wave and
wave-induced fields are independent of the nondimensional fetch, $\hat{x}$.
According to potential flow theory, the fluctuating pressure at the
water surface of sinusodial waves propagating in the same direction
as a uniform wind field is (Lamb 1932, §232)

$$\tilde{p} = - \rho_a g \eta [1 + (1 - u_{\infty} / c)^2]$$

where u_{∞} is the mean equivalent uniform wind speed and c is the

-62-

phase speed of the waves. This expression predicts a 180° phase difference between η and $\tilde{p}$ for a potential flow. An experimental data for the phase angle between η and $\tilde{p}$ agrees well with the field data obtained by Dobson (1971) and Elliott (1972), i.e., $\tilde{p}$ leads η by 225° on the average. Figure 5.16 shows the comparison of the phase angle data of $\tilde{p}$ with existing experimental results obtained both in the field and laboratory. Although the data are scattered, a data trend was found. It indicates that the phase differences between η and $\tilde{p}$ approach 180° for large c/u_* (lower wind speed) and tend to deviate from 180° for smaller c/u_* (higher wind speed). The difficulty in obtaining accurate experimental phase angles and the possible effect of variable turbulence characteristics on wave-induced field may be responsible for the scatter of the experimental data in the higher wind speed range. The phase angle between η and $\tilde{u}$ and η and $\tilde{v}$ close to wave surface could be derived from the boundary conditions at the wave surface (Yu, et al.,1973). The results are that η leads $\tilde{u}$ and $\tilde{v}$ by 180° and 270°, respectively, inside the critical layer (i.e., small values of u_∞/c) where the mean wind velocity equals the phase speed of wave, whereas η leads $\tilde{u}$ and $\tilde{v}$ by 0° and 90°, respectively, outside the critical layer (i.e., larger values of u_∞/c) (Yu, et al., 1973). Since the wind speeds of our measurement are relatively high, all the experimental results are in the range of large u_∞/c. The present phase angle results are plotted in Figure 5.17 and compared with those of Yu, et al., 1973. Although Yu's data was obtained in a wave-following system over

-63-

artificially-generated simple progressive water waves, there is good
agreement seen if Yu's data are extended to the region of large
u_∞/c. Again, the results deviate from the theoretical predictions
based on the boundary condition at the air-water interface (i.e.,
η leads $\tilde{u}$ and $\tilde{v}$ by 0° and 90° for large u_∞/c ratio).
Experimental difficulties preclude us from measuring true pressures
at the air-water interface. The distance of the pressure probe to
the interface may cause such deviations from the theoretical esti-
mates.

5.4 Energy Transfer from Wind to Waves

The energy transfer from wind to waves is through the work
done by the normal wave-induced pressure $\tilde{p}$, wave induced turbulent
Reynolds stresses $\widetilde{u'v'}$ and $\widetilde{v'v'}$, and the mean turbulent Reynolds
stresses $\overline{u'v'}$ acting on wave surface as shown in equation (D.12)
of Appendix D. The results of calculation based on the experimental
data were tabulated in Table (D.1). The energy transferred to the
wave field due to the normal pressure term is calculated from equa-
tion (4.19) and all other terms are calculated by employing a tech-
nique similar to that for calculating momentum transfer and described
in Section 4.2.8. Based on the results shown in Table (D.1), we
found that the major source of energy to the wind-generated wave is
from the normal pressure $\tilde{p}$ [column heading (1) in Table (D.1)].
The contributions from the wave-induced and mean turbulent Reynolds
stresses [column headings (2), (3) and (4) in Table (D.1)] are ex-
tremely small (approximating 2.5% of the total energy transferred to

-64-

the wave field). The surprising result is that the terms represented by the contribution of energy to the wave field due to $\widetilde{u'v'}$ and $\widetilde{v'v'}$ are negative. This implies that the energy is extracted from the wave field and transferred to the wind. This result can not be explained at the present, but may be attributed to the accuracy of the calculation of these small higher-order terms. As indicated in the Appendix A, the accuracy of calculation of such terms is about 30%. But according to the reasonable trend of the results of $-\rho_a \overline{\widetilde{u'v'\tilde{u}}}$, $-\rho_a \overline{\widetilde{v'^2\tilde{v}}}$ and $\rho_a \overline{u'v' \, \partial\eta/\partial x \, \tilde{v}}$ [column headings (2), (3) and (4) in Table (D.1)] with increasing free stream wind velocity u_∞ and fetch, we can see the order of magnitude of these terms is reliable, and hence the contribution of these terms to the energy transfer from wind to waves is negligible. Therefore, we can conclude that almost all the energy transfer from wind to waves is due to the normal pressure acting on water surface.

The calculated results of γ_E, which is the ratio of the energy transferred into waves over the energy transferred into water, are tabulated in Table (D.1) for different wind speeds and fetches. It seems that γ_E is independent of free stream wind speed and fetch. The calculated average value of γ_E is 0.89 which means about 89% of the energy transferred into water goes to the wave field directly and the remaining 11% of the energy goes to the drift current field. This analysis is based on the assumption of the drift current velocity equals 3% of the free stream wind velocity due to the lack of experimental results for drift current velocity in our channel.

Based upon the measured pressure $p_m(t)$ and the waves $\eta(t)$,

-65-

the spectral density of energy and momentum transfer from wind to waves through the normal pressure acting on wave surface can be calculated by equations (4.19) and (4.20), respectively. The results are shown in Figures 5.18 and 5.19. Again the experimental results are similar along the channel, and only two representative sets of data at a small fetch (6.51 m) and a longer fetch (15.66 m) are shown. Both spectral distributions have a shape similar to that of the wave spectrum with a peak at the dominant wave frequency and a small hump at the second harmonic. Therefore, most of the energy and momentum transfer occurred around the dominant frequency of the wave spectrum. The magnitude of these results are of the same order as Dobson's (1971) which were obtained in the ocean.

5.5 Energy Transfer of Nonlinear Wave-Wave Interactions

5.5.1 Theoretical Results of Nonlinear Wave-Wave Interactions

The nonlinear wave-wave interaction mechanism proposed by Hasselmann (1962) is conservative and can redistribute energy among various frequencies in a given wave spectrum. The theoretical expression of the rate of energy transfer due to this nonlinear mechanism is a triple integral expression, equation (2.9). As discussed previously, Barnett's parametric equation was used to approximate the theoretical results for nonlinear wave-wave interactions $S_{nl}(f)$. Based on the measured wind wave spectra, the theoretical $S_{nl}(f)$ calculated from equations (2.17), (2.18) and (2.19) are shown in part (a) of Figures 5.20 to 5.31. This series of figures is presented following the order of decreasing wind speed and decreasing

-66-

fetch. The spectral distribution of $S_{n1}(f)$ consists of three regions: a positive and relatively low frequency region, a negative and intermediate frequency region, and a positive and relatively high frequency region. This implies that the energy transfers are away from intermediate frequency region to the lower and higher frequency regions in a wave spectrum.

In order to discuss the results of $S_{n1}(f)$ further, the results of the net rate energy transfer $S(f)$ are presented. The spectral distribution of $S(f)$ is similar to that of $S_{n1}(f)$, namely, positive transfer in a relatively low frequency region and negative transfer in the intermediate frequency region as shown in part (a) of Figures 5.20 to 5.31. The results for $S(f)$ were calculated from equation (2.5) and based on the measured wave spectrum $E(f)$ along the fetch. This net rate energy transfer as shown in equation (2.5) is the sum of the rate of energy transfer due to air-input $S_{in}(f)$, nonlinear wave-wave interactions $S_{n1}(f)$, and white-cap dissipation $S_{ds}(f)$. The resulting positive transfer for $S(f)$ in the relatively low frequency region and negative transfer for $S(f)$ in the intermediate frequency region indicate a shifting of wave energy from intermediate frequencies to the low frequency region along the direction of wave propagation as shown in Figure 5.1. The spectral distribution of $S(f)$ is consistent with the observed wave spectrum establishment along a fetch for constant wind or at a fixed fetch with increasing wind. Since the air-input $S_{in}(f)$ and white-cap dissipation $S_{ds}(f)$ are purely positive and negative transfers, respectively, in all frequency regions and because the nonlinear

-67-

wave-wave interaction $S_{n1}(f)$ has a similar spectral distribution to $S(f)$, the nonlinear wave-wave interactions mechanism must be responsible for the energy shift from intermediate frequencies to low frequencies. Consequently, this stresses the importance of $S_{n1}(f)$ to wave growth in any relevant frequency region.

The parametric equation results of $S_{n1}(f)$ are examined in the previously mentioned three regimes. In the relatively low frequency region, the peaks for both positive energy transfer of $S_{n1}(f)$ and $S(f)$ are approximately at the same frequency, except for two cases of short fetch (3.48 m to 6.51 m) with wind speeds of 7.09 and 8.01 m/sec as shown in part (a) of Figures 5.30 and 5.31, respectively. This miss match in frequency implies that the parametric equation can not predict $S_{n1}(f)$ well at the short fetch, as $S_{n1}(f)$ is compared with the measured $\hat{S}_{n1}(f)$. Although Barnett (1966) indicated that the parametric equation is developed for the fully developed sea ; it is also applicable for the partially developed sea . Since the two cases are in the very initial stage of the wave generating zone, the fetches are too short to reach the applicable range of the parametric equation. For all other cases the parametric equation is indeed to be able to predict $S_{n1}(f)$ sufficiently well in the relatively low frequency region.

In the intermediate frequency region, the negative peak of $S_{n1}(f)$ and the positive peak of $S_{in}(f)$ (or $E(f)$) occur at the same frequency as shown in Figures 5.20 to 5.31. Since the net transfer $S(f)$ is the algebric sum of $S_{in}(f)$, $S_{n1}(f)$ and $S_{ds}(f)$

-68-

and the negative transfer of $S_{ds}(f)$ is always smaller than the positive transfer from wind to waves $S_{in}(f)$ as shown in part (b) of Figures 5.20 to 5.31, the nonlinear energy transfer $S_{nl}(f)$ can be attributed largely to the negative transfer of $S(f)$ in the intermediate frequency region. Consequently, the energy transferred from wind to waves in a intermediate frequency region is always transferred to both the relatively low and high frequency regions throught the mechanism of nonlinear wave-wave interactions. In general, the parametric equation results are quite adequate and acceptable as pointed out by Barnett (1966) and Mitsuyasu (1968b) and evidenced by the results of this study.

The relatively high frequency region seems to begin with the frequency at which the net energy transfer $S(f)$ equals zero. This implies that the positive energy transfer of $S_{in}(f)$ and $S_{nl}(f)$ is balanced by the negative transfer of $S_{ds}(f)$ in the relatively high frequency region. The calculated results for $S_{nl}(f)$, based on Barnett's parametric equation, were shown in part (a) of Figures 5.20 to 5.31. The calculated values of $S_{nl}(f)$ are too large to satisfy the conservative requirement of the nonlinear wave-wave interaction mechanism (Mitsuyasu, 1968b). To avoid overestimating $S_{nl}(f)$ by Barnett's parametric equation in the relatively high frequency region, one can use the conservative nature of the nonlinear wave-wave interaction mechanism. A suggested method is to use the parametric equation to calculate the sum of the energy transfer in the relatively low frequency and intermediate frequency regions where the spectral value of $S_{nl}(f)$ changes from negative to positive, say

-69-

at a frequency f_{so}. A net negative result is expected due to the large negative transfer in the intermediate frequency region. In order to satisfy the conservative law for $S_{nl}(f)$ over all frequencies, we require a positive energy transfer equal to the negative value obtained from the previous calculation to be spread over the frequency range between f_{so} and the cutoff frequency of the wave spectrum. A smooth decay function, such as exponential decay, could be assumed for redistributing the positive energy transfer in the relatively high frequency region. With modification Barnett's parametric equation would be the most applicable method for predicting nonlinear wave-wave interaction economically and efficiently.

5.5.2 Experimental Results of Nonlinear Wave-Wave Interactions

Because we can not directly measure the energy transfer due to $S_{nl}(f)$ and $S_{ds}(f)$ separately, the experimental result of the sum of $\hat{S}_{nl}(f)$ and $\hat{S}_{ds}(f)$ was first deduced from equation (4.21) and is plotted in part (a) of Figures 5.20 to 5.31. As shown in the same graphs, the negative value of $(\hat{S}_{nl} + \hat{S}_{ds})$ at the peak frequency of the intermediate frequency region is larger than that of the parametric equation result for $S_{nl}(f)$ as expected, except one case at a fetch of 3.46 m to 6.51 m and wind speed of 8.88 m/sec (see part (a) of Figure 5.29). In order to evaluate the experimentally determined $\hat{S}_{nl}(f)$, the white-capping dissipation $S_{ds}(f)$ must be subtracted from $(\hat{S}_{nl} + \hat{S}_{ds})$. Because we can not directly measure $\hat{S}_{ds}(f)$, a theoretical model of white-capping dissipation, $S_{ds}(f)$ had to be assumed in order to obtain $\hat{S}_{nl}(f)$ from equation

(4.22). Therefore $\hat{S}_{n1}(f)$ was estimated from the measured results for $S(f)$ and $S_{in}(f)$ [from equations (2.5) and (4.19), respectively] together with Hasselmann's white-cap dissipation model for $S_{ds}(f)$ [equation (2.21)]. The results for $\hat{S}_{n1}(f)$ are shown in part (b) of Figures 5.20 to 5.31 and compared there with the theoretical results for $S_{n1}(f)$ computed by Barnett's parametric equation. In general, the qualitative comparisons are satisfactory in the relatively low and intermediate frequency regions, except for the three cases where the wind wave development at small fetch (3.46 m to 6.51 m) is at its initial stage as shown in Figures 5.27 to 5.31. The relatively high frequency components of the wind-waves at small fetch and the inadequate representation of $S_{n1}(f)$ with the Barnett's parametric equations as discussed previously may be the reasons which contribute to the disagreement for these cases.

For the cases in good agreement, both the theoretical $S_{n1}(f)$ and experimental $\hat{S}_{n1}(f)$ generally have similar positive peak frequencies, similar spectral distributions and almost the same amount of positive energy transfer in the relatively low frequency region; they also have similar negative peak frequencies and similar spectral distributions in the intermediate frequency region. The positive and negative peak frequencies of $S_{n1}(f)$ are almost the same as the positive peak frequency of $S(f)$ and peak frequency of $E(f)$, respectively.

As to a quantitative comparison of the results of $S_{n1}(f)$ and $\hat{S}_{n1}(f)$ in the intermediate frequency region, the parametric equation results for $S_{n1}(f)$ are always slightly larger (5% to 40%) than the

-71-

experimental $\hat{S}_{n1}(f)$ in the neighborhood of the negative peak frequency for the cases with the fetch larger than 6.51 m as shown in part (b) of Figures 5.20 to 5.28. These discrepencies might be caused by an overestimation by Hasselmann's white-cap dissipation model for $S_{ds}(f)$ as used in equation (4.22), resulting in an underestimation of $\hat{S}_{n1}(f)$.

The comparisons of $S_{n1}(f)$ and $\hat{S}_{n1}(f)$ in the relatively high frequency region are unsatisfactory. The experimental result for $\hat{S}_{n1}(f)$ did not indicate the expected positive transfer, but rather approached zero. It is recalled that the "experimentally" determined $\hat{S}_{n1}(f)$ was calculated from equation (4.22) and was based on the experimentally determined $S(f)$ and $S_{in}(f)$ and Hasselmann's $S_{ds}(f)$. Since the measured $S(f)$[*] is approximately zero in this relatively high frequency region as shown in the figures, $\hat{S}_{n1}(f)$ $\simeq S_{in}(f) - S_{ds}(f)$. Based on the experimentally determined $S_{in}(f)$, it seems that underestimation of $S_{ds}(f)$ in that frequency region may be responsible for $\hat{S}_{n1}(f)$ not being able to have the expected positive values of transfer. As discussed previously, unless an independent experimental determination of the dissipation function $S_{ds}(f)$ can be made, $\hat{S}_{n1}(f)$ can not be satisfactorily evaluated over all frequency ranges.

---

[*] After completion of our work and as we were writing it up, Ramamonjiarisoa and Coantic (1976) reported that laboratory wind-generated water waves with frequencies higher than the dominant wave frequency do not obey the classical deep water dispersion relationship; these waves propagate at the phase speed of the dominant wave in the spectrum. Consequently, the calculated value of $S(f)$ should be altered before further detailed comparisons at high frequencies can be made.

Based on the comparisons and discussions presented in Sections 5.5.1 and 5.5.2, we may conclude that Barnett's parametric equation might slightly overestimate the negative transfer for $S_{n1}(f)$ in the intermediate frequency region and is inadequate in the relatively high frequency region (it grossly overestimates the positive transfer). Hasselmann's white-capping dissipation model might slightly overestimate the negative transfer in the intermediate frequency region and underestimate the negative transfer in the relatively high frequency region. However, Barnett's parametric equation is applicable for calculating the energy transfer due to nonlinear wave-wave interactions in the relatively low frequency and intermediate frequency regions of a wind wave spectrum with the normalized fetch $\hat{x}$ greater than 100.

5.6 Energy Dissipation of White Capping

5.6.1 Theoretical Results of White Capping

The theoretical results for white capping energy dissipation function $S_{ds}(f)$, calculated from equation (2.21), are also shown in part (b) of Figures (5.20) to (5.31). The constant d in equation (2.21) is associated with the energy dissipation spectrum. The values of d were calculated based on the energy balance in the high frequency equilibrium range [equation (4.26)] and are tabulated in Table (5.2) for each case. The graphs clearly show the distribution of the spectral density $S_{ds}(f)$ appears similar to that of the wave spectrum as expected from equation (2.21). The dissipation function used herein has a maximum negative value at the peak frequency of the

-73-

wave spectrum and decreases on both sides of the peak frequency, finally approaching zero in the relatively low and high frequency regions. This theoretical model of $S_{ds}(f)$ was first checked by Hasselmann using JONSWAP data. Fairly good agreement was found and presented by Hasselmann (1974). Because of the lack of direct measurements of the air-input term $S_{in}(f)$, an assumed $S_{in}(f)$ was used in equation (4.23) by Hasselmann for calculating the experimental results for $S_{ds}(f)$. In this study, $S_{in}(f)$ was measured directly to give a more accurate investigation on Hasselmann's white-cap dissipation model.

5.6.2 Experimental Results of White Capping

As discussed previously, the experimental results always yield the sum of $\hat{S}_{ds}(f)$ and $\hat{S}_{nl}(f)$. In order to deduce the "experimental" results for $\hat{S}_{ds}(f)$ as indicated in equation (4.23), an assumed $S_{nl}(f)$ form has to be taken. The experimental results for $\hat{S}_{ds}(f)$ are evaluated based on the measured values of $S(f)$ and $S_{in}(f)$ and Barnett's representation of the term of $S_{nl}(f)$. The resulting $\hat{S}_{ds}(f)$ are plotted in part (b) of Figures (5.20) to (5.31) and compared with the theoretical $S_{ds}(f)$. The comparison between $\hat{S}_{ds}(f)$ and $S_{ds}(f)$ are in general satisfactory in the relatively low and intermediate frequency regions for the fetches larger than 6.51 m, except for the cases with fetches between 6.51 m and 9.48 m and 12.61 m and 15.66 m and with wind speed of 7.09 m/sec [i.e. Figures (5.28) and (5.22)], where the negative peak frequencies of $\hat{S}_{ds}(f)$ deviate from those of $S_{ds}(f)$. The deviation is probably

-74-

caused by the overestimation of $S_{n1}(f)$ based on the parametric equations in the negative peak frequency region. Consequently, the resulting value of $\hat{S}_{ds}(f)$ would be underestimated based on equation (4.23). The agreements between $\hat{S}_{ds}(f)$ and $S_{ds}(f)$ are poor in the relatively high frequency region for all cases. The inadequacy of Barnett's parametric equation in the relatively high frequency range may be responsible for the poor agreement (Mitsuyasu, 1968b). The agreements are poor for the small fetch, 3.46 m to 6.51 m, for all wind speeds; this may be attributed to the inadequacy of Barnett's parametric presentation for $S_{n1}(f)$ at small fetch where the relatively high frequency waves exist. However, generally the good agreements are shown in the relatively low and intermediate frequency regions for large fetches. From the practical point of view, Hasselmann's dissipative model due to white capping is acceptable and applicable for developing a new wave prediction scheme for the normalized fetch $\hat{x}$ larger than 100.

5.7 Mean Momentum Transfer from Wind to Waves

The mean momentum transferred from wind to water in a developing turbulent boundary layer calculated from equations (4.29), (4.30) and (4.32) is tabulated in Table (C.1). Based on these results, we found that about 65% of the momentum transferred into water goes to the wave field directly, while the remaining 35% goes to currents. The most important contributions to this momentum transfer are the normal pressure acting along the wave surface via $\overline{\tilde{p}\, \partial\eta/\partial x}$ and the wave-induced turbulent Reynolds stresses acting via $\rho_a \overline{u'u'}\, \partial\eta/\partial x$. The

-75-

former contributes about 73% of the total momentum transferred into waves, while the latter gives about 27%. Although the largest contribution of momentum to wave growth comes from the normal pressure, the contribution from turbulent effects coupled with the water waves can not neglected. Therefore, the turbulent-wave interaction must be taken into account for the momentum transfer in formulating wind-wave generation theory.

Since the phase relations between pressure and wave are stable and organized over a frequency range around the dominant frequency of the wave spectrum as shown in Figure 5.15 (f), there is an efficient momentum transfer for each frequency component. On the other hand, the result of calculating $\rho_a \overline{\widetilde{u'u'} \, \partial\eta/\partial x}$ for the momentum contribution to the wave field indicated an unstable phase relationship with the wave height, resulting in random fluctuating values varying from positive to negative throughout the frequency range. Since the quantity $\widetilde{u'u'}$ is a wave-induced quantity and closely correlated with the wave spectrum, it yields a net positive transfer to the wave field.

The averaged ratio γ of momentum transferred into waves over the total momentum transferred into water is about 0.65. Since the equation used (Appendix C) in obtaining the present results is derived in a developing turbulent boundary layer, the mean pressure gradient in the wave tank has already been taken into account. In fact, the mean pressure gradient in our wave tank is small. It makes our results comparable with the field results. As shown in Figure 5.15 (b), the value of γ varied from 0.53 to 0.75 along

-76-

the fetch and seems to approach a constant value of approximately 0.70 at large fetch. It may be inferred then that approximately 70% of momentum transferred across the interface goes directly to the wave field for fully developed wind waves.

Dobson's (1971) expression of γ for the fully developed boundary layer is

$$\gamma = -\overline{[(\tilde{p}\,\frac{\partial \eta}{\partial t})/c]} \; / \; [-\rho_a \overline{(\tilde{u}+u')\,(\tilde{v}+v')}]$$

$$= -\frac{2\pi f}{g}\,\overline{\tilde{p}\,\frac{\partial \eta}{\partial t}} \; / \; [-\rho_a \overline{(\tilde{u}\tilde{v}+u'v')}]$$

which is different from the present expression derived in Appendix C, viz.,

$$\gamma = (\overline{\tilde{p}\,\frac{\partial \eta}{\partial x}} + \rho_a \overline{u'u'\,\frac{\partial \eta}{\partial x}}) \; / \; (\overline{\tilde{p}\,\frac{\partial \eta}{\partial x}} + \rho_a \overline{u'u'\,\frac{\partial \eta}{\partial x}} - \rho_a \overline{u'v'})$$

Since $\overline{\tilde{p}\,\frac{\partial \eta}{\partial x}}$ is equal to $-\frac{2\pi f}{g}\,\overline{\tilde{p}\,\frac{\partial \eta}{\partial t}}$ and $\overline{\tilde{p}\,\frac{\partial \eta}{\partial x}}$ is also equal to $-\rho_a \overline{\tilde{u}\tilde{v}}$ for the inviscid larminar flow as indicated by Phillips (1966), therefore, the only difference in the above two expressions of γ is the appearance of $\rho_a \overline{u'u'\,\frac{\partial \eta}{\partial x}}$ in the present γ. The neglection of this term which is a result of the interaction between turbulent and wave-induced fields could cause the overestimation of Dobson's γ value [average value of γ is 1.1].

Instead of direct measurement, JONSWAP (1973) calculated γ value based on the momentum balance scheme of a wind wave spectrum. These values of γ varied from 0.1 to 0.8 as discussed in

-77-

Section 1.1. However, the Dobson (1971) and JONSWAP (1973) field data gave a γ value of about 0.8 for a normalized fetch in the range of $\hat{x} \simeq 10^5$. The present γ results varied from 0.53 to 0.75 and seemed to approach a constant value close to 0.7 for normalized fetches larger than 100. We believe that the experimental results of Wu (1968) and Barnett (1971) and Phillips estimate (1966) are inconsistent with the present data and the field data of Dobson's and JONSWAP's. Because our experimental conditions were better controlled than other investigators' and our calculated γ values are based on an equation consistent with our experimental conditions, we confidently conclude that about 70% of the total mean momentum transferred across the air-water interface goes directly to the wave field in the fetch range of $100 < \hat{x} < 500$, with a reasonable assurance that this result can be extrapolated to larger $\hat{x}$ values.

6.   CONCLUSIONS AND RECOMMENDATIONS

6.1 Conclusions

Based on the presentation, comparison and discussion of the present results in Chapter 5, the following conclusions can be drawn:

(1) The present experimental data, as well as the preexisting data, indicate that the nondimensional peak frequency $\hat{f}_m$, nondimensional total energy $\hat{\varepsilon}$, and the equilibrium constant α of a wave spectrum depend on nondimensional fetch $\hat{x}$, e.g., $\hat{f}_m \propto \hat{x}^{-0.33}$, $\hat{\varepsilon} \propto \hat{x}^{1.23}$ and $\alpha \propto x^{-n}$, where n varies from 0.22 to 0.65 according to the available data. Since these parameters satisfy the requirement of a self-similar spectrum, i.e., $\hat{\varepsilon} \sim \alpha \hat{f}_m^{-4}$, with better understanding of these parameters we will be able to derive an appropriate wave spectrum in terms of normalized fetch $\hat{x}$ for the practical applications.

(2) That part of the turbulence field close to the interface and with frequencies in the range of the wave frequency is strongly coupled with the wave motion. Strong coherence and stable phase relationships between $\tilde{p}$, $\tilde{u}$ and $\tilde{v}$ with respect to the wave field η are found. The phase angle of $\tilde{p}$ leading the wave by 225° is identical to that found in Elliott's (1972) field data. This phase relationship between wave and wave-induced pressure may provide useful information for theoretical or numerical modeling of the momentum and energy transfer from wind to waves and, hence, for prediction of the growth rate of the wave. In a frequency range greater than 10 Hz, the effects of waves on the turbulent structure were not detected at all. The

inertial subrange of the turbulent energy spectrum satisfied the Kolmogorov $f^{-5/3}$ Law, which is consistent with the physical assumptions of the dynamic behavior of a turbulence spectrum in the equilibrium range. In the high frequency range $(f > 500 \text{ Hz})$ the f^{-7}-law characterizing the usual viscous range of a turbulence spectrum was not achieved in these experiments.

(3) The wave-induced pressure appears to play a dominant role in energy transfer from wind to waves. The wave-induced turbulent Reynolds stresses $\widetilde{u'v'}$ and $\widetilde{v'v'}$, as well as the mean turbulent Reynolds stress $\overline{u'v'}$ have small effects on the energy transfer. The surprising negative mean transfer due to the wave-induced turbulent Reynolds stresses may be attributed to the inability of our measurement system to resolve the very small wave-induced Reynolds stress effects. Since the wave-induced Reynolds stresses are associated with non-linear effects and the present set data was taken at a fixed distance of 0.508 cm above the highest wave, experimental data obtained in the immediate proximity of the interface by employing a wave following device may shed some additional light on these processes.

(4) The nonlinear wave-wave interaction mechanism proposed by Hasselmann (1962) does indeed provide the needed transfer process from the intermediate frequency region into both the relatively lower and higher frequency regions. The transfer from the intermediate frequency to the lower frequency region provides a logical explanation for the establishment of a wind-wave spectrum, namely, the energy is shifted toward the lower frequency region during generation. On the other hand, the transfer from the intermediate frequency to higher frequency

region provides an added source of energy to balance the wave dissipation process. The results indicating a large positive transfer in the high frequency region due to nonlinear wave-wave interaction may be attributed to the inadequacy of Barnett's parametric presentation of the nonlinear process in that frequency range. However, Barnett's parametric equations (2.17) are generally correct and applicable for nondimensional fetch $\hat{x}$ greater than 100. Therefore, they are useful, then, for practical wave prediction.

It seems to be reasonable to conclude that wind wave generation and growth follow this process: Soon after a spectrum develops, the wave-wave interaction mechanism takes over to transfer energy from intermediate frequencies to lower and higher frequencies with the atmosphere acting as a continuous source of energy at the intermediate frequencies.

Positive energy transfer in the low frequency region is responsible for the evolution of the wave spectrum during the period of wave growth and positive transfer in the high frequency region is balanced by the white-capping dissipation.

(5) Hasselmann's (1974) model for white-capping dissipation seems to be valid for $\hat{x} > 100$. However, this validity is associated with the simultaneous application of Barnett's parametric equation representing the nonlinear wave-wave interaction. An independent validation of either the $S_{nl}(f)$ or $S_{ds}(f)$ must await further experimental studies in which $S_{nl}(f)$ and $S_{ds}(f)$ can be measured separately.

(6) The mean momentum transfer, in the direction of wave

propagation, from wind to waves in a developing turbulent boundary layer is governed by the normal pressure and the wave-induced turbulent Reynolds stresses acting along the wave surface. The former contributes about 73% of the total mean momentum transferred into waves, whereas the latter contributes about 27%. Accordingly, turbulence-wave interaction plays an important, but not dominant, role in the momentum transfer from wind to waves. About 70% of the total mean momentum transferred goes from the wind to the wave field directly (in the normalized fetch range: $100 < \hat{x} < 500$), while the remaining 30% goes to the current field.

6.2 Recommendations

(1) The measurement simultaneously of wave height and the fluctuating pressure and velocity components in a fixed or in a wave following system over the surface of a mechanically-generated water wave is a logical extension from the present experimental program. This would produce a greater influence by organized wave-induced components and hence better estimates of the energy and momentum transfer from wind to waves associated with wave-induced or wave-associated components. With these results, we might be to formulate a quantitatively correct model for the momentum and energy transfer from wind to waves. In addition, based on the experimental data on the energy transfer from wind to waves, nonlinear effects seem to be important. Consequently, experimental data in the close proximity of the interface which could be obtained with a wave following system without damaging the hot-wire would be extremely valuable.

-82-

(2) Barnett's parametric equation and Hasselmann's white-capping dissipation model might need to be modified in the relatively high frequency region in order to match the experimental results and balance the energy transfer in this region. For the complete verification of these two models and the full understanding of energy transfer of wind-generated gravity-wave spectrum, an equivalent experimental program to the present one should be carried out in the field.

REFERENCES

Barnett, T. P. (1966), "On the generation, dissipation, and prediction of ocean wind waves," Ph.D. dissertation, Univ. of California, San Diego, Calif.

Barnett, T. P. and J. C. Wilkerson (1967), "On the generation of ocean wind waves as inferred from airborne radar measurements of fetch-limited spectra," J. Mar. Res., 25(3), pp. 292-321.

Barnett, T. P. (1968), "On the generation, dissipation, and prediction of windwaves," J. Geophys. Res., 73(2), pp. 513-529.

Barnett, T. P. (1971), "An international attempt to understand wind generated ocean waves," Part 2: some results. Res. Lab., Westinghouse Elec. Corp., Pittsburgh, Penn., 15 June.

Bendat, J. S. and A. G. Piersol (1971), Random Data: Analysis and Measurement Procedures, Wiley-Interscience, New York.

Blackman, R. B. and J. W. Tukey (1958), The Measurement of Power Spectra, Dover Publication, Inc., New York.

Bole, J. B. and E. Y. Hsu (1969), "Response of gravity water waves to wind excitation," J. Fluid Mech., 35, pp. 657-675.

Bracewell, R. (1965), The Fourier Transform and Its Applications, McGraw-Hill, Inc., New York.

Chambers, A. J., P. A. Mangarella, R. L. Street and E. Y. Hsu (1970), "An experimental investigation of transfer of momentum at an air-water interface," Dept. of Civil Engr. Tech. Rept. No. 133, Stanford Univ., Stanford, Calif.

Chang, P. C., E. J. Plate and G. M. Hidy (1971), "Turbulent air flow over the dominant component of wind-generated water waves," J. Fluid Mech., 47(1), pp. 183-208.

Chao, S. P., E. Y. Hsu and R. L. Street (1976), "The interaction between turbulent wind and progressive water waves," Tech. Rept. No. 204, Dept. of Civil Engr., Stanford Univ., Stanford, Calif.

Colonell, J. M. (1966), "Laboratory simulation of sea waves," Dept. of Civil Engr. Tech. Rept. No. 65, Stanford Univ., Stanford, Calif.

Davis, R. E. (1970), "On the turbulent flow over a wavy boundary," J. Fluid Mech., 42(5), pp. 721-731.

Davis, R. E. (1972), "On prediction of the turbulent flow over a wavy boundary," J. Fluid Mech., 52(2), pp. 287-306.

Dobson, F. W. (1969), "Observation of normal pressure on wind-generated sea waves," Ph.D. dissertation, Univ. of British Columbia, Canada.

Dobson, F. W. (1971), "Measurements of atmospheric pressure on wind-generated sea waves," J. Fluid Mech., 48, pp. 91-127.

Elliott, J. (1972), "Microscale pressure fluctuations near waves being generated by the wind," J. Fluid Mech., 54, pp. 427-448.

Eckart, C. (1953), "The generation of wind waves over a water surface," J. Appl. Phys., 24, pp. 1485-1494.

Gelci, R., J. Cazale and R. Vassal (1956), "Utilisation des diagrammes de propagation à la provision énergétique de le houle," Bull. Inform. Comité Central Oceanog. d'Étude Côtes, 8(4), 169.

Groves, G. W. and J. Melcer (1961), "On the propagation of ocean waves on a sphere," Geofis. Intern., 4(1), pp. 77.

Hasselmann, K. (1960), "Fundamental equations of ocean wave prediction," Shiffstechnik, 7, pp. 191-195.

Hasselmann, K. (1962), "On the non-linear energy transfer in a gravity wave spectrum," Part 1. J. Fluid Mech., 12, pp. 481-500.

Hasselmann, K. (1963), "On the non-linear energy transfer in a gravity wave spectrum," Part 2. J. Fluid Mech., 15, pp. 273-281.

Hasselmann, K. (1963), "On the non-linear energy transfer in a gravity wave spectrum," Part 3. J. Fluid Mech., 15, pp. 385-398.

Hasselmann, K. (1967), "Non-linear interactions treated by the methods of theoretical physics (with application to the generation of wave by wind), " Proc. Roy. Soc., A 299, pp. 77-100.

Hasselmann, K. and J. I. Collins (1968), "Spectral dissipation of finite depth gravity waves due to turbulent bottom friction," J. Mar. Res., 26, pp. 1-12.

Hasselmann, K. (1968), "Weak interaction theory of ocean waves," Basic Developments in Fluid Dynamics, Vol. 2, Ed. by M. Holt. Academic Press, New York.

Hasselmann, K. (1971), "On the mass and momentum transfer between short gravity waves and large-scale motions," J. Fluid Mech., 50(1), pp. 189-206.

Hasselmann, K., T. P. Barnett, E. Bouws, H. Carlson, D. E. Cartwright, K. Enke, J. A. Ewing, H. Gienapp, D. E. Hasselmann, P. Kruseman, A. Meerburg, P. Müller, D. J. Olbers, K. Richter, W. Sell, H. Walden (1973), "Measurements of wind-wave growth and swell decay during the Joint North Sea Wave Project," Deutsches Hydrographisches Institut, Hamburg.

Hasselmann, K. (1974), "On the spectral dissipation of ocean waves due to white capping," Boundary Layer Meteorol., 6, pp. 107-127.

Helmholtz, H. (1868), "Über discontinuierliche Flüssigkeitsbewegungen," Mber. Preuss. Akad. Wiss., pp. 215-228.

Hinze, J. O. (1975), Turbulence -- An Introduction to Its Mechanism and Theory, McGraw-Hill, New York.

Hsu, E. Y. (1965), "A wind, water-wave research facility," Dept. of Civil Engr. Tech. Rept. No. 57, Stanford Univ., Stanford, Calif.

Hussain, A. K. M. F. and W. C. Reynolds (1970), "The mechanics of a perturbation wave in a turbulent shear flow," Dept. of Mech. Engr. Tech. Rept. FM-6, Stanford Univ., Stanford, Calif.

Jeffreys, Sir H. (1925), "On the formation of water waves by wind," Proc. Roy. Soc., A 110, pp. 341-347.

Kline, S. J. and F. A. McClintock (1953), "Describing uncertainties in single sample experiments," Mechanical Engineering, January, 1953.

Lock, R. C. (1954), "Hydrodynamic stability of the flow in the laminar boundary layer between parallel streams," Proc. Camb. Phil. Soc., 50, pp. 105-124.

Longuet-Higgins, M. S. (1969a), "A nonlinear mechanism for the generation of sea waves," Proc. Roy. Soc., A 311, pp. 371-389.

McIntosh, D. A. (1975), "Turbulent heat and momentum transfer at an air-water interface: the influence of surface conditions," Dept. of Civil Engr. Tech. Rept. No. 197, Stanford Univ., Stanford, Calif.

Miles, J. W. (1957), "On the generation of surface waves by shear flows," J. Fluid Mech., 3, pp. 185-204.

Miles, J. W. (1967), "On the generation of surface waves by shear flows," Part 5. J. Fluid Mech., 30, pp. 163-175.

Mitsuyasu, H. (1968b), "A note on the nonlinear energy transfer in the spectrum of wave-generated waves," Rep. Res. Inst. Appl. Mech., 16(54), pp. 251-263, Kyushu Univ., Japan.

Norris, L. H. and W. C. Reynolds (1975), "Turbulent channel flow with a moving wavy boundary," Dept. of Mech. Engr. Tech. Rept. FM-10, Stanford Univ., Stanford, Calif.

Phillips, O. M. (1957), "On the generation of waves by turbulent wind," J. Fluid Mech., 2, pp. 417-445.

Phillips, O. M (1959), "The scattering of gravity waves by turbulence," _J. Fluid Mech._, 5, pp. 177-192.

Phillips, O. M. (1960), "On the dynamics of unsteady gravity waves of finite amplitude," _J. Fluid Mech._, 9, pp. 193-217.

Phillips, O. M. (1966), "_The Dynamics of the Upper Ocean_," Cambridge Univ. Press.

Pierson, W. J. (1959), "A note of the growth of the spectrum of wind-generated gravity waves as determined by non-linear consideration," _J. Geophys. Res._, 64, pp. 1007-1011.

Ramamonjiarisoa, A. and M. Coantic (1976), "Loi expérimentale de dispersion des vagues produites par le vent sur une faible longueru d'action" C. R., Acad. Sc. Paris, t 282 (2 févier).

Shemdin, O. H. and E. Y. Hsu (1967), "The dynamics of wind in the vicinity of progressive water waves," _J. Fluid Mech._, 30, pp. 403-416.

Snyder, R. L. and C. S. Cox (1966), "A field study of the wind generation of ocean waves," _J. Mar. Res._, 24(2), pp. 141-178.

Stewart, R. W. (1961), "The wave drag of wind over water," _J. Fluid Mech._, 10, pp. 189-194.

Sutherland, A. J. (1967), "Spectral measurements and growth rates of wind-generated water waves," Dept. of Civil Engr. Tech. Rept. No. 84, Stanford Univ., Stanford, Calif.

Takeuchi, K. and T. R. Mogel (1975), "A performance evaluation of a mini computer," _Rev. Sci. Instrum._, 46(6), pp. 686-691.

Tchen, C. M. (1953), "On the spectrum of energy in turbulent shear flow," _J. of Res. of the Nat. Bur. of Standards_, 50(1), Res. Paper 2388.

Thomson, Sir W. (1871), "Hydokinetic solutions and observations," _Phil. Mag._, 42(4), pp. 368-372.

Ursell, F. (1956), "Wave generation by wind," _Surveys in Mechanics_ (ed. G. K. Batchelor), pp. 216-249, Cambridge Univ. Press.

Wu, Jin (1968), "Laboratory studies of wind-wave interactions," _J. Fluid Mech._, 34, pp. 91-111.

Wuest, W. (1949), "Beitrag zur entstehung von wasserwellen durch wind," _Z.Angew. Math. Mech._, 29, pp. 239-252.

Young, M. B. O., E. Y. Hsu and R. L. Street (1973), "Air-water inter-
    action: the nature of turbulent heat, mass and momentum transfer
    mechanisms in the air boundary layer," Dept. of Civil Engr. Tech.
    Rept. No. 163, Stanford Univ., Stanford, Calif.

Yu, H. Y., E. Y. Hsu and R. L. Street (1973), "Wave-induced perturba-
    tions in a turbulent boundary layer over progressive water waves,"
    Dept. of Civil Engr. Tech. Rept. No. 172, Stanford Univ., Stanford,
    Calif.

APPENDIX A

UNCERTAINTY ANALYSIS

Uncertainty in measurements always exists due to improper per-
formance, inaccuracy of instruments, and/or propagation of input
uncertainties through the data reduction procedure to the results.
Kline and McClintock (1953) proposed a procedure to determine the
percentage uncertainty in the general dependent quantity of interest
$f(x_i)$ as follows:

$$\frac{\delta f}{f} = \pm \left[\sum_{i=1}^{n} \left(\frac{\partial f}{\partial x_i} \frac{\delta x_i}{f} \right)^2 \right]^{1/2} \tag{A.1}$$

where the x_i are the measured inputs in the data reduction procedure
and δf is the uncertainty in f. The experimental uncertainties
computed here are based on the odds of $20 : 1$.

The basic percentage uncertainties in $\delta x_i/f$ were calculated
from the calibration results and are listed below:

Calibration of crystal pressure transducer	± 5%
Calibration of hot films	± 5%
Calibration of wave-height gauge	± 4%
Mean velocity	± 4%

The uncertainty arising from spectral estimates is computed by
the following relationship [Bendat and Piersol (1971)]:

$$\varepsilon = \frac{1}{\sqrt{N}}$$

where N is the number of spectra averaged and ϵ is the uncertainty of the computed spectra. Fifty spectra were averaged and used for the results presented here so the basic uncertainties of these spectra are $\pm 14.2\%$. The corresponding degrees of freedom [$\simeq 2N$, Bendat and Piersol (1971)] and confidence band [Blackman and Tukey (1958)] are 100 and 90% respectively.

The resulting uncertainties calculated by equation (A.1) are

u_*	$\pm 10\%$
$\hat{\epsilon}$	$\pm 15\%$
α	$\pm 15\%$
$\hat{f}_m$	$\pm 15\%$
$\hat{x}$	$\pm 14\%$
R	$\pm 14\%$
Θ	$\pm 14\%$
$\tilde{p}\,\dfrac{\partial \eta}{\partial x}$	$\pm 14\%$
$\overline{u'u'}\,\dfrac{\partial \eta}{\partial x}$	$\pm 30\%$
$\overline{u'v'}\,\tilde{u}$	$\pm 30\%$
$\overline{v'v'}\,\tilde{v}$	$\pm 30\%$

The uncertainty here does not invalidate the results and conclusions presented in Chapters 5 and 6.

-90-

APPENDIX B

ENERGY TRANSFER EQUATION OF A WIND WAVE SPECTRUM

Hasselmann (1968) posed a generalized formulation of the energy balance equation for a wind wave spectrum; this equation can be expressed as

$$\frac{DF(\vec{k},\vec{x},t)}{Dt} = \frac{\partial F}{\partial t} + \dot{x}_i \frac{\partial F}{\partial x_i} + \dot{k}_i \frac{\partial F}{\partial k_i} = S(\vec{k}) \tag{B.1}$$

where

$$\dot{x}_i = \frac{\partial \omega(\vec{x},\vec{k})}{\partial k_i}, \qquad \dot{k}_i = -\frac{\partial \omega(\vec{x},\vec{k})}{\partial x_i} \tag{B.2}$$

It is assumed that the bottom depth H is slowly varying, i.e., $(1/k)(\partial H / \partial x_i) \ll 1$, so that the geometrical refraction law equation (B.2) is applicable (the dot denotes differentiation with respect to t and $\omega = (gk \tanh kH)^{1/2}$ is the radian frequency of a free surface gravity wave traveling in water of depth H). $S(\vec{k})$ is the net rate of energy transfer and is a function of the wave number vector $\vec{k}$. Also $\int F(\vec{k},\vec{x},t) \, d\vec{k} = \rho_\omega g <\eta^2>$ where ρ_ω is water density, η is the water surface deviation from the mean still water level and the bracket denotes an ensemble average.

In equation (B.1), DF / Dt represents the Lagrangian rate of change of the spectrum relative to a wave group $\vec{k}$ moving along the path in $\vec{x} - \vec{k}$ phase space determined by the Hamiltonian equations (B.2). In deep water, the wave refraction $\dot{k}_i \, \partial F / \partial k_i$ is zero. The source

function $S(\vec{k})$ represents the net rate of energy transfer to or from the spectrum at the wave number $\vec{k}$ due to all the interaction processes which affect the component $\vec{k}$. The general form of the source function is

$$S(\vec{k}) = S_1 + S_2 + S_3 + S_4 + S_1' + S_2' + S_3' + S_4' + S_5 + S_6 + S_7 + \ldots$$

where

S_1 represents the constant energy transfer to the wave field through atmospheric turbulence pressure fluctuations (Eckart, 1953; Phillips, 1957).

S_2 represents the inviscid mechanism of unstable coupling between the wave field and the mean boundary layer flow (Miles, 1957).

S_3 represents the non-linear correction to Miles' inviscid theory.

S_4 represents the energy transfer due to wave-burbulence interaction (Hasselmann, 1967).

$S_1' \sim S_4'$ represent the transfer due to the interactions of waves with mean currents and turbulence in the ocean, corresponding to the transfer processes $S_1 \sim S_4$ of similar interactions with the atmosphere; S_1' and S_2' are normally neglected according to Hasselmann (1968).

S_5 represents the energy transfer due to nonlinear wave-wave interactions (Hasselmann, 1962).

S_6 represents energy dissipation in shallow water due to turbulent bottom friction (Hasselmann and Collins, 1968).

S_7 represents energy loss due to wave breaking (Hasselmann, 1974).

...   other mechanisms for a systematic and complete theory of wind-wave generation.

Equation (B.1) can be simplified for a stationary deep-water wave spectrum with negligible of mean ocean current and can be expressed as

$$\dot{x}\,\frac{\partial F}{\partial x} = S_{in} + S_{nl} + S_{ds} \tag{B.3}$$

where $\dot{x}$ is the group velocity.

Next, we let S_{in} represent the rate of energy transfer from wind to waves, corresponding to the sum of S_1 to S_4, which is dominated by the normal pressure acting on the wave surface as indicated in Appendix D; S_{nl} and S_{ds} are equal to S_5 and S_7, respectively. Equation (B.3) is equivalent to equation (2.5) in Section 2.1.

APPENDIX C

MOMENTUM TRANSFER FROM WIND TO WAVES

IN A DEVELOPING TURBULENT BOUNDARY LAYER

The developing turbulent boundary layer equation describing the momentum transfer across the wind-wave interface was derived by C. T. Hsu (private communication) and is summarized in this section. In the derivation of the governing equation of the air flow, the decomposition of an instantaneous quantity, $f(\vec{x},t)$ for the flow above the wavy boundary is assumed to be

$$f(\vec{x},t) = \overline{f}(\vec{x}) + \tilde{f}(\vec{x},t) + f'(\vec{x},t)$$

where $\overline{f}$ is the time-averaged mean quantity, $\tilde{f}$ is a wave-induced perturbation quantity associated with the wave motion, f' is a background turbulent quantity. In order to determine the wave-induced quantity, the statistical techniques of time average and phase average are employed. The time average of $f(\vec{x},t)$ is

$$\overline{f}(\vec{x}) = \lim \frac{1}{T} \int_{0}^{T} f(\vec{x},t) \, dt$$

whereas a phase average is

$$<f(\vec{x},t)> = \lim_{N \to \infty} \frac{1}{N} \sum_{n=1}^{N} f(\vec{x}, t + n\tau)$$

where τ is the period of a wave and N is the number of waves in the

ensemble. The background turbulence is assumed to be random and its contribution to the phase average of a large ensemble is zero. Then the phase average of f is

$$<f> = \bar{f} + \tilde{f}$$

and the wave-induced quantity is

$$\tilde{f} = <f> - \bar{f}$$

Some useful relations that follow from the above definitions are

$$\overline{f'} = 0 \qquad \overline{\tilde{f}} = 0 \qquad <f'> = 0$$

$$<\bar{f}> = \bar{f} \qquad \overline{<f>} = \bar{f} \qquad <\tilde{f}> = \tilde{f}$$

$$\overline{\bar{f}\,g} = \bar{f}\,\bar{g} \qquad <\bar{f}\,g> = \bar{f}<g> \qquad <\tilde{f}\,g> = \tilde{f}<g>$$

$$\overline{\tilde{f}\,g'} = 0 \qquad \overline{<\tilde{f}\,g'>} = 0 \qquad <\tilde{f}\,g'> = 0$$

where f and g are two arbitrary quantities.

C.1 Momentum Transfer in Horizontal X-Direction

The air flow above the wave surface η is assumed to be a two-dimensional turbulent shear flow. The momentum equation in x-direction and continuity equation can be written as

-95-

$$\frac{\partial u}{\partial t} + u \frac{\partial u}{\partial x} + v \frac{\partial u}{\partial y} = - \frac{1}{\rho_a} \frac{\partial p}{\partial x} + \nu \left(\frac{\partial^2 u}{\partial x^2} + \frac{\partial^2 u}{\partial y^2} \right) \tag{C.1}$$

and

$$\frac{\partial u}{\partial x} + \frac{\partial v}{\partial y} = 0 \tag{C.2}$$

Applying (C.2), we can rewrite (C.1) as

$$\frac{\partial u}{\partial t} + \frac{\partial u^2}{\partial x} + \frac{\partial (uv)}{\partial y} = - \frac{1}{\rho_a} \frac{\partial p}{\partial x} + \nu \nabla^2 u \tag{C.3}$$

As previously discussed we can decompose the velocity components and pressure into mean, wave-induced and background turbulent quantities as follows:

$$u = \overline{u} + \tilde{u} + u'$$

$$v = \overline{v} + \tilde{v} + v' \tag{C.4}$$

$$p = \overline{p} + \tilde{p} + p'$$

Substituting (C.4) into equation (C.1), and taking the phase average of the result yields

$$\frac{\partial}{\partial t} (\overline{u} + \tilde{u}) + \frac{\partial}{\partial x} [(\overline{u} + \tilde{u})^2 + <u'^2>] + \frac{\partial}{\partial y} [(\overline{u} + \tilde{u})(\overline{v} + \tilde{v}) + <u'v'>]$$

$$= - \frac{1}{\rho_a} \frac{\partial}{\partial x} (\overline{p} + \tilde{p}) + \nu \nabla^2 (\overline{u} + \tilde{u}) \tag{C.5}$$

where $<u'^2> = \overline{u'^2} + \widetilde{u'^2}$ and $<u'v'> = \overline{u'v'} + \widetilde{u'v'}$. The terms

-96-

associated with the background turbulence disappear in the phase
average except for the quadratic terms u'^2 and $u'v'$. For the
convenience of the following derivation, the pressure and velocity com-
ponents are redefined now so

$$u = \bar{u} + \tilde{u} \qquad v = \bar{v} + \tilde{v} \qquad p = \bar{p}_\infty + \bar{p} + \tilde{p}$$

where $\bar{p}_\infty$ is the pressure at free stream. By applying the new defi-
nition of u, v and p, we can rewrite (C.5) as

$$\frac{\partial u}{\partial t} + \frac{\partial}{\partial x} (u^2 + \langle u'^2 \rangle) + \frac{\partial}{\partial y} (uv + \langle u'v' \rangle)$$

$$= -\frac{1}{\rho_a} \frac{\partial}{\partial x} (p - \bar{p}_\infty) + \nu \nabla^2 u \qquad\qquad (C.6)$$

The momentum equation at free stream is

$$\frac{\partial u_\infty}{\partial t} + u_\infty \frac{\partial u_\infty}{\partial x} = -\frac{1}{\rho_a} \frac{\partial \bar{p}_\infty}{\partial x} \qquad\qquad (C.7)$$

where u_∞ and $\bar{p}_\infty$ are the free stream velocity and pressure.
Subtracting equation (C.6) from equation (C.7) and applies the still
valid continuity equation for incompressible flow

$$\frac{\partial u}{\partial x} + \frac{\partial v}{\partial y} = 0$$

we obtain

$$\frac{\partial}{\partial t} (u_\infty - u) + \frac{\partial}{\partial x} (u_\infty u - u^2) + (u_\infty - u) \frac{\partial u_\infty}{\partial x} + \frac{\partial}{\partial y} [v(u_\infty - u)]$$

$$- \frac{1}{\rho_a} \frac{\partial}{\partial x} (\tilde{p} + \overline{p}) + \nu \nabla^2 u - \frac{\partial}{\partial x} <u'^2> - \frac{\partial}{\partial y} <u'v'> = 0 \qquad (c.8)$$

Now, define the displacement thickness δ_1 and momentum thickness δ_2 as

$$\delta_1 = \int_\eta^\infty (1 - \frac{u}{u_\infty}) \, dy \quad ; \quad \delta_2 = \int_\eta^\infty \frac{u}{u_\infty} (1 - \frac{u}{u_\infty}) \, dy$$

The integrating equation (C.8) with respect to y from η to ∞ and applying the identity

$$\int_\eta^\infty \frac{\partial f}{\partial x_1} \, dy = \frac{\partial}{\partial x_1} [\int_\eta^\infty f \, dy] + [f \frac{\partial \eta}{\partial x_1}]_{y=\eta}$$

where the variable x_1 represents either x or t allows equation (C.8) to be expressed as

$$\frac{\partial}{\partial t} (u_\infty \delta_1) + \frac{\partial}{\partial x} (u_\infty^2 \delta_2) + u_\infty \frac{\partial u_\infty}{\partial x} \delta_1 + \frac{\partial}{\partial x} [\int_\eta^\infty \nu \frac{\partial u}{\partial x} \, dy]$$

$$- \frac{1}{\rho_a} \frac{\partial}{\partial x} [\int_\eta^\infty \tilde{p} \, dy] - \frac{\partial}{\partial x} [\int_\eta^\infty <u'^2> \, dy]$$

$$= [\nu \frac{\partial u}{\partial y} - <u'v'> + \frac{1}{\rho} \tilde{p} \frac{\partial \eta}{\partial x} - \nu \frac{\partial \tilde{u}}{\partial x} \frac{\partial \eta}{\partial x} + <u'^2> \frac{\partial \eta}{\partial x}]_{y=\eta} \qquad (C.9)$$

In arriving at equation (C.9), the boundary condition at the interface, i.e., $v = \frac{\partial \eta}{\partial t} + u \frac{\partial \eta}{\partial x}$ is applied.

The left hand side of equation (C.9) represents the total rate of horizontal momentum transfer across the interface from the air field. The right hand side of equation (C.9) represents the mechanism of interface transfer. Since we are not interested in the instantaneous time varying field, the time-average of equation (C.9) was taken and the resultant mean momentum transferred across the wind-wave interface is

$$M = [\mu \frac{\partial \overline{u}}{\partial y} - \rho_a \overline{u'v'} + \overline{\tilde{p} \frac{\partial \eta}{\partial x}} - \mu \overline{\frac{\partial \tilde{u}}{\partial x} \frac{\partial \eta}{\partial x}} + \rho_a \overline{u'^2 \frac{\partial \eta}{\partial x}}]_{y=\eta} \qquad (C.10)$$

In equation (C.10), the terms associated with the wave form η and the wave-induced quantities should be account for the mean momentum transferred into wave field directly, i.e.,

$$M_w = [\overline{\tilde{p} \frac{\partial u}{\partial y}} - \mu \overline{\frac{\partial \tilde{u}}{\partial x} \frac{\partial \eta}{\partial x}} + \rho_a \overline{u'^2 \frac{\partial \eta}{\partial x}}]_{y=\eta}$$

The remaining terms should be attributed to the mean momentum transferred into current as expressed by

$$M_c = [\mu \frac{\partial \overline{u}}{\partial y} - \rho \overline{u'v'}]_{y=\eta}$$

If the location of measurement $(\eta + \delta_*)$ is outside the viscous sublayer of the air flowfield, then the viscous effect can be neglected, and

$$M = [- \rho \, \overline{u'v'} + \overline{\tilde{p} \frac{\partial \eta}{\partial x}} + \rho_a \overline{\tilde{u'}^2 \frac{\partial \eta}{\partial x}}]_{y=\eta+\delta_*} \qquad (C.11)$$

$$M_w = [\overline{\tilde{p} \frac{\partial \eta}{\partial x}} + \rho_a \overline{\tilde{u'}^2 \frac{\partial \eta}{\partial x}}]_{y=\eta+\delta_*} \qquad (C.12)$$

$$M_c = [- \rho \, \overline{u'v'}]_{y=\eta+\delta_*} \qquad (C.13)$$

Accordingly, the ratio of the mean horizontal momentum transferred into waves over the total mean horizontal momentum transferred across the wind-wave interface is given by

$$\gamma = M_w \, / \, M \qquad (C.14)$$

This expression seems to be applicable for a general air flow (developing and fully-developed turbulent boundary layers) and imposes no limitation on the wave forms (small or finite amplitude). The results for M_w, M_c and γ are tabulated in Table (C.1) for various wind and wave conditions. Discussion is provided in Section 5.7.

C.2 Momentum Transfer in Vertical Y-Direction

Similarly, the phase average of the momentum equation in the y-direction is

$$\frac{\partial v}{\partial t} + u \frac{\partial v}{\partial x} + v \frac{\partial v}{\partial y} + \frac{\partial}{\partial x} <u'v'> + \frac{\partial}{\partial y} <v'v'>$$

$$= - \frac{1}{\rho_a} \frac{\partial}{\partial y} (p - \overline{p}_\infty) + \nu (\frac{\partial^2 v}{\partial x^2} + \frac{\partial^2 v}{\partial y^2}) \qquad (C.15)$$

where $u = \bar{u} + \tilde{u}$, $v = \bar{v} + \tilde{v}$ and $p = \bar{p}_\infty + \bar{p} + \tilde{p}$

Integrating (C.10) with respect to y from η to ∞ produces

$$\frac{\partial}{\partial t} [\int_\eta^\infty v \, dy] + \frac{\partial}{\partial x} [\int_\eta^\infty (uv + \langle u'v' \rangle - \nu \frac{\partial v}{\partial x}) dy] + v_\infty^2 + \frac{1}{\rho_a} \bar{p}_\infty$$

$$= [\frac{1}{\rho_a} p + \langle v'v' \rangle - \nu \frac{\partial v}{\partial y} + \nu \frac{\partial v}{\partial x} \frac{\partial \eta}{\partial x} - \langle u'v' \rangle \frac{\partial \eta}{\partial x}]_{y=\eta} \qquad (C.16)$$

On the left hand side of equation (C.16), the first term represents the momentum transfer in the control volume bounded by $x = x_\gamma$, $x = x_\gamma + \Delta x$, $y = \eta$ and $y = \infty$; the second term represents the net force acting on each edge of $x = x_\gamma$ and $x = x_\gamma + \Delta x$; and the third and fourth terms represent the force acting on the edge of $y = \infty$. The terms on the right hand side of equation (C.16) represent the total force supported by the water field. The time-average of equation (C.16) is

$$\frac{\partial}{\partial t} [\overline{\int_\eta^\infty (uv + \langle u'v' \rangle - \nu \frac{\partial v}{\partial x}) \, dy}] + v_\infty^2 + \frac{1}{\rho_a} \bar{p}_\infty$$

$$= [\frac{1}{\rho_a} \bar{p} + \overline{v'v'} - \nu \frac{\partial \bar{v}}{\partial y} - \overline{\langle u'v' \rangle \frac{\partial \eta}{\partial x}}]_{y=\eta} \qquad (C.17)$$

The last term on the right hand side of above equation is the only term transferring vertical momentum to the wave. Therefore, the vertical mean momentum transfer from wind to waves is

$$M_{yw} = \overline{[- \rho_a \langle u'v' \rangle \frac{\partial \eta}{\partial x}]}_{y=\eta+\delta_*} = \overline{[- \rho_a \widehat{u'v'} \frac{\partial \eta}{\partial x}]}_{y=\eta+\delta_*} \qquad (C.18)$$

-101-

This vertical momentum transferred from wind to waves will act together with the horizontal momentum transferred from wind to waves and form the circular motion of the wave.

APPENDIX D

ENERGY TRANSFER FROM WIND TO WAVES

IN A DEVELOPING TURBULENT BOUNDARY LAYER

D.1 Energy Transfer in Horizontal X-Direction

The energy transfer across the wind-wave interface can be derived by multiplying equation (C.8) by $2u$ and is expressed as

$$\frac{\partial}{\partial t} (u_\infty u - u^2) + u_\infty^2 \frac{\partial}{\partial t} (1 - \frac{u}{u_\infty}) + \frac{\partial}{\partial x} (u_\infty^2 u - u^3) + \frac{\partial}{\partial y} [(u_\infty^2 - u^2) v]$$

$$- 2 u \frac{\partial}{\partial x} \langle u'u' \rangle - 2 u \frac{\partial}{\partial y} \langle u'v' \rangle - \frac{2u}{\rho_a} \frac{\partial}{\partial x} (\tilde{p} + \overline{p}) - 2 \nu (\frac{\partial u}{\partial y})^2$$

$$+ 2 \nu \frac{\partial}{\partial y} (u \frac{\partial u}{\partial y}) - 2 \nu (\frac{\partial u}{\partial x})^2 + 2 \nu \frac{\partial}{\partial x} (u \frac{\partial u}{\partial x}) = 0 \qquad (D.1)$$

where $u = \overline{u} + \tilde{u}$, $v = \overline{v} + \tilde{v}$ and $p = \overline{p}_\infty + \overline{p} + \tilde{p}$.

We define D_x, δ_1, δ_2 and δ_3 as

$$D_x = \int_\eta^\infty \mu [(\frac{\partial u}{\partial x})^2 + (\frac{\partial u}{\partial y})^2] \, dy$$

$$\delta_1 = \int_\eta^\infty (1 - \frac{u}{u_\infty}) \, dy$$

$$\delta_2 = \int_\eta^\infty \frac{u}{u_\infty} (1 - \frac{u}{u_\infty}) \, dy$$

$$\delta_3 = \int_\eta^\infty \frac{u}{u_\infty} (1 - \frac{u^2}{u_\infty^2}) \, dy$$

Employing the boundary condition $v = \partial \eta / \partial t + u \partial \eta / \partial x$, and integrating

equation (D.1) with respect to y from η to ∞ yields

$$\frac{\partial}{\partial t}(u_\infty^2 \delta_2) + u_\infty^2 \frac{\partial}{\partial t}\delta_1 + \frac{\partial}{\partial x}(u_\infty^3 \delta_3) - 2\frac{\partial}{\partial x}\int_\eta^\infty u<u'u'>\,dy$$

$$- 2[u<u'u'>\frac{\partial \eta}{\partial x}]_{y=\eta} + 2\int_\eta^\infty <u'u'>\frac{\partial \eta}{\partial x}\,dy + 2[u<u'v'>]_{y=\eta}$$

$$+ 2\int_\eta^\infty <u'v'>\frac{\partial u}{\partial y}\,dy - \frac{2}{\rho_a}\frac{\partial}{\partial x}\int_\eta^\infty (\tilde{p} + \overline{p})\,u\,dy - \frac{2}{\rho_a}[(\tilde{p} + \overline{p})\,u\,\frac{\partial \eta}{\partial x}]_{y=\eta}$$

$$+ \frac{2}{\rho_a}\int_\eta^\infty (\tilde{p} + \overline{p})\frac{\partial u}{\partial x}\,dy - \frac{2\,D_x}{\rho_a} - 2\nu[u\frac{\partial u}{\partial y}]_{y=\eta} + 2\frac{\partial}{\partial x}[\int_\eta^\infty \nu\,u\,\frac{\partial u}{\partial x}\,dy]$$

$$+ 2\nu[u\frac{\partial u}{\partial x}\frac{\partial \eta}{\partial x}]_{y=\eta} = 0 \tag{D.2}$$

Dividing equation (D.2) by a factor of 2 and rearranging it yields

$$[\nu\frac{\partial u}{\partial y}u + \frac{1}{\rho_a}\tilde{p}\frac{\partial \eta}{\partial x}u + <u'u'>\frac{\partial \eta}{\partial x}u - \nu\frac{\partial u}{\partial x}\frac{\partial \eta}{\partial x}u - <u'v'>u]_{y=\eta}$$

$$+ \frac{D_x}{\rho_a} - \int_\eta^\infty [<u'u'>\frac{\partial u}{\partial x} + <u'v'>\frac{\partial u}{\partial y}]\,dy - \frac{1}{\rho_a}\int_\eta^\infty (\overline{p} + \tilde{p})\frac{\partial u}{\partial x}\,dy$$

$$= \frac{1}{2}\frac{\partial}{\partial t}(u_\infty^2 \delta_2) + \frac{1}{2}u_\infty^2 \frac{\partial}{\partial t}\delta_1 + \frac{1}{2}\frac{\partial}{\partial x}(u_\infty^2 \delta_3)$$

$$+ \frac{\partial}{\partial x}[\int_\eta^\infty (\nu\frac{\partial u}{\partial x} - <u'u'> - \frac{\overline{p} + \tilde{p}}{\rho_a})\,u\,dy] \tag{D.3}$$

On the left hand side of equation (D.3), the first five terms evaluated at $y = \eta$ indicate the energy transfer from wind to water due to horizontal force; the sixth term denotes the large scale dissipation in the wind field and is considered negligible; the seventh term denotes the energy sink to the turbulent field due to the strain

-104-

against the turbulent stresses; and the eighth term represents the work done by the pressure force $\tilde{p}$ associated with volumetric change in x-direction. The net horizontal mean energy transfer across the wind wave interface can be derived by taking the time-average of equation (D.3), yielding

$$E_x = \nu \; \overline{[\frac{\partial u}{\partial y} u]}_{y=\eta} + \frac{1}{\rho_a} \; \overline{[\tilde{p} \frac{\partial \eta}{\partial x} u]}_{y=\eta} + \overline{[<u'u'> \frac{\partial \eta}{\partial x} u]}_{y=\eta}$$

$$- \nu \; \overline{[\frac{\partial u}{\partial x} \frac{\partial \eta}{\partial x} u]}_{y=\eta} - \overline{[<u'v'> u]}_{y=\eta} \qquad (D.4)$$

Applying $u = \bar{u} + \tilde{u}$ [c.f., equation (C.6)] in the above equation, we obtain

$$E_x = \nu \; \overline{[\frac{\partial \bar{u}}{\partial y} \bar{u}]}_{y=\eta} + \nu \; \overline{[\frac{\partial \tilde{u}}{\partial y} \tilde{u}]}_{y=\eta} + \frac{1}{\rho_a} \; \overline{[\tilde{p} \frac{\partial \eta}{\partial x}]}_{y=\eta} \bar{u}_{y=\eta}$$

$$+ \frac{1}{\rho_a} \; \overline{[\tilde{p} \frac{\partial \eta}{\partial x} \tilde{u}]}_{y=\eta} + \overline{[<u'u'> \frac{\partial \eta}{\partial x} \bar{u}]}_{y=\eta} + \overline{[<u'u'> \frac{\partial \eta}{\partial x} \tilde{u}]}_{y=\eta}$$

$$- \nu \; \overline{[\frac{\partial \bar{u}}{\partial x} \frac{\partial \eta}{\partial x} \tilde{u}]}_{y=\eta} - \nu \; \overline{[\frac{\partial \tilde{u}}{\partial x} \frac{\partial \eta}{\partial x} \bar{u}]}_{y=\eta} - \nu \; \overline{[\frac{\partial \tilde{u}}{\partial x} \frac{\partial \eta}{\partial x} \tilde{u}]}_{y=\eta}$$

$$- \overline{[<u'v'> \tilde{u}]}_{y=\eta} - \overline{[u'v' \; \bar{u}]}_{y=\eta} \qquad (D.5)$$

From equation (D.5) the terms associated with the mean velocity at the interface should account for the energy transfer from wind to current. At the interface, the mean velocity can be represented by the velocity of the drift current. The remaining energy should be transferred into the wave field. The energy transferred into wave and current fields

are expressed, respectively, as

$$E_{xw} = \rho_a \, [\nu \, \overline{\frac{\partial \tilde{u}}{\partial y} \tilde{u}} + \frac{1}{\rho_a} \, \overline{\tilde{p} \, \frac{\partial \eta}{\partial x} \, \tilde{u}} + \overline{<u'u'> \frac{\partial \eta}{\partial x} \, \tilde{u}}$$

$$- \nu \, \overline{\frac{\partial \overline{u}}{\partial x} \frac{\partial \eta}{\partial x} \, \tilde{u}} - \nu \, \overline{\frac{\partial \tilde{u}}{\partial x} \frac{\partial \eta}{\partial x} \, \tilde{u}} - \overline{<u'v'> \, \tilde{u}}]_{y=\eta} \qquad (D.6)$$

$$E_{xc} = \rho_a \, [(\nu \, \frac{\partial \overline{u}}{\partial y} + \frac{1}{\rho_a} \, \overline{\tilde{p}} \, \frac{\partial \eta}{\partial x} + \overline{<u'u'>} \, \frac{\partial \eta}{\partial x}$$

$$- \nu \, \overline{\frac{\partial \tilde{u}}{\partial x} \frac{\partial \eta}{\partial x}} - \overline{u'v'}) \, \overline{u}]_{y=\eta} \qquad (D.7)$$

D.2 Energy Transfer in Vertical Y-Direction

Similarly, the energy transfer equation in the y-direction can be derived by multiplying the momentum equation (C.15) by $2v$ and integrating it with respect to y from η to ∞, viz.,

$$(\nu \, \frac{\partial v}{\partial y} \, v)_{y=\eta} - \frac{1}{\rho_a} \, [(\tilde{p} + \overline{p}) \, v]_{y=\eta} - [<v'v'> v]_{y=\eta} - \nu[\frac{\partial v}{\partial x} \frac{\partial \eta}{\partial x} v]_{y=\eta}$$

$$+ [<u'v'> \frac{\partial \eta}{\partial x} v]_{y=\eta} + \frac{D_y}{\rho_a} - \int_\eta^\infty [<u'v'> \frac{\partial v}{\partial x} + <v'v'> \frac{\partial v}{\partial y}] \, dy$$

$$- \frac{1}{\rho_a} \int_\eta^\infty (\overline{p} + \tilde{p}) \, \frac{\partial v}{\partial y} \, dy = - \frac{1}{2} \frac{\partial}{\partial t} \, [\int_\eta^\infty v^2 \, dy] - \frac{1}{2} \frac{\partial}{\partial x} \, [\int_\eta^\infty u \, v^2 \, dy]$$

$$- \frac{1}{2} \, v_\infty^3 - \frac{\partial}{\partial x} \, [\int_\eta^\infty (<u'v'> - \nu \, \frac{\partial v}{\partial x}) \, v \, dy] \qquad (D.8)$$

where $u = \overline{u} + \tilde{u}$, $v = \overline{v} + \tilde{v}$, $p = \overline{p}_\infty + \overline{p} + \tilde{p}$ and $D_y = \mu \int_\eta^\infty [(\frac{\partial v}{\partial x})^2 + (\frac{\partial v}{\partial y})^2] \, dy$

-106-

Then, the vertical mean energy transfer across the wind-wave interface can be derived by taking the time-average of equation (D.8), yielding

$$
E_y = [\mu \, \overline{\frac{\partial v}{\partial y} v} - \overline{(\bar{p} + \tilde{p}) v} - \rho_a \overline{<v'v'> v} - \mu \, \overline{\frac{\partial v}{\partial x} \frac{\partial \eta}{\partial x} v} + \rho_a \overline{<u'v'> \frac{\partial \eta}{\partial x} v}]_{y=\eta}
$$

(D.9)

Substituting $v_\eta = \bar{v}_\eta + \tilde{v}_\eta = \tilde{v}_\eta$, we get

$$
E_y = [\mu \, \overline{\frac{\partial \tilde{v}}{\partial y} \tilde{v}} - \overline{\tilde{p} \, \tilde{v}} - \rho_a \overline{<v'v'> \tilde{v}} - \mu \, \overline{\frac{\partial \tilde{v}}{\partial x} \frac{\partial \eta}{\partial x} \tilde{v}} + \rho_a \overline{<u'v'> \frac{\partial \eta}{\partial x} \tilde{v}}]_{y=\eta}
$$

$$
= E_{yw}
$$

(D.10)

Viewing equation (D.10), we find that all the vertical mean energy transfer goes directly to the wave field. Finally, we can sum up the horizontal and vertical mean energy transfer from wind to waves as follows:

$$
E_w = E_{xw} + E_{yw}
$$

$$
= [\mu \, \overline{\frac{\partial \tilde{u}}{\partial y} \tilde{u}} - \rho_a \overline{\widetilde{u'v'} \, \tilde{u}} + \overline{(\tilde{p} + \rho_a \widetilde{u'u'} - \mu \frac{\partial \tilde{u}}{\partial x}) \frac{\partial \eta}{\partial x} \tilde{u}}]_{y=\eta}
$$

$$
+ [\mu \, \overline{\frac{\partial \tilde{v}}{\partial y} \tilde{v}} - \overline{\tilde{p} \, \tilde{v}} - \rho_a \overline{\widetilde{v'v'} \, \tilde{v}} + \rho_a \overline{u'v' \frac{\partial \eta}{\partial x} \tilde{v}}
$$

$$
+ \overline{\widetilde{u'v'} \frac{\partial \eta}{\partial x} \tilde{v}} - \mu \, \overline{\frac{\partial \tilde{v}}{\partial x} \frac{\partial \eta}{\partial x} \tilde{v}}]_{y=\eta}
$$

(D.11)

After neglecting the viscous effect and only considering the lower

order terms, we can rewrite the total mean energy transfer to waves as

$$E_w = [- \rho_a \overline{\widehat{u'v'} \, \tilde{u}} - \overline{\tilde{p} \, \tilde{v}} - \rho_a \overline{\widehat{v'v'} \, \tilde{v}} + \rho_a \overline{u'v' \, \frac{\partial \eta}{\partial x} \tilde{v}}]_{y=\eta} \quad (D.12)$$

while the total mean energy transfer across the wind-wave interface is

$$E = E_{xw} + E_{yw} + E_{xc} + E_{yc}$$

$$= E_w + E_{xc}$$

$$= [- \rho_a \overline{\widehat{u'v'} \, \tilde{u}} - \overline{\tilde{p} \, \tilde{v}} - \rho_a \overline{\widehat{v'v'} \, \tilde{v}} + \rho_a \overline{u'v' \, \frac{\partial \eta}{\partial x} \tilde{v}}]_{y=\eta}$$

$$+ \rho_a [(\nu \frac{\partial \overline{u}}{\partial y} + \frac{1}{\rho_a} \overline{\tilde{p} \, \frac{\partial \eta}{\partial x}} + \overline{<u'u'> \frac{\partial \eta}{\partial x}} - \nu \overline{\frac{\partial u}{\partial x} \frac{\partial \eta}{\partial x}} - \overline{u'v'}) \, \overline{u}]_{y=\eta}$$

$$(D.13)$$

where $E_{yc} = 0$

The ratio of the mean energy transferred into waves over the total mean
energy transferred across wind-wave interface is

$$\gamma_E = E_w / E \quad (D.14)$$

The calculated results for each term in equation (D.12) were shown
in Table (D.1) from our experiments. It was found that the normal
pressure working on wave surface is the dominant mechanism for energy
transfer from wind to waves. The average value of γ_E is about 0.9
which means most of the energy transferred across the wind-wave inter-
face goes to wave field directly.

-108-

APPENDIX E

DATA REDUCTION COMPUTER PROGRAMS

The most important computer programs used in data reduction are subroutines for the cross spectrum and calculation of nonlinear wave-wave interaction by Barnett's parametric equation. Based on these two programs, we can calculate the power spectra, coherence, phase relation, energy transfer from wind to waves, nonlinear wave-wave interactions, and white capping dissipation.

```
0001          CCROSS SPECTRUM SUBROUTINE
0002          CN=512,NUMBER OF DATA POINT FOR EACH SET OF DATA IN FFT
0003          CNN1=2*N-1,M=N/10,K=N/2+1,L=2*N+3,TAPER=COSINE TAPER
0004          CNN1,M,K,L,TAPER=ALL DEFINED IN MAIN PROGRAM
0005          CX(1024)=STORE TWO SETS OF DATA FOR FFT
0006          CXX,YY=AUTO-SPECTRUM OF TWO SETS OF DATA
0007          CRXY,TXY=COSPECTRUM AND QUADRATURE SPECTRUM BETWEEN TWO
0008          CSETS OF DATA
0009          SUBROUTINE CROSS(N,NN1,M,K,L)
0010          DIMENSION X(1024),TAPER(51),XX(257),YY(257),RXY(257),
0011         1TXY(257)
0012          COMMON RXY,TXY,XX,YY,X,TAPER
0013          NN=2*N
0014          SUM1=0.
0015          SUM2=0.
0016          DO 40 I=1,NN1,2
0017          SUM1=SUM1+X(I)
0018       40 SUM2=SUM2+X(I+1)
0019          SUM1=SUM1/FLOAT(N)
0020          SUM2=SUM2/FLOAT(N)
0021          DO 45 I=1,NN1,2
0022          X(I)=X(I)-SUM1
0023       45 X(I+1)=X(I+1)-SUM2
0024          DO 58 I=1,M
0025          II=2*I-1
0026          III=NN-II
0027          X(II)=X(II)*TAPER(I)
0028          X(II+1)=X(II+1)*TAPER(I)
0029          X(III)=X(III)*TAPER(I)
0030       58 X(III+1)=X(III+1)*TAPER(I)
0031          CALL FFT(X)
0032          XX(1)=XX(1)+4.*X(1)**2
0033          YY(1)=YY(1)+4.*X(2)**2
0034          RXY(1)=RXY(1)+2.*X(1)*X(2)
0035          TXY(1)=0.
0036          DO 122 I=2,K
0037          II=2*I-1
0038          III=L-2*I
0039          RX=X(II)+X(III)
0040          TX=X(II+1)-X(III+1)
0041          XX(I)=XX(I)+RX*RX+TX*TX
0042          RY=X(II+1)+X(III+1)
0043          TY=X(III)-X(II)
0044          YY(I)=YY(I)+RY*RY+TY*TY
0045          RXY(I)=RXY(I)+X(II)*X(III+1)+X(III)*X(II+1)
0046      122 TXY(I)=TXY(I)+X(II)**2+X(II+1)**2-X(III)**2
0047         1-X(III+1)**2
0048          RETURN
0049          END
**** LIST END ****
```

```
0001          CSUBROUTINE OF THE RATE OF ENERGY TRANSFER DUE TO
0002          CNONLINEAR WAVE-WAVE INTERACTIONS CALCULATED BY
0003          CBARNEET'S PARAMETRIC EQUATION
0004          CYY=INPUT WAVE HEIGHT SPECTRUM,DF=BANDWIDTH OF SPTR
0005           SUBROUTINE WNII(YY,DF)
0006           DIMENSION YY(257)
0007           COMMON A(257),B(257),SWW(257)
0008           SUMY=0.
0009           SUMYF=0.
0010           DO 1 I=1,257
0011           F=DF*FLOAT(I-1)
0012           SUMY=SUMY+YY(I)
0013         1 SUMYF=SUMYF+YY(I)*F*F
0014           E=SUMY*DF
0015           F0=(SUMYF*DF/E)**0.5
0016           F10=(F0*10.)**7*E*E/980.66**4
0017           B1=7.5*F10*(1.+2048./(45.*3.14159))
0018           A1=4.4*F10*E*F0*10.*3.*3.14159/8.
0019           C=980.66*DF
0020           FS3=0.53*F0
0021           F42=0.42*F0
0022           A(1)=0.
0023           B(1)=0.
0024           SWW(1)=0.
0025           DO 2 I=2,257
0026           F=DF*FLOAT(I-1)
0027           F5=F-FS3
0028           IF(F5-0.)3,3,4
0029         3 B(I)=0.
0030           GO TO 5
0031         4 B(I)=B1*F5*F5*FS/F*YY(I)*C
0032         5 F1=F0/F
0033           F2=1.-0.42*F1
0034           F3=1.-F1
0035           F4=-4.*F3*F3+0.1*(F1**5)
0036           IF(F-F42)6,6,7
0037         6 A(I)=0.
0038           GO TO 8
0039         7 A(I)=A1*F2*F2*F2*EXP(F4)*C
0040         8 SWW(I)=A(I)-B(I)
0041         2 CONTINUE
0042           WRITE(6,9)
0043         9 FORMAT(1H1)
0044           WRITE(6,13)E,F0,A1,B1
0045        13 FORMAT(1X,"E=",E10.4,"F0=",E10.4,"A1=",E10.4,"B1="
0046          1,E10.4)
0047           RETURN
0048           END
**** LIST END ****
```

Table 5.1

Friction velocity

x (m)	3.46			6.51			9.48			12.61			15.66		
u_∞ (m/sec)	6.76	7.62	8.43	6.92	7.73	8.62	7.02	7.90	8.81	7.09	8.01	8.88	7.26	8.10	8.97
u_* (m/sec)	0.56	0.72	0.76	0.64	0.73	0.74	0.61	0.63	0.67	0.59	0.68	0.74	0.61	0.69	0.71
$\hat{x}$ (xg/u_*^2)	107	66	59	158	120	116	249	232	206	350	267	329	416	327	304

Notes: x is the fetch, $\hat{x}$ is the normalized fetch, u_∞ is the free stream velocity, u_* is the friction velocity and g is the gravitational acceleration.

Table 5.2

Constant of white-capping dissipation model

u_∞ (m/sec)	(1) $\times 10^3$	(2) $\times 10^3$	(3) $\times 10^3$	(4) $\times 10^3$
8.88	0.5046	0.4368	0.5406	0.5351
8.01	0.2627	0.3807	0.4889	0.5189
7.09	0.1728	0.3235	0.3683	0.3365

Notes: (1), (2), (3) and (4) corresponding to fetches between 3.46 m and 6.51 m, 6.51 m and 9.48 m, 9.48 m and 12.61 m, and 12.61 m and 15.66 m, respectively.

Table C-1

Mean momentum transfer in a developing turbulent boundary layer

u_∞ (m/sec)	Fetch (m)	(1)*	(2)*	(3)*	(4)*	(5)*	(6)*	(7)	(8)	(9) γ
8.43	3.46	2.709	0.653	0.0115	1.986	3.374	5.360	0.803	0.194	0.629
8.62	6.51	3.088	0.172	0.0085	2.079	3.269	5.348	0.945	0.053	0.611
8.81	9.48	3.983	1.665	0.0094	2.729	5.657	8.386	0.704	0.294	0.674
8.88	12.61	4.238	2.371	0.0086	2.843	6.618	9.461	0.640	0.358	0.700
8.97	15.66	4.539	2.335	0.0078	2.873	6.882	9.755	0.660	0.339	0.705
7.62	3.46	1.561	0.221	0.0093	1.416	1.791	3.207	0.872	0.123	0.558
7.73	6.51	2.042	0.172	0.0079	1.583	2.222	3.805	0.919	0.077	0.584
7.90	9.48	2.572	1.703	0.0073	2.019	4.282	6.301	0.601	0.398	0.680
8.01	12.61	3.145	2.660	0.0067	1.940	5.812	7.521	0.541	0.458	0.750
8.10	15.66	3.328	2.017	0.0061	2.183	5.351	7.534	0.622	0.377	0.710
6.76	3.46	0.780	0.290	0.0068	0.969	1.077	2.046	0.724	0.269	0.527
6.92	6.51	1.446	0.539	0.0064	1.202	1.991	3.193	0.726	0.271	0.624
7.02	9.48	1.857	0.487	0.0043	1.287	2.072	3.359	0.765	0.235	0.617
7.09	12.61	1.694	0.846	0.0051	1.372	2.545	3.917	0.666	0.332	0.650
7.26	15.66	2.241	0.652	0.0052	1.511	2.898	4.409	0.773	0.225	0.657
							Average:	0.731	0.267	0.645

Notes: u_∞ is mean free stream velocity, $(1) = \overline{\tilde{p} \, \partial\eta/\partial x}$, $(2) = \rho_a \overline{u'u'} \, \partial\eta/\partial x$, $(3) = -\mu \, \overline{\partial\tilde{u}/\partial x \cdot \partial\eta/\partial x}$,
$(4) = -\rho_a \overline{u'v'}$, $(5) = (1) + (2) + (3)$, $(6) = (1) + (2) + (3) + (4)$, $(7) = (1) / (5)$,
$(8) = (2) / (5)$, $(9) = (5) / (6) = \gamma$

* is in dyne/cm^2

-113-

Table D-1

Mean energy transfer in a developing turbulent boundary layer

u_∞ (m/sec)	Fetch (m)	(1)* $\times 10^{-2}$	(2)* $\times 10^{-2}$	(3)* $\times 10^{-2}$	(4)* $\times 10^{-2}$	(5)* (dyne/cm²) $\times 10^{-2}$	(6) (m/sec)	(7)* $\times 10^{-2}$	(8)* $\times 10^{-2}$	(9)* $\times 10^{-2}$	(10)* γ_E	(11)	(12)
8.43	3.46	9.17	-0.160	-0.036	0.030	5.360	0.253	1.36	10.36	9.00	0.87	0.13	0.02
8.62	6.51	14.22	-0.190	-0.030	0.033	5.348	0.259	1.39	15.42	14.03	0.91	0.09	0.02
8.81	9.48	23.01	-0.600	-0.140	0.060	8.386	0.264	2.22	24.55	22.33	0.91	0.09	0.03
8.88	12.61	32.68	-0.570	-0.320	0.066	9.461	0.266	2.52	34.38	31.86	0.93	0.07	0.03
8.97	15.66	45.33	-0.980	-0.160	0.064	9.755	0.269	2.63	46.88	44.25	0.94	0.06	0.03
7.62	3.46	3.71	-0.048	-0.019	0.013	3.207	0.229	0.74	4.40	3.66	0.83	0.17	0.02
7.73	6.51	7.79	-0.133	-0.036	0.018	3.805	0.232	0.88	8.52	7.64	0.90	0.10	0.02
7.90	9.48	11.51	-0.400	-0.110	0.030	6.301	0.237	1.49	12.52	11.03	0.88	0.12	0.05
8.01	12.61	19.02	-0.460	-0.170	0.037	7.521	0.240	1.86	20.29	18.43	0.91	0.09	0.03
8.10	15.66	26.59	-0.440	-0.150	0.039	7.534	0.243	1.83	27.87	26.04	0.93	0.07	0.02
6.76	3.46	1.36	-0.016	-0.008	0.006	2.046	0.203	0.42	1.76	1.34	0.76	0.24	0.02
6.92	6.51	4.13	-0.022	+0.002	0.010	3.193	0.208	0.66	4.78	4.12	0.86	0.14	0.01
7.02	9.48	7.10	-0.150	-0.036	0.015	3.359	0.211	0.71	7.64	6.93	0.91	0.09	0.03
7.09	12.61	7.66	-0.200	-0.041	0.018	3.917	0.213	0.84	8.28	7.44	0.90	0.10	0.03
7.26	15.66	13.98	-0.320	+0.008	0.020	4.409	0.218	0.96	14.65	13.69	0.93	0.07	0.02
									Average:		0.89	0.11	0.025

Notes: u_∞ is mean free stream velocity, (1) = $-\overline{pv}$, (2) = $-\rho_a u'v' \frac{\partial \eta}{\partial x} \overline{v}$, (3) = $-\rho_a \overline{v'^2 v}$,
(4) = $\rho_a \overline{u'v'} \frac{\partial \eta}{\partial x} \overline{v}$, (5) = Total mean horizontal momentum transferred into water [from Table (C.1),
column (6)], (6) = Estimated surface current drift velocity ≈ 3% u_∞, (7) = (5) × (6) = Mean energy
transferred into current, (8) = (1) + (2) + (3) + (4) + (7) = Total energy transferred into water,
(9) = (1) + (2) + (3) + (4) = Energy transferred into waves, (10) = (9) / (8), (11) = (7) / (8),
(12) = [(2) + (3) + (4)] / (9)

* is in erg-cm⁻²-sec⁻¹

-114-
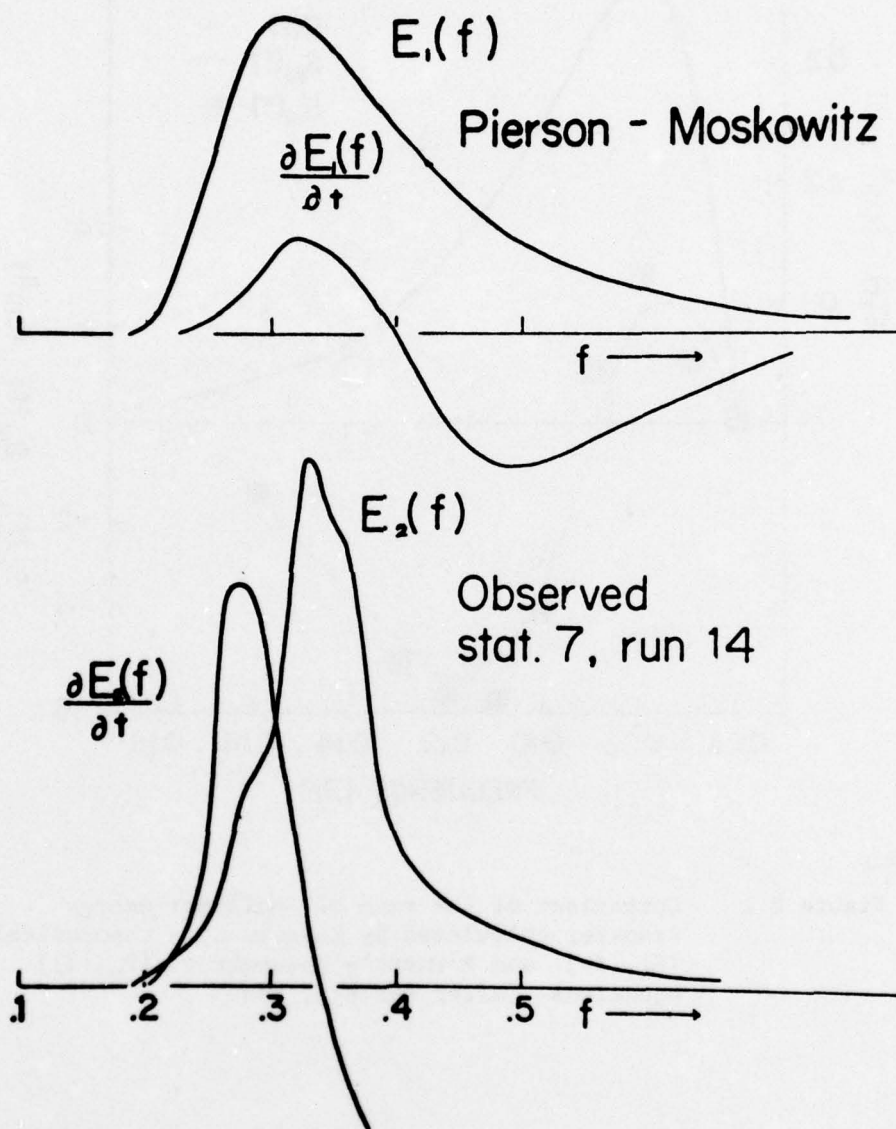
Figure 1.1 Comparison of the rate of energy transfer of nonlinear wave-wave interactions ($\partial E/\partial t$) of Pierson-Moskowitz spectrum (E_1) and observed ocean spectrum (E_2) (after Barnett, 1971)
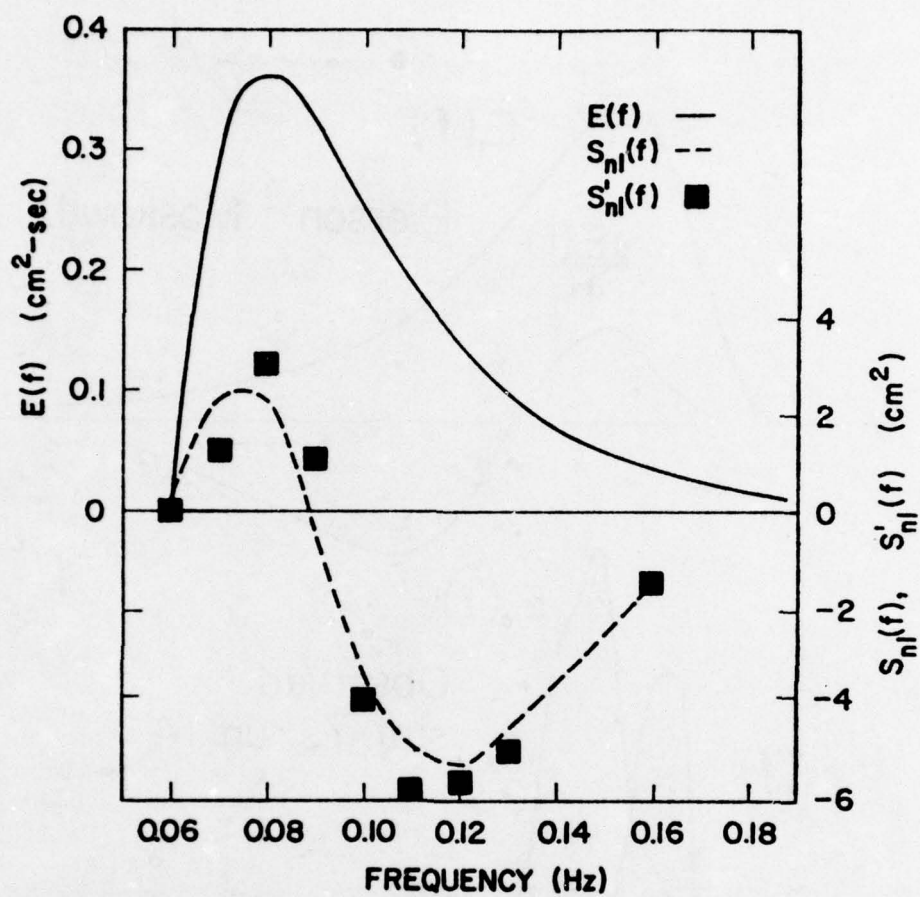
Figure 2.1   Comparison of the rate of nonlinear energy
transfer calculated by Hasselmann's theoretical
$[S'_{n1}(f)]$ and Barnett's parametric $[S_{n1}(f)]$
equations (after Barnett, 1966)
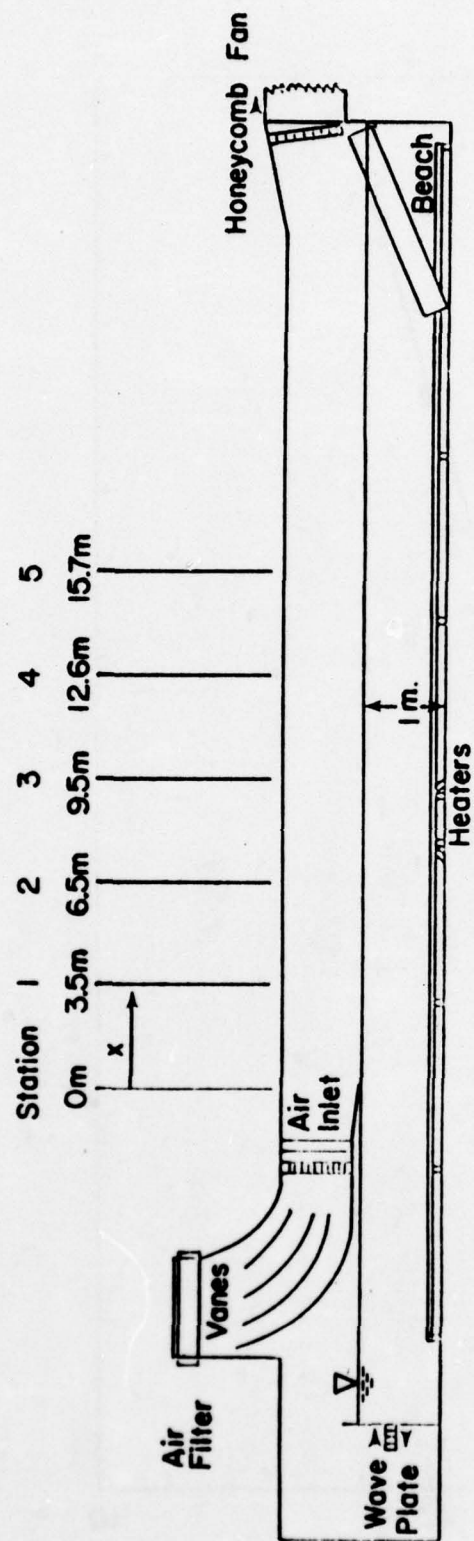
Figure 3.1   Schematic of Stanford wind-wave channel
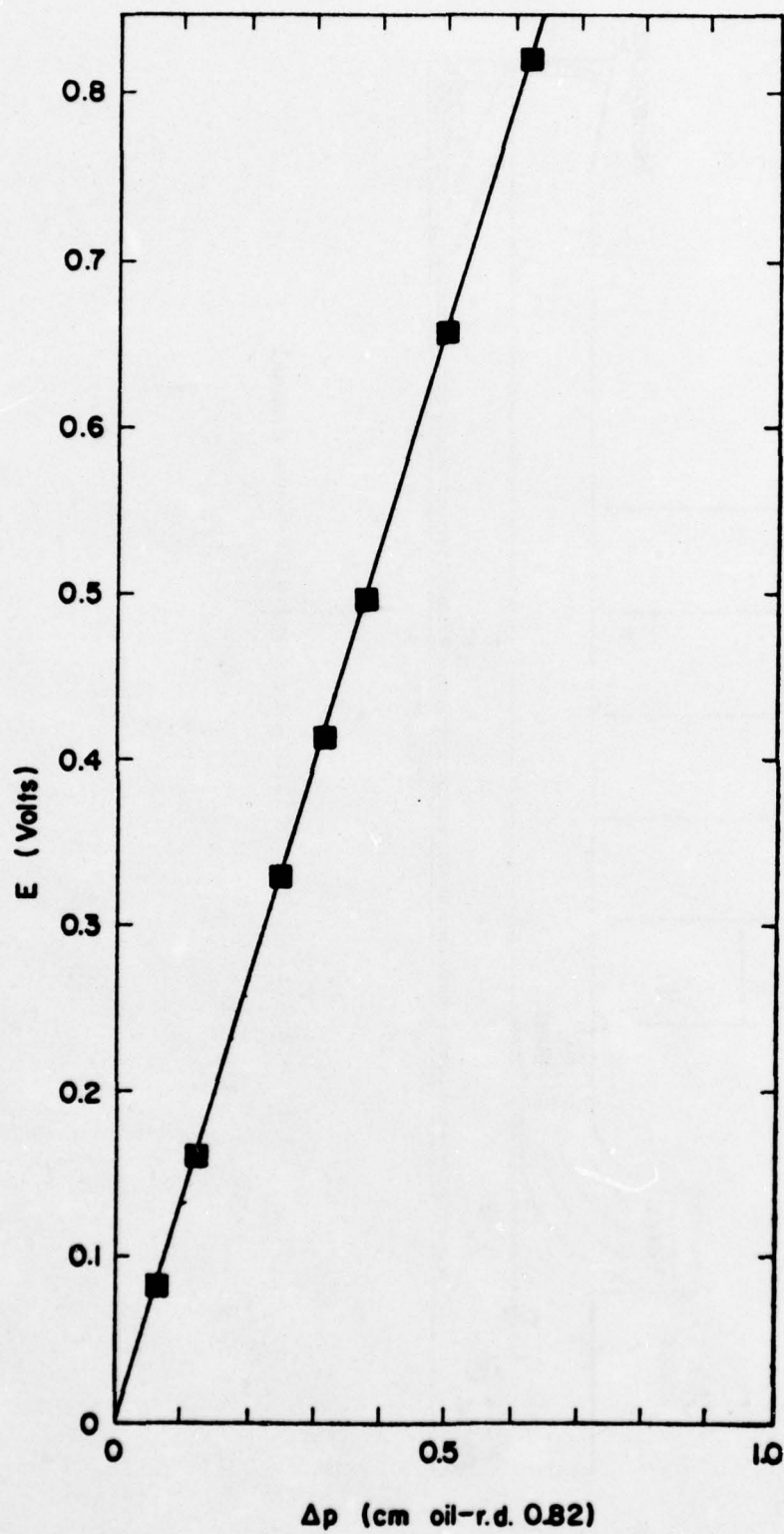
Figure 3.2   Pace pressure transducer calibration

-118-
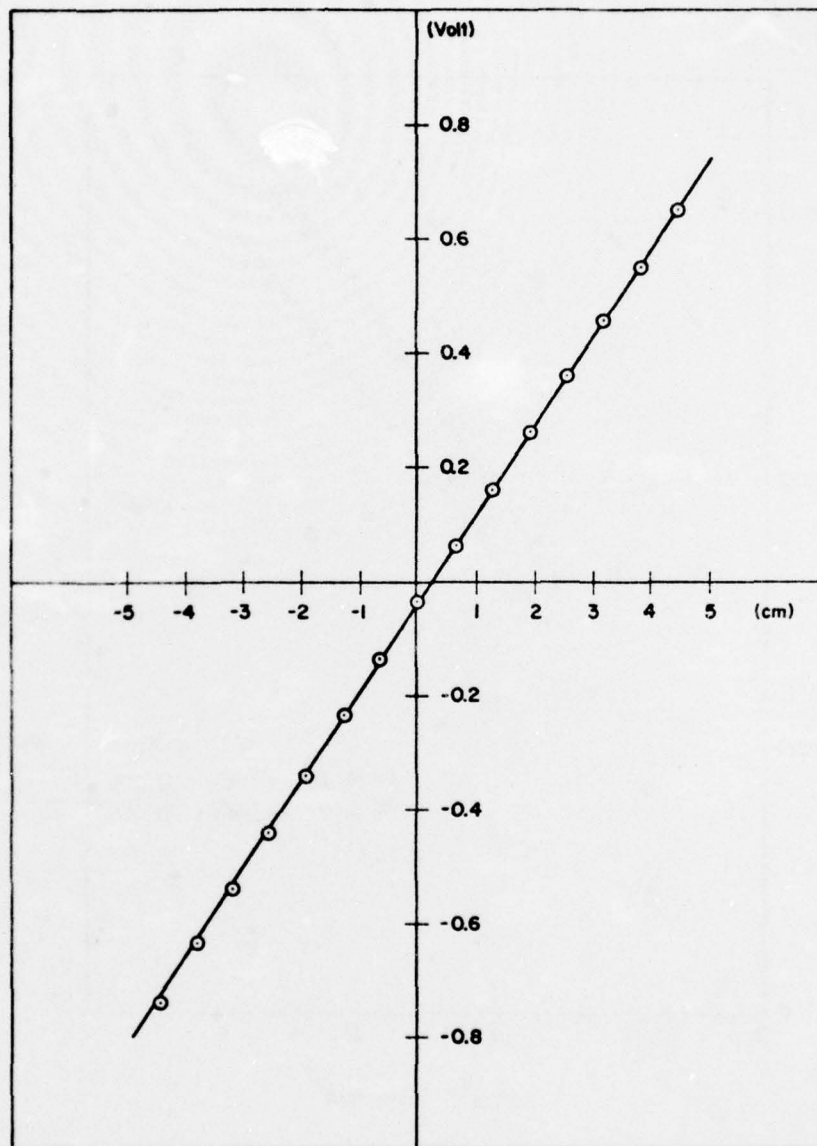
Figure 3.3   Capacitance wave height gauge calibration
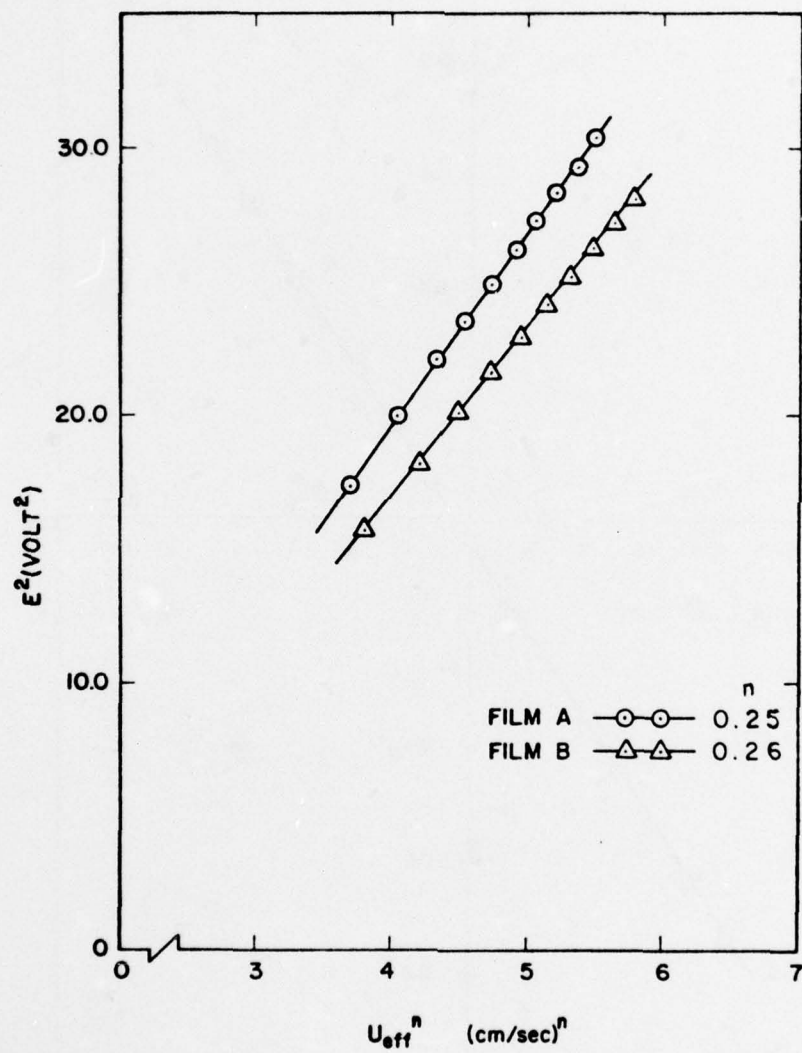
Figure 3.4   Cross hot films calibration

PRESSURE
DIAPHRAGM

PIEZOCERAMIC
ELEMENTS

SENSOR DISK

GASKET

0.05

7.62

0.16

0.32

0.03

0.16

0.32

0.32

0.635

L905

DRIVE PINS

"DUMMY" DIAPHRAGM FOR
ACCELERATION COMPENSATION

SECTION I-I

TRANSDUCER CASING

I

SUPPORTING TUBE

2.54

SENSOR DISK

I

UNIT:CM
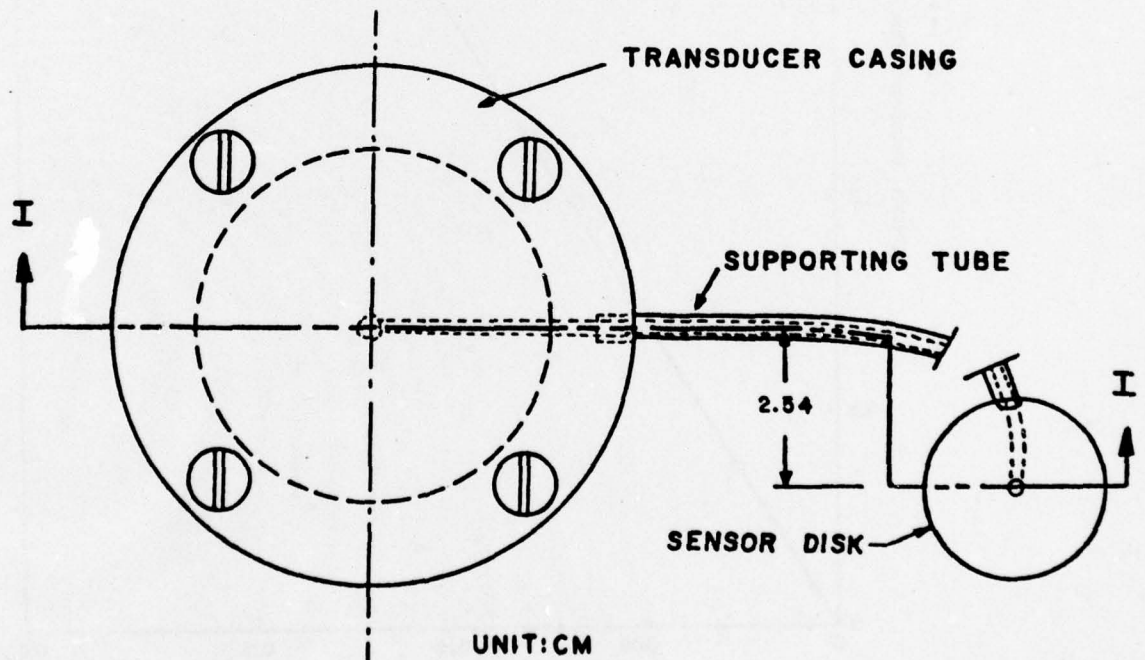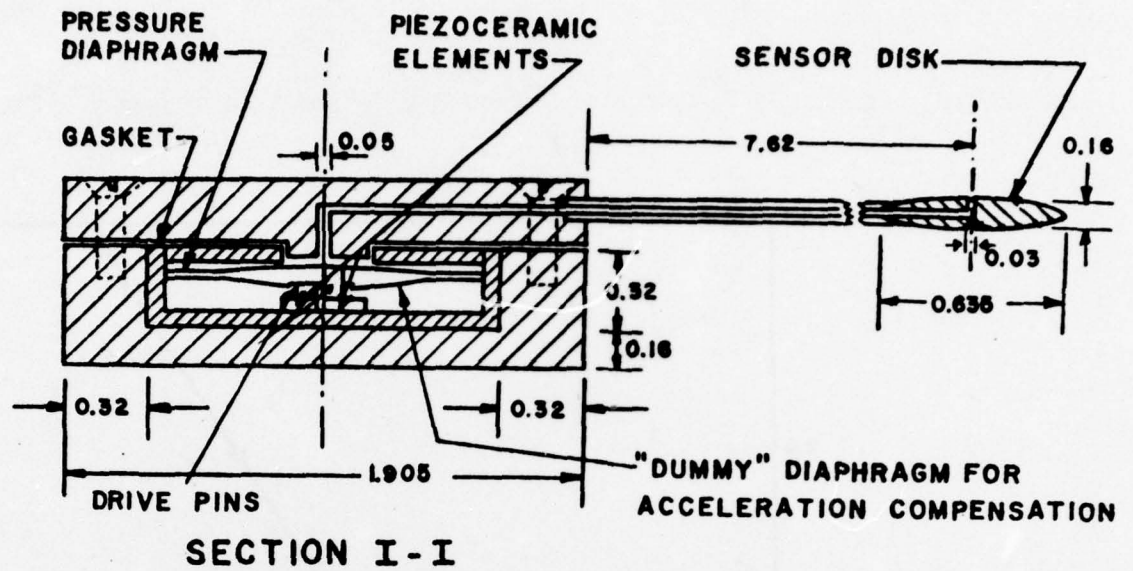
Figure 3.5   Detailed structure of crystal pressure
transducer (after Yu, el al., 1973)
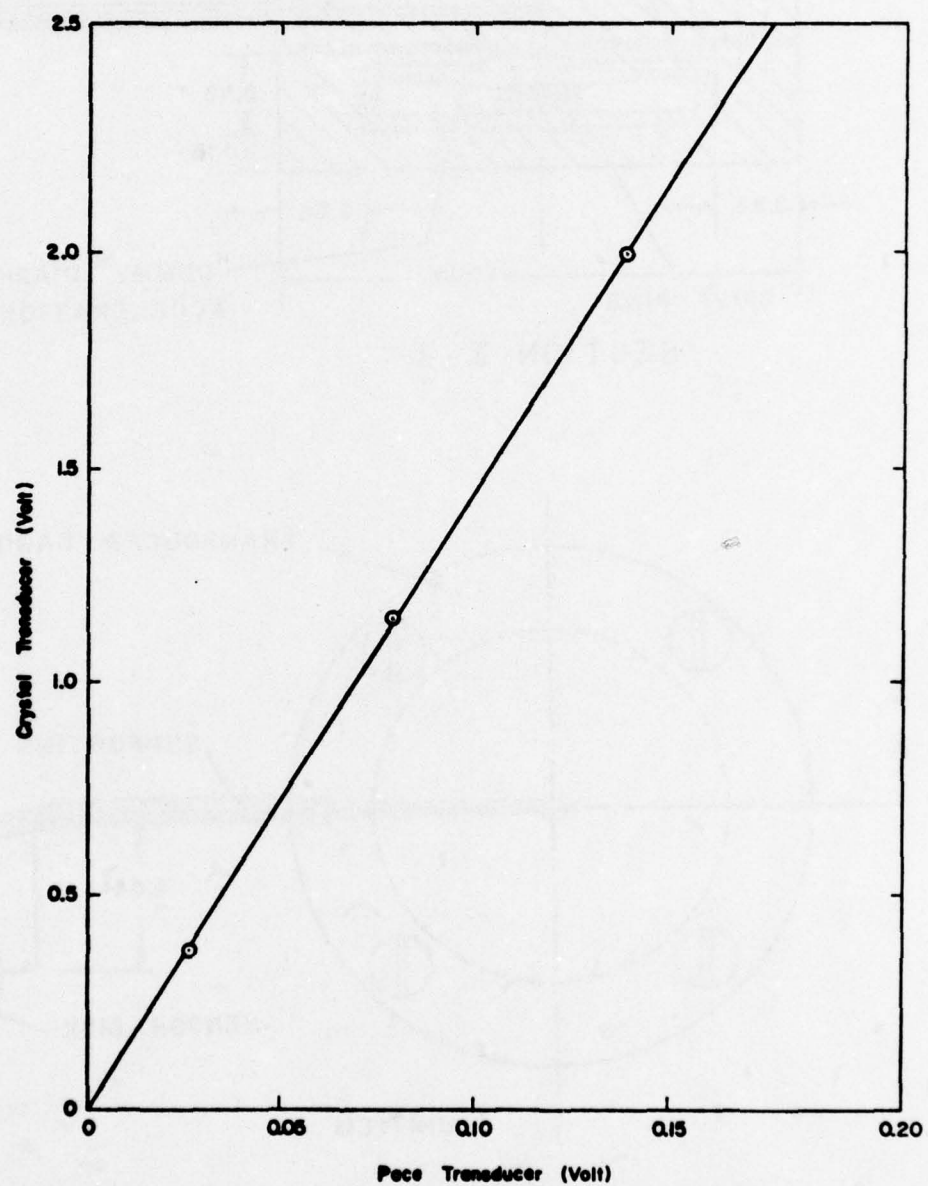
Figure 3.6 Calibration of crystal pressure transducer against Pace pressure transducer
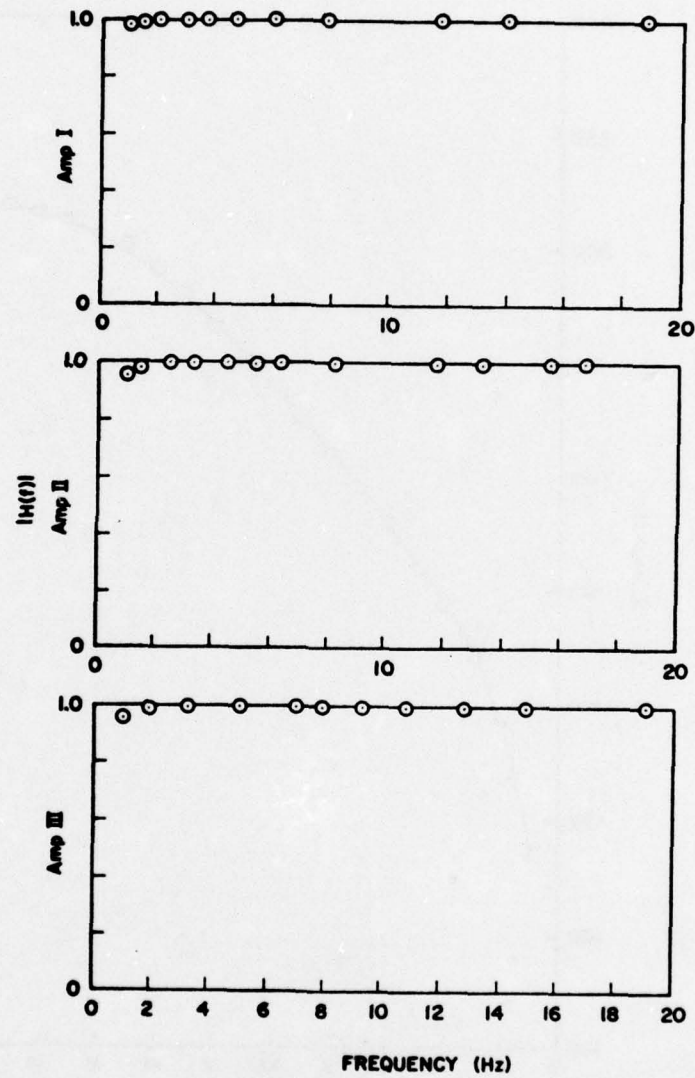
Figure 3.7 Calibration of the magnitude of crystal pressure transducer output versus frequency
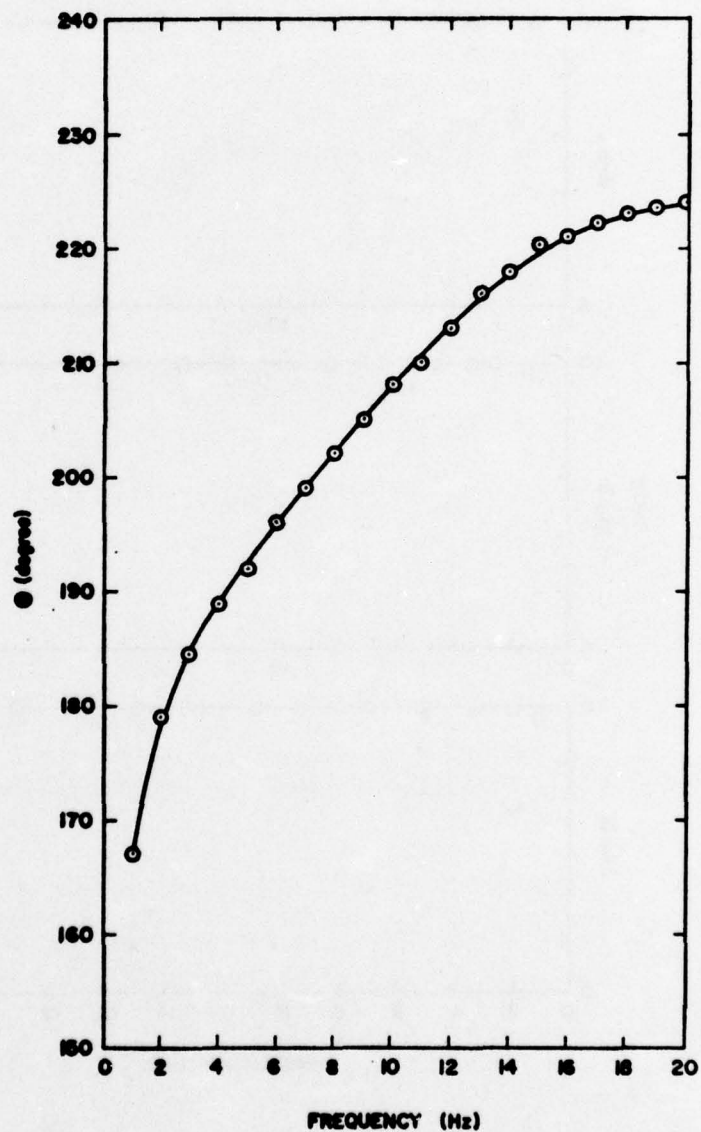
Figure 3.8 Calibration of phase lag of the sensing system of crystal pressure transducer versus the variation of frequency
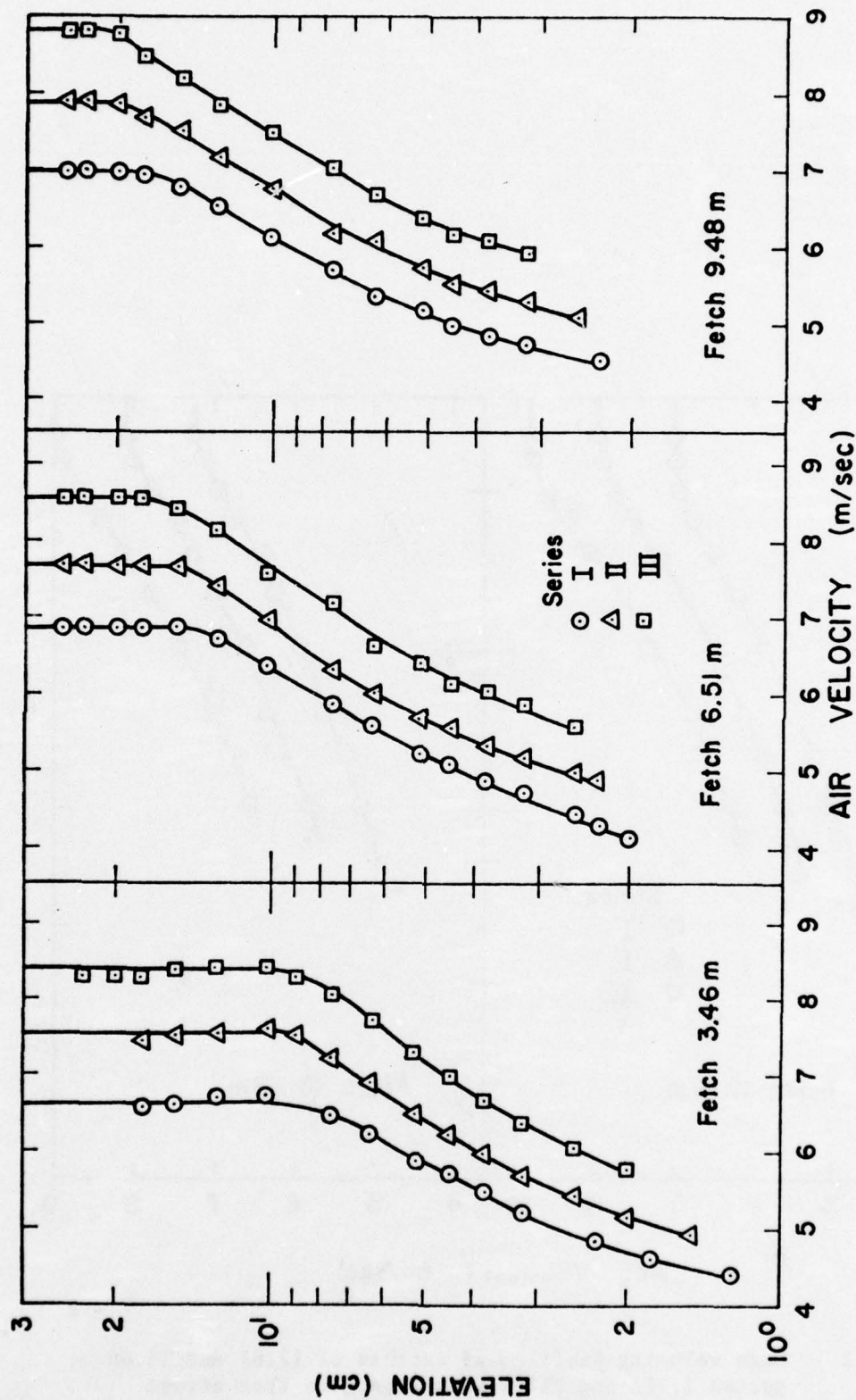
Figure 4.1   Mean air velocity profiles at fetches of 3.46, 6.51 and 9.48 m; series I, II and III corresponding to free stream velocities of 7.09, 8.01 and 8.88 m/sec, measured at fetch of 12.61 m, respectively.
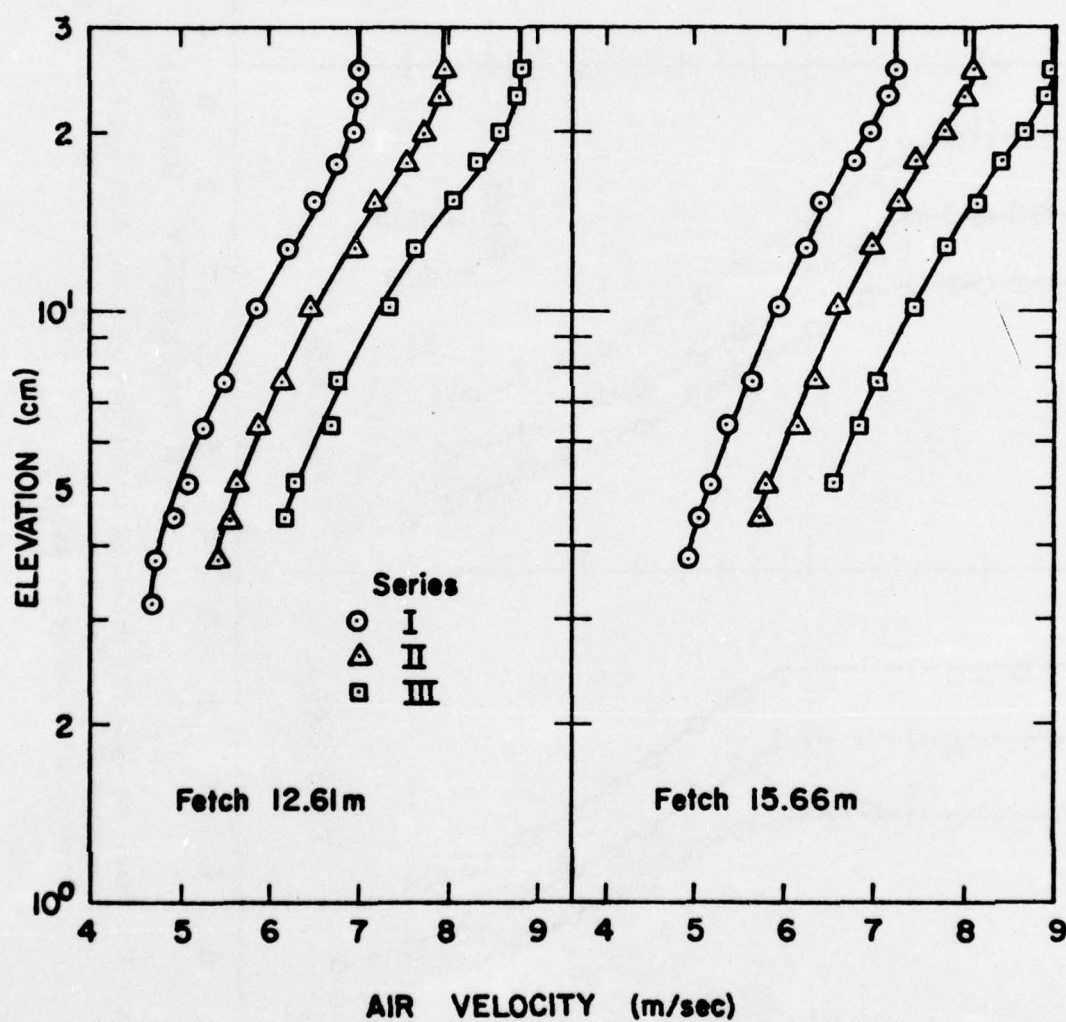
Figure 4.2   Mean velocity profiles at fetches of 12.61 and 15.66 m;
series I, II and III corresponding to free stream
velocities of 7.09, 8.01 and 8.88 m/sec, measured at
fetch of 12.61 m, respectively
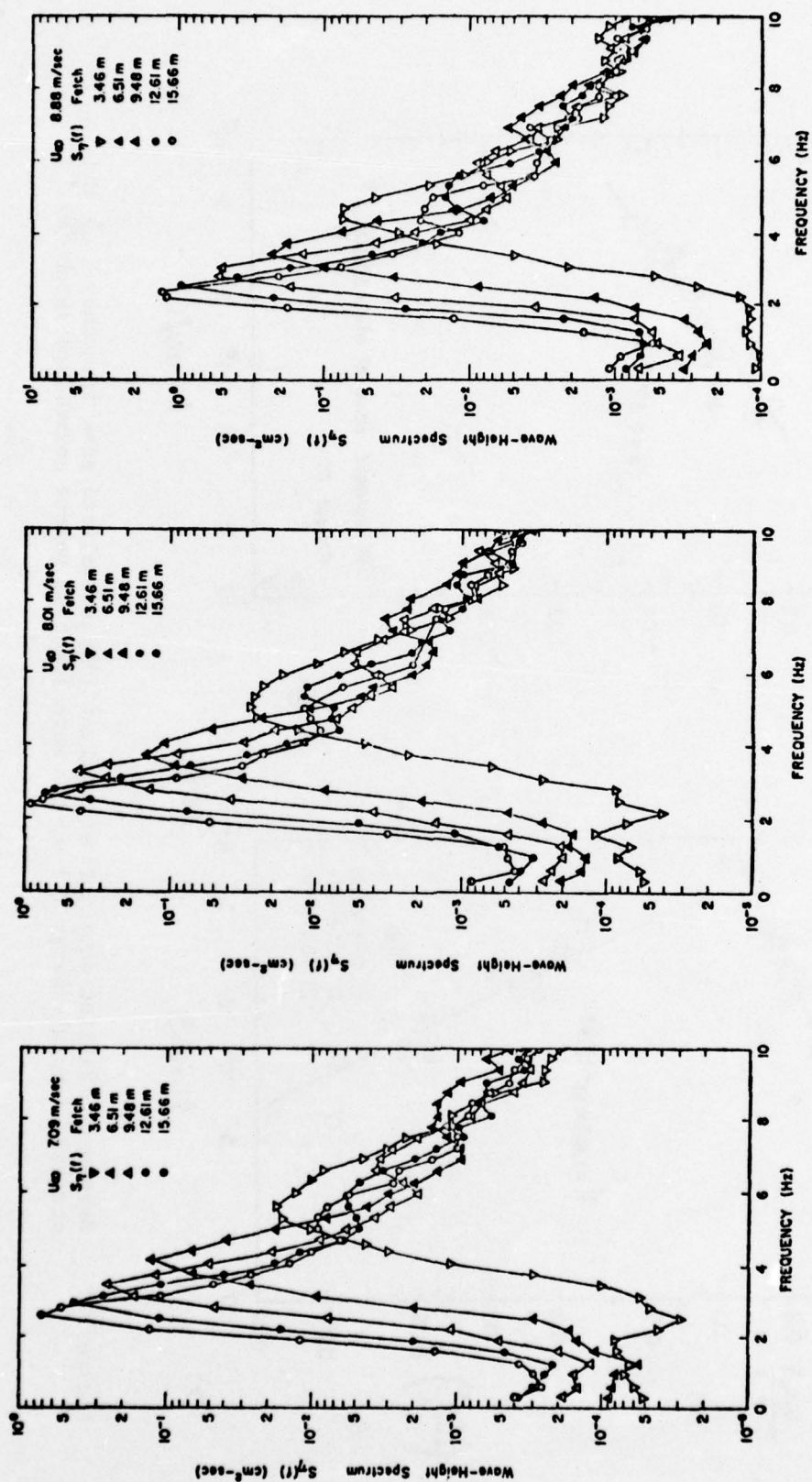
Figure 5.1   Power spectra of wave height for different fetches and wind speeds
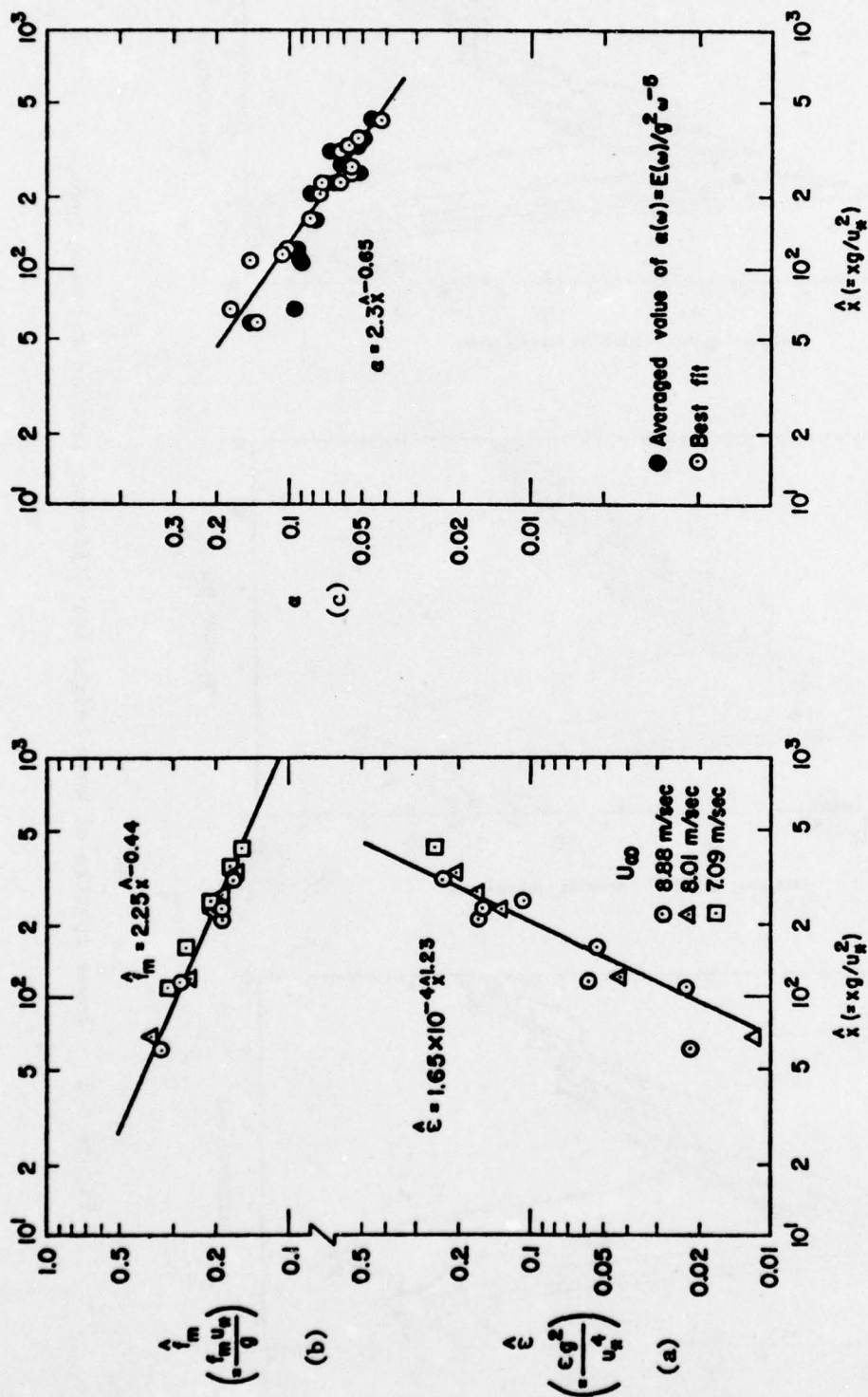
Figure 5.2 Curves of Phillips equilibrium constant (α), normalized peak frequency ($\hat{f}_m$) and normalized total energy ($\hat{\epsilon}$) of the wave spectrum versus normalized fetch ($\hat{x}$)

$$a = 0.35\hat{x}^{-0.22}$$

$$\hat{x}\ (= xg/u_*^2)$$

(a)
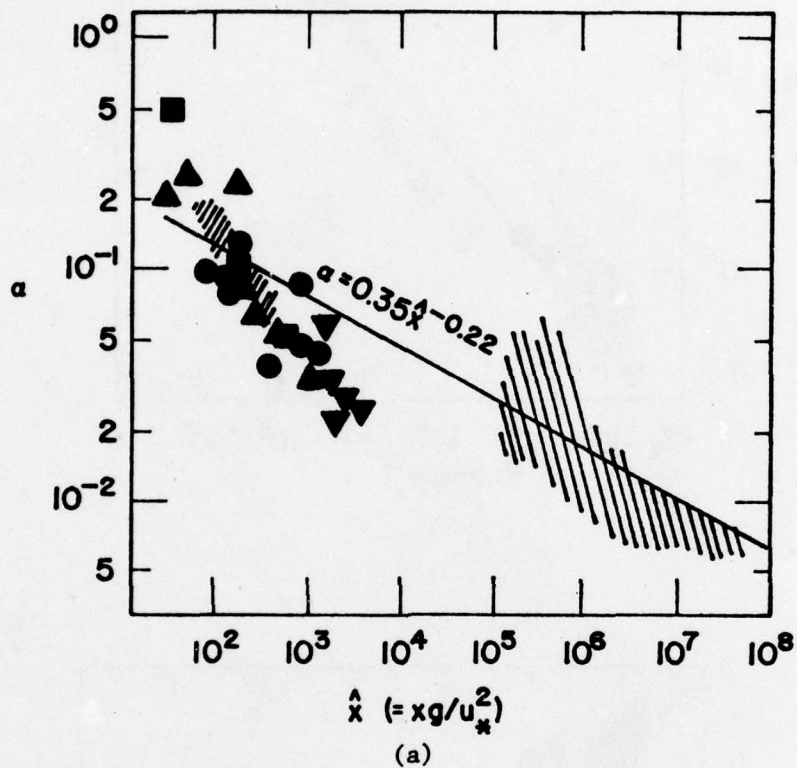
||||	Hasselmann et al. (1973)
●	Mitsuyasu (1968)
▼	Pierson and Stacy (1971)
■	Sutherland (1967)
▲	Toba (1971)
////	This experiment

Figure 5.3   Comparisons of present and previous laboratory and ocean results of (a) Phillips equilibrium constant (α), (b) normalized total energy ($\hat{\epsilon}$), and (c) normalized peak frequency ($\hat{f}_m$) of the wave spectrum versus normalized fetch ($\hat{x}$) (after Hasselmann, et al., 1973)

(b)

(c)
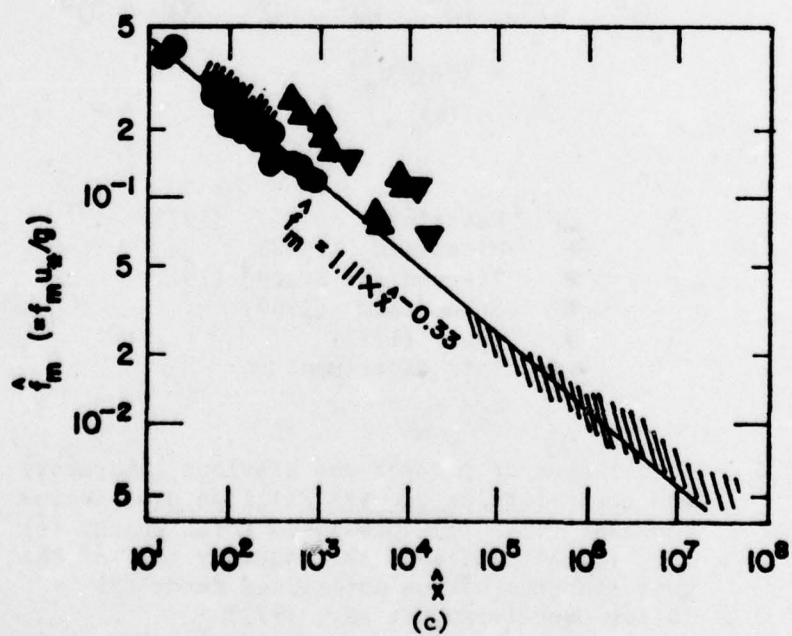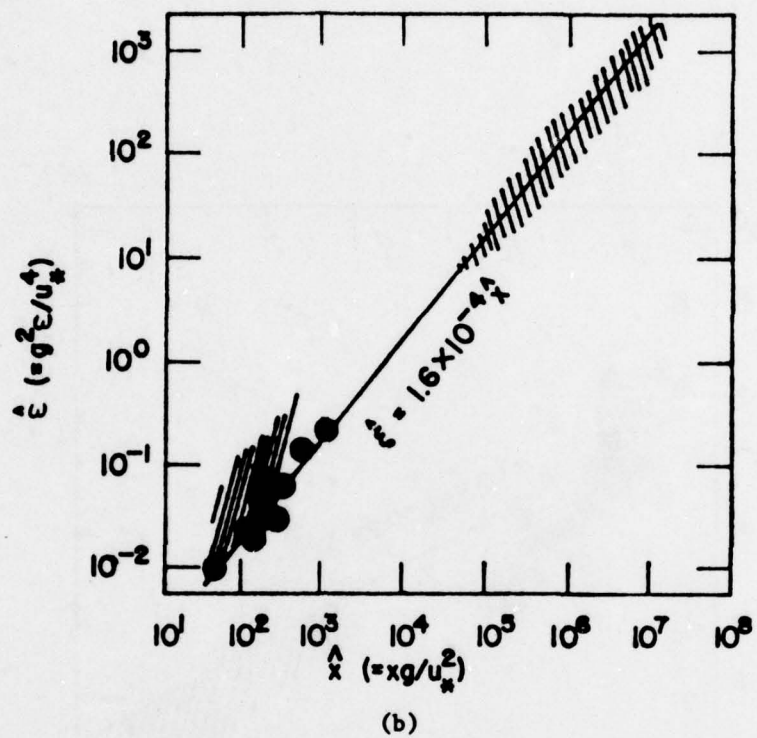
Figure 5.3   For legend see pp. 129

-130-
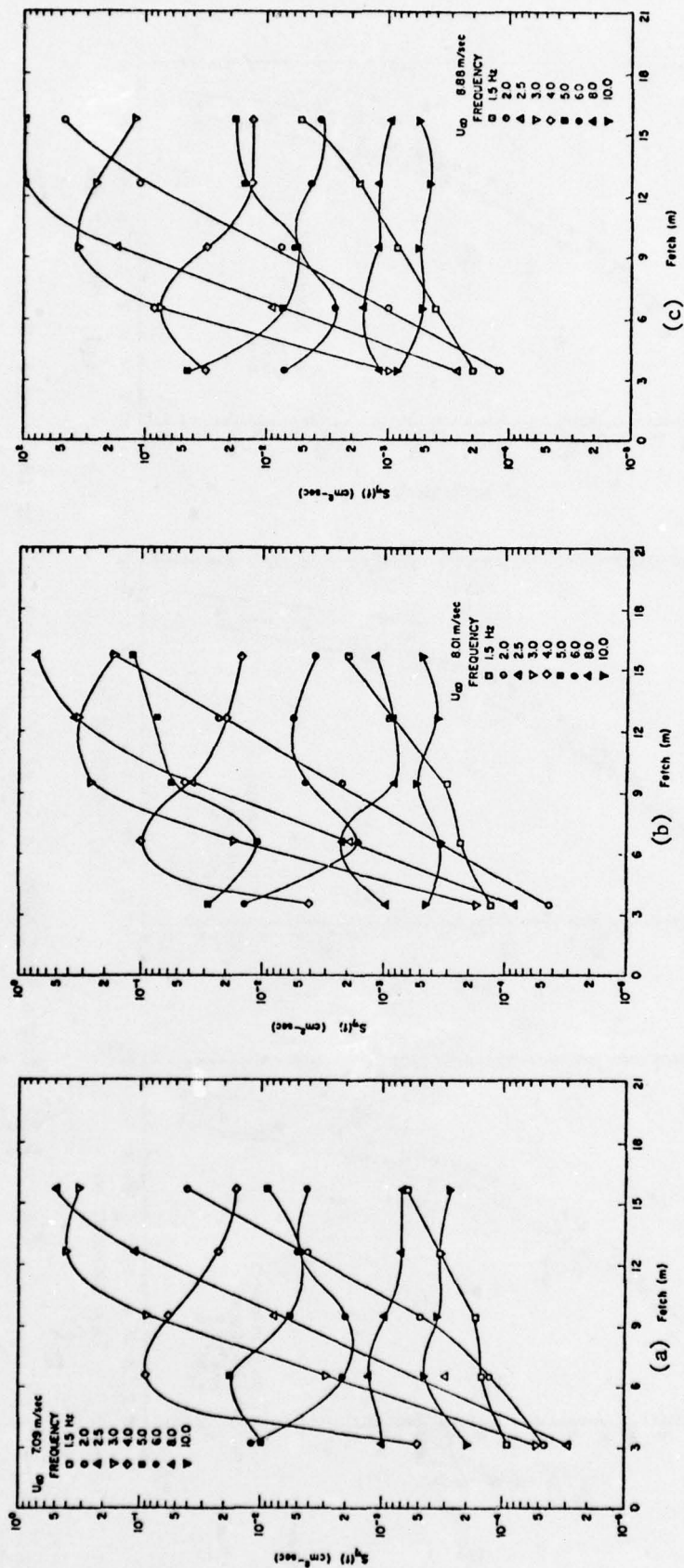
Figure 5.4   The variation of wave spectral components along fetch for
wind speeds of (a) 7.09, (b) 8.01 and (c) 8.88 m/sec
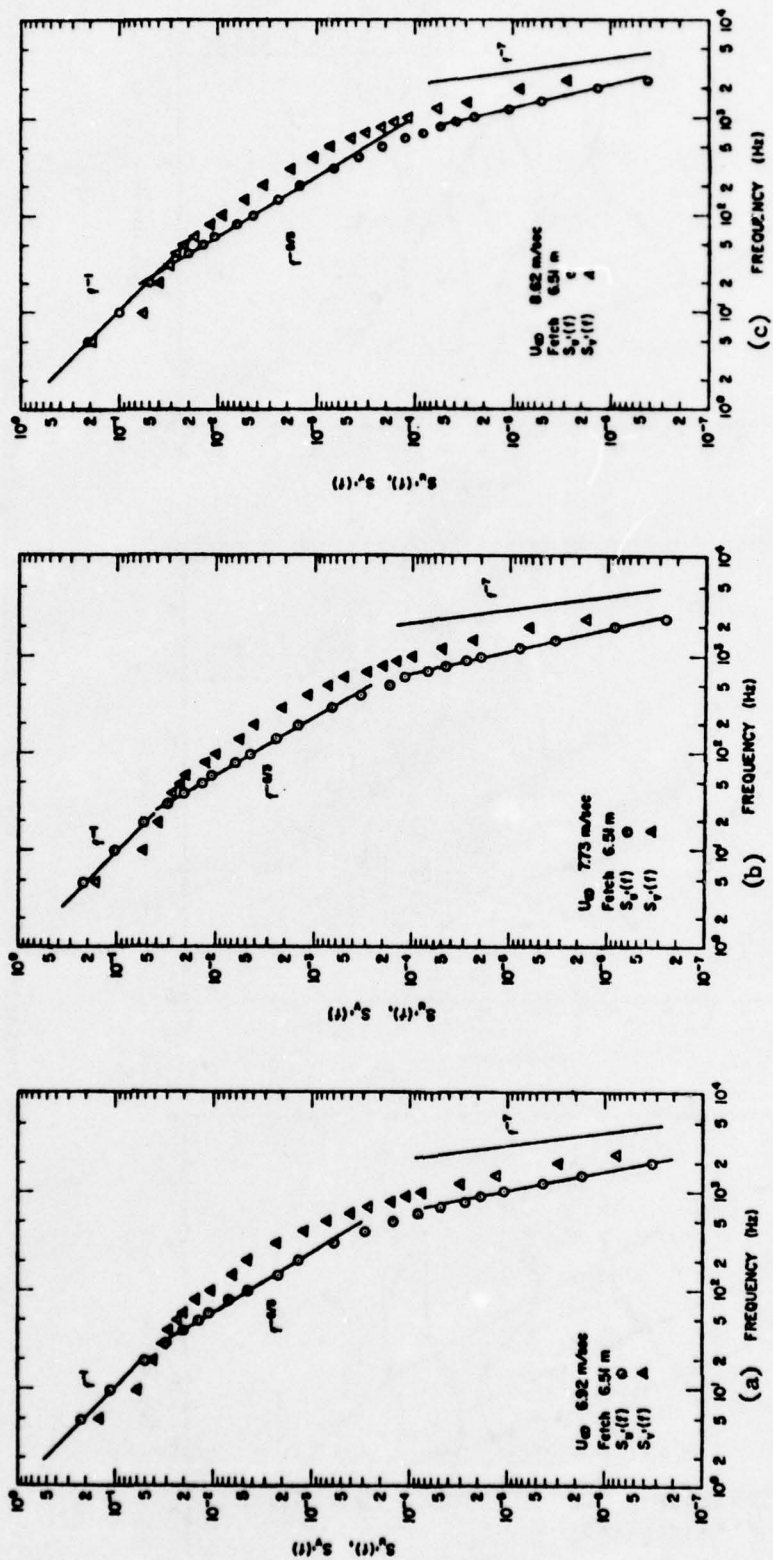
Figure 5.5   Normalized power spectra of u' and v'   at fetch of 6.51 m
for wind speeds of (a) 6.92,   (b) 7.73   and   (c) 8.62 m/sec

-132-
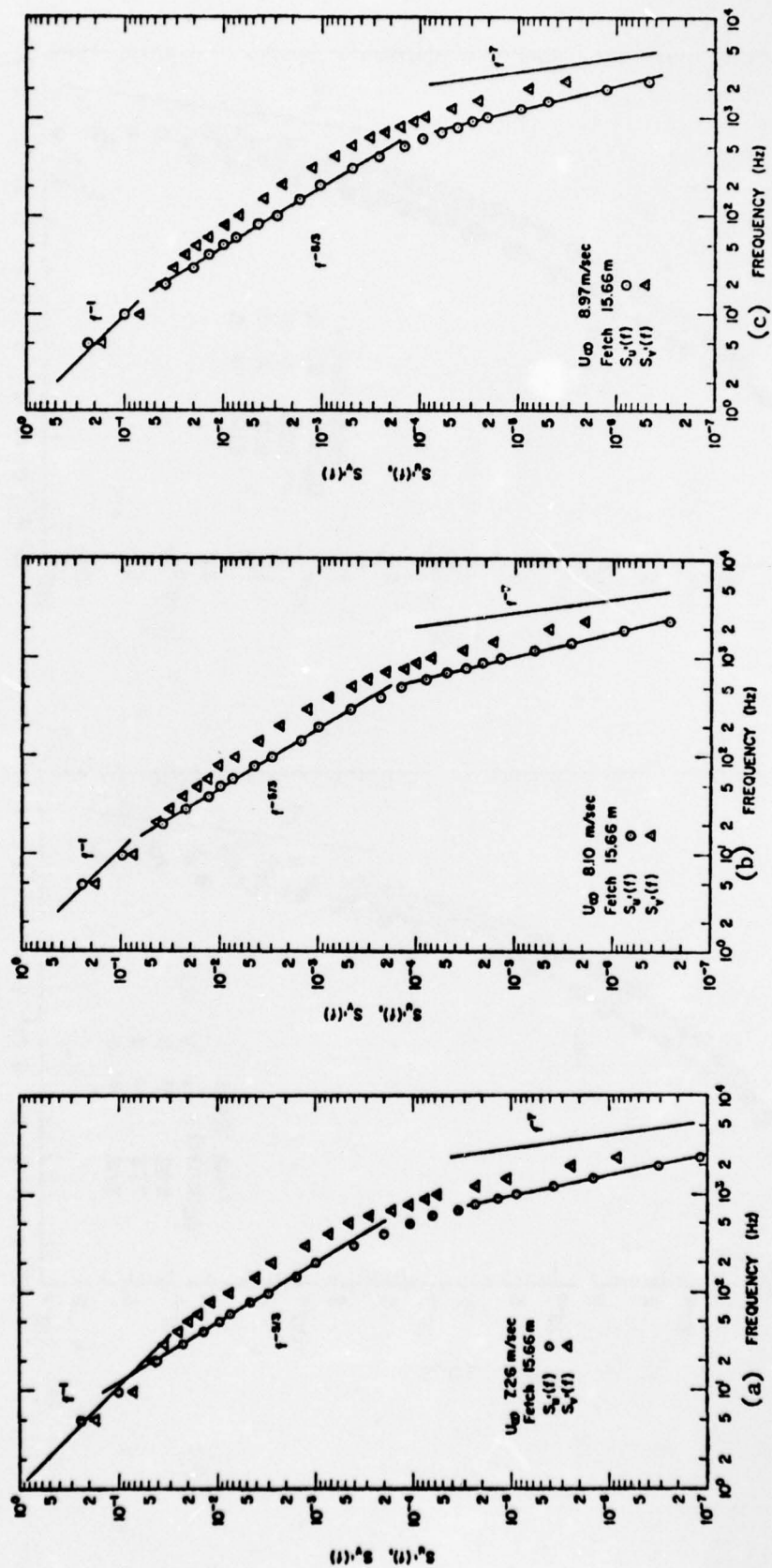
Figure 5.6   Normalized power spectra of u' and v' at fetch of 15.66 m
for wind speeds of (a) 7.26, (b) 8.10 and (c) 8.97 m/sec

-133-
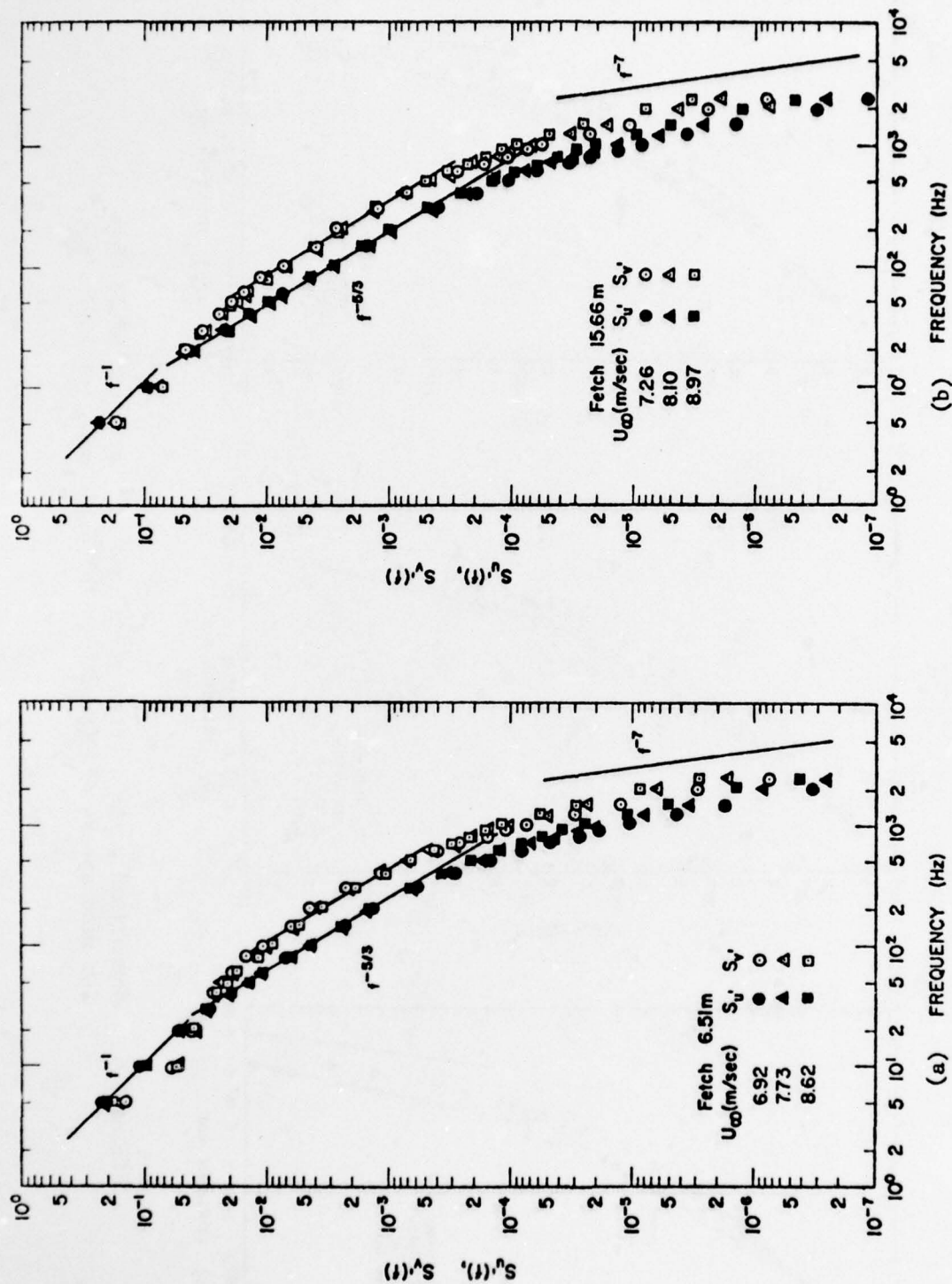
Figure 5.7   Normalized power spectra of u' and v' for different
wind speeds at fetches of (a) 6.51 and (b) 15.66 m
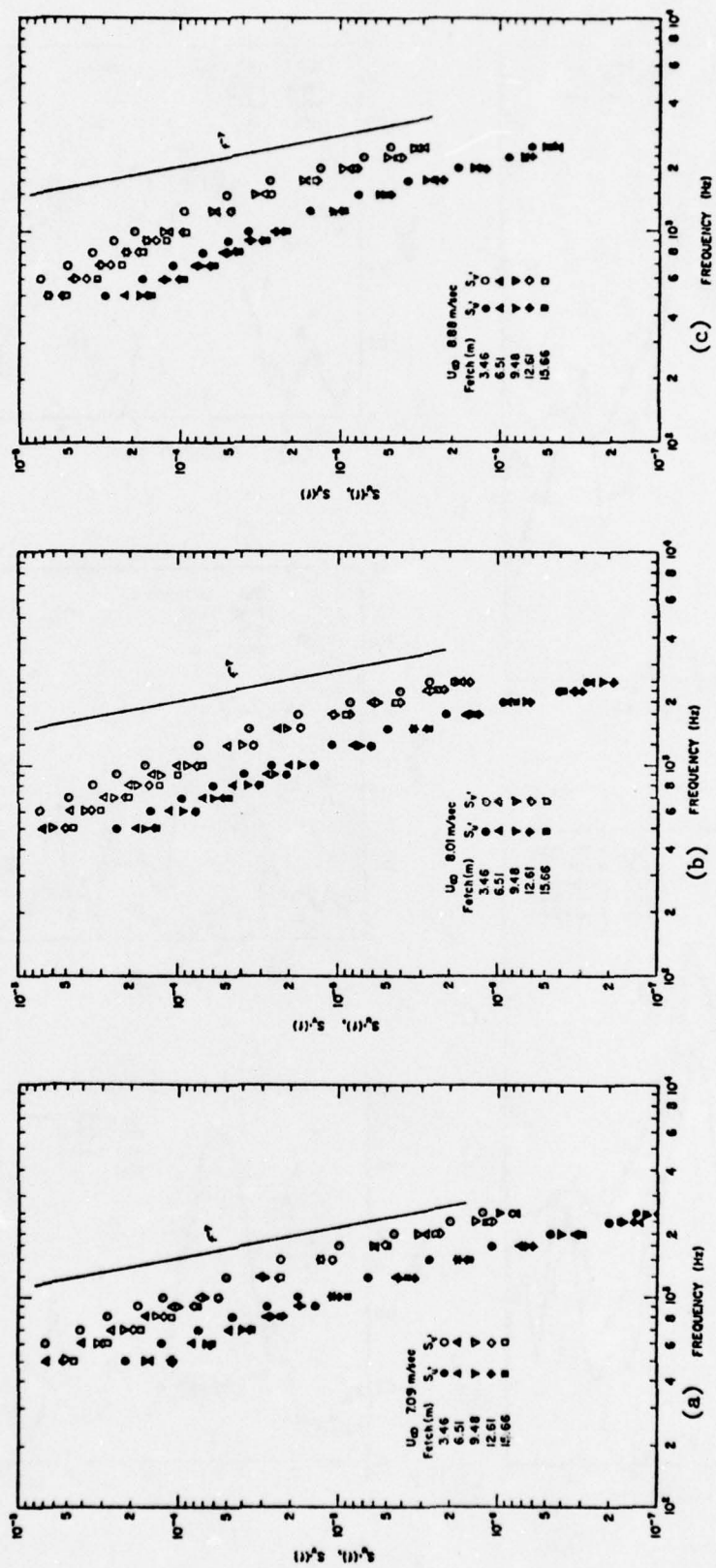
Figure 5.8   Normalized power spectra of u' and v' at different fetches
for wind speeds of (a) 7.09, (b) 8.01 and (c) 8.88 m/sec
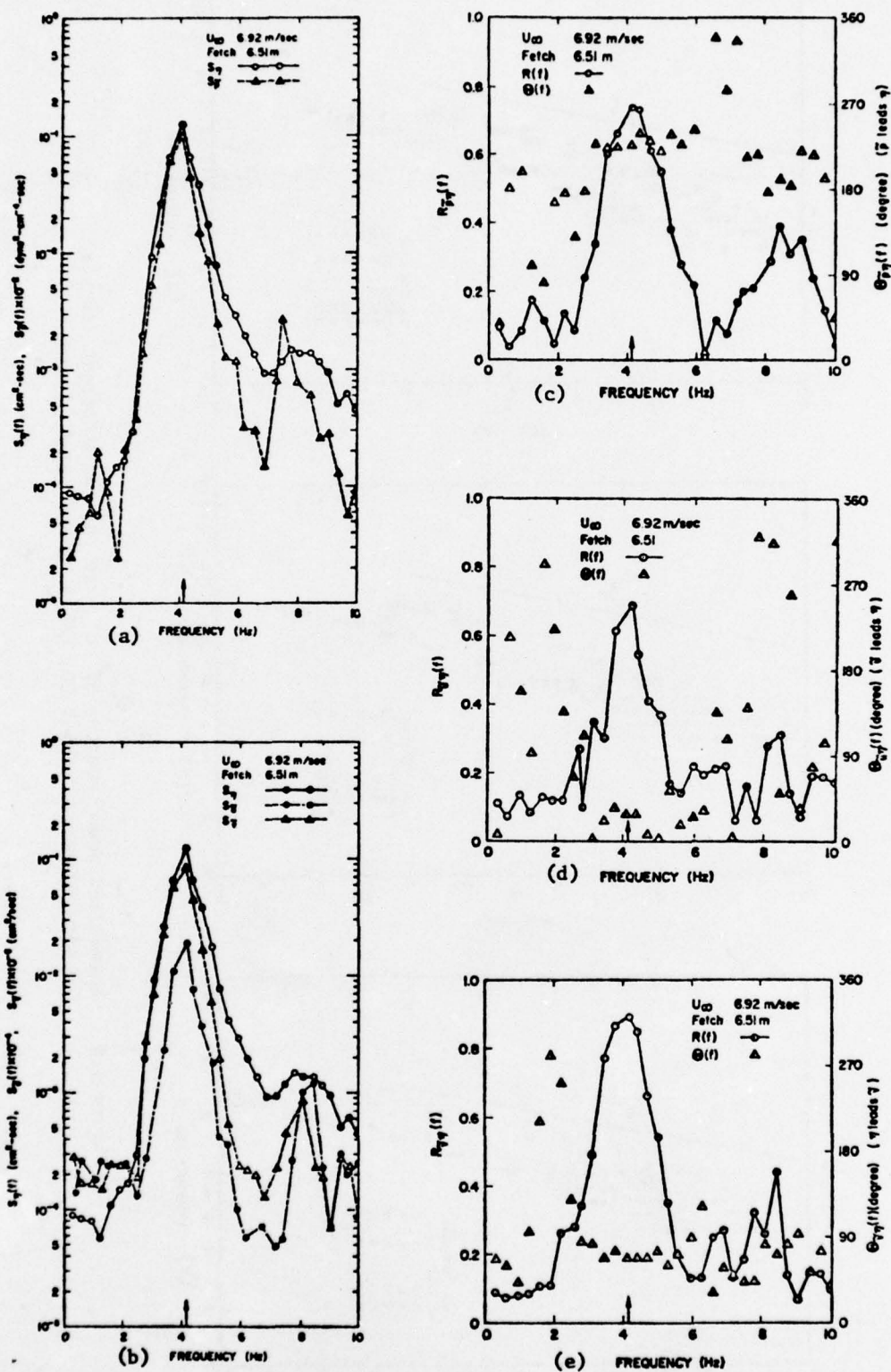
Figure 5.9   Power spectra of wave-induced pressure p̃ and velocity
             components ũ and ṽ, and spectra of coherence (R) and
             phase angle (θ) between p̃, ũ, ṽ and η at fetch of
             6.51 m and wind speed of 6.92 m/sec
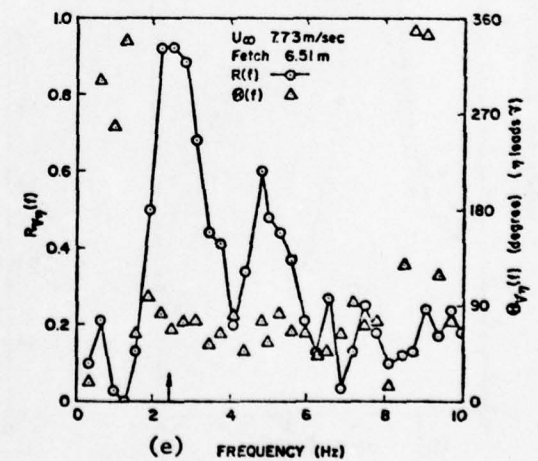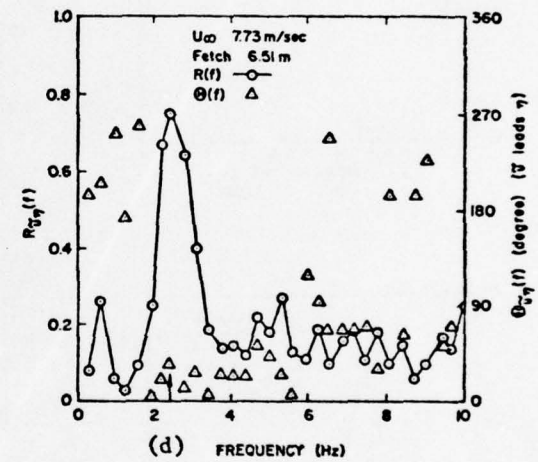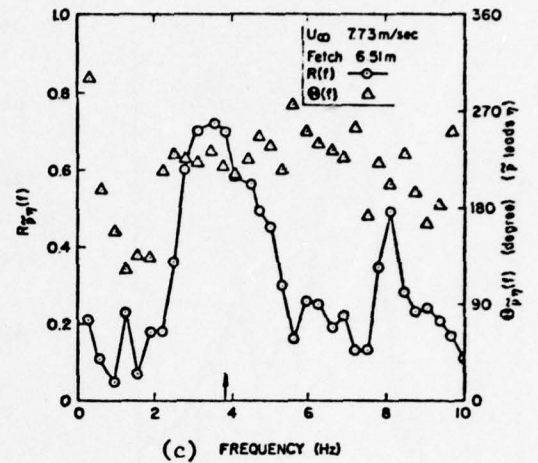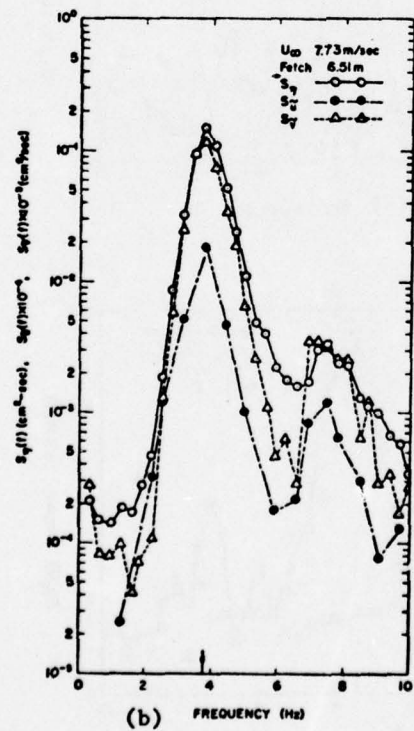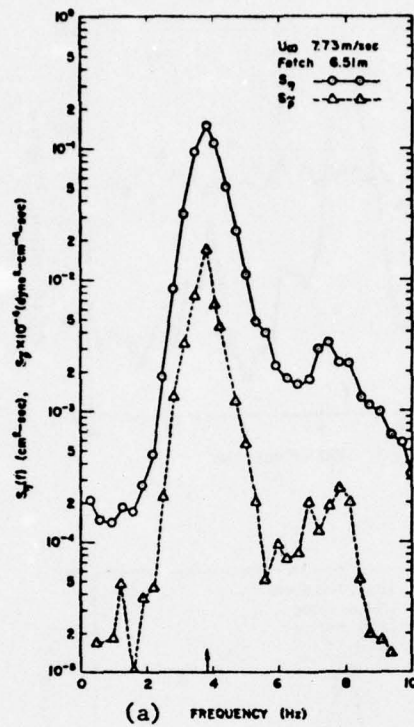
Figure 5.10   Power spectra of wave-induced pressure p̃ and velocity
                components ũ and ṽ, and spectra of coherence (R) and
                phase angle (θ) between p̃, ũ, ṽ and η at fetch   of
                6.51 m and wind speed of 7.73 m/sec

-137-
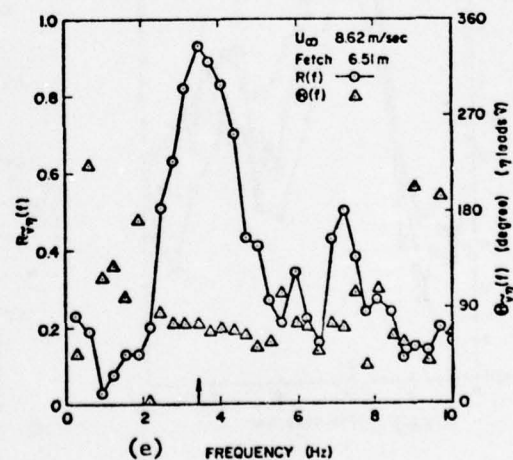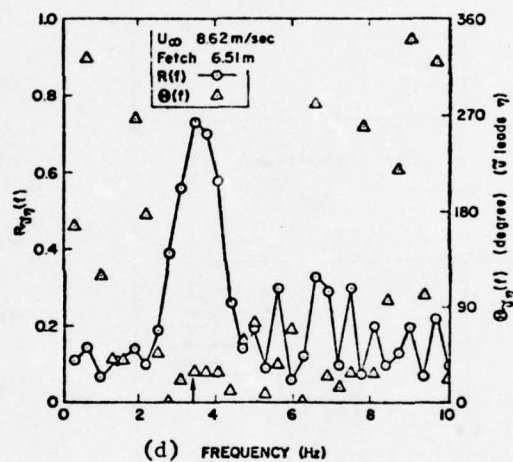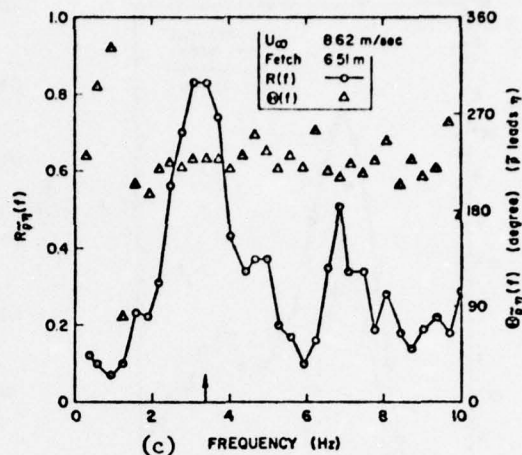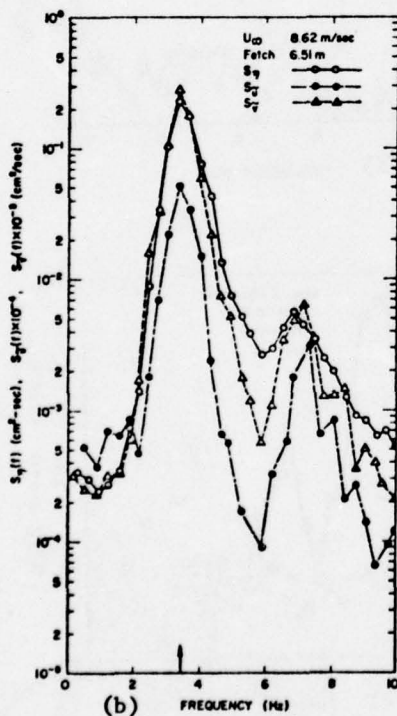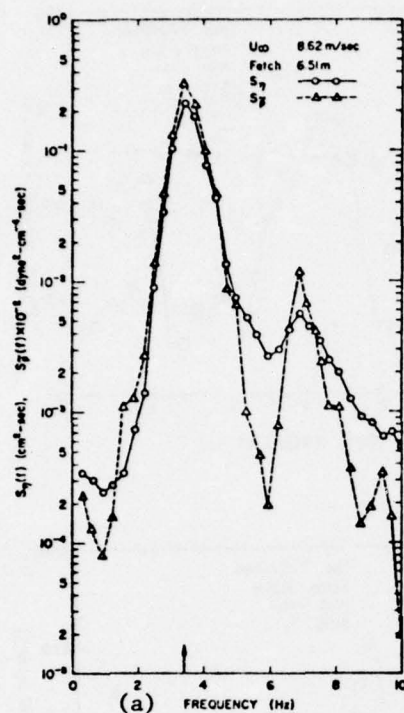
Figure 5.11 Power spectra of wave-induced pressure p̃ and velocity
components ũ and ṽ, and spectra of coherence (R) and
phase angle (θ) between p̃, ũ, ṽ and η at fetch of
6.51 m and wind speed of 8.62 m/sec
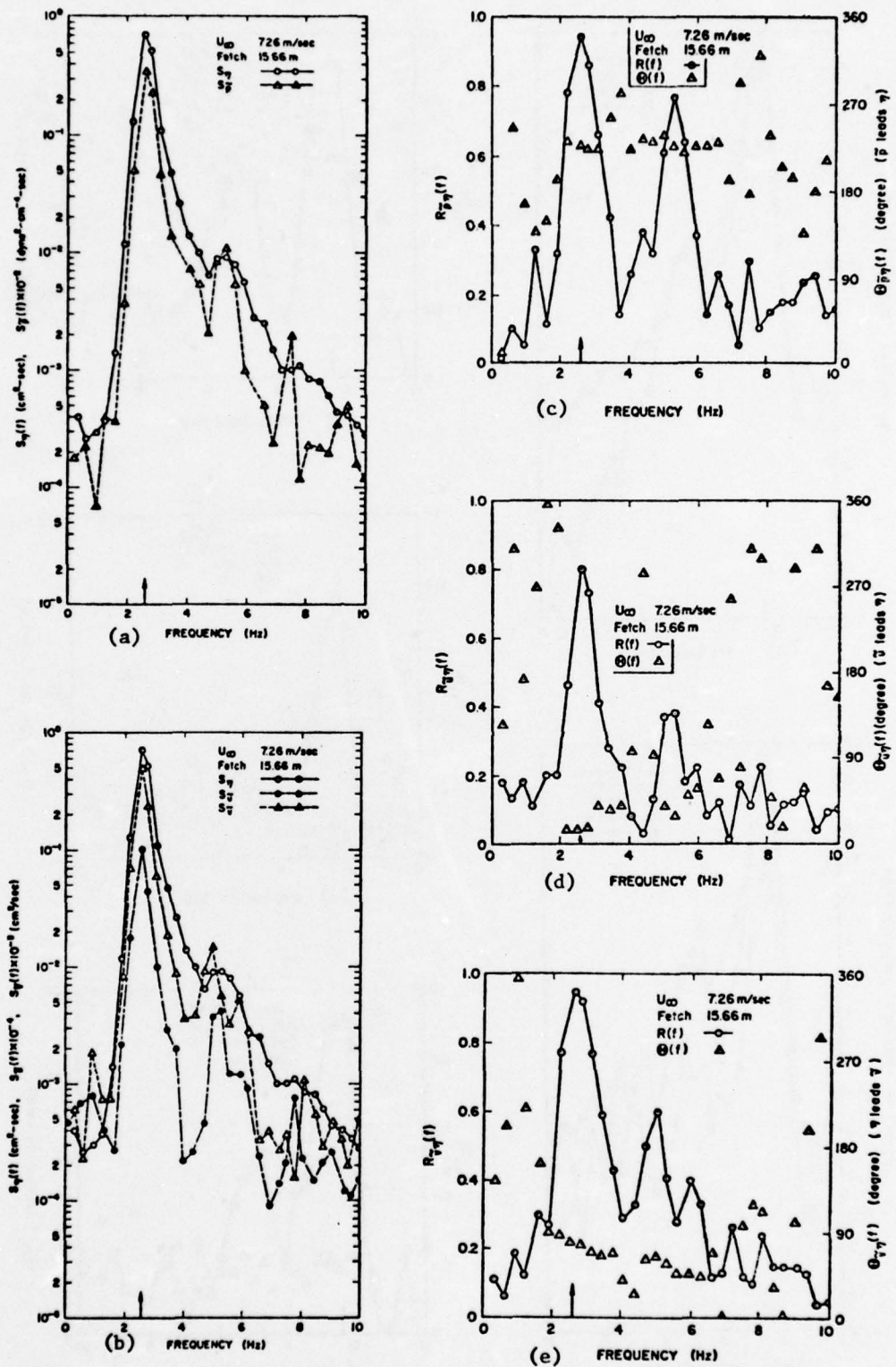
Figure 5.12   Power spectra of wave-induced pressure $\tilde{p}$ and velocity components $\tilde{u}$ and $\tilde{v}$, and spectra of coherence (R) and phase angle (θ) between $\tilde{p}$, $\tilde{u}$, $\tilde{v}$ and η at fetch of 15.66 m and wind speed of 7.26 m/sec
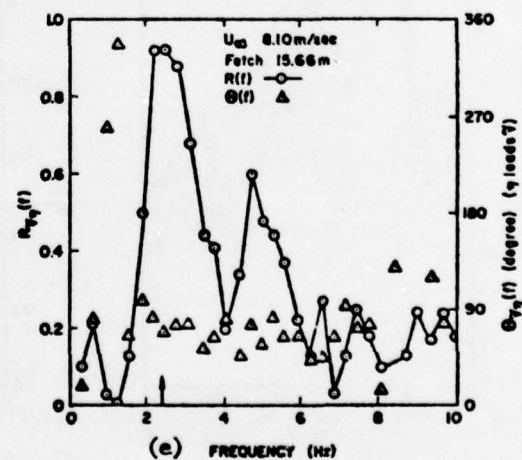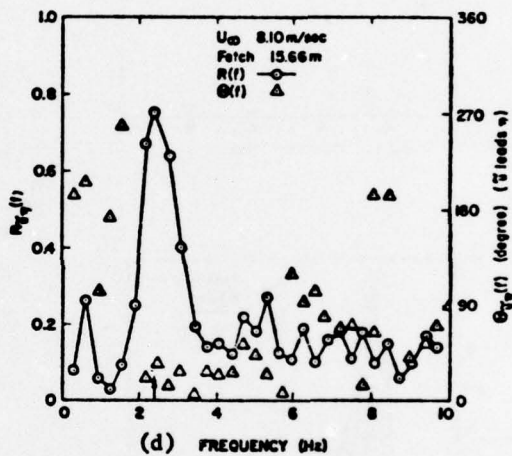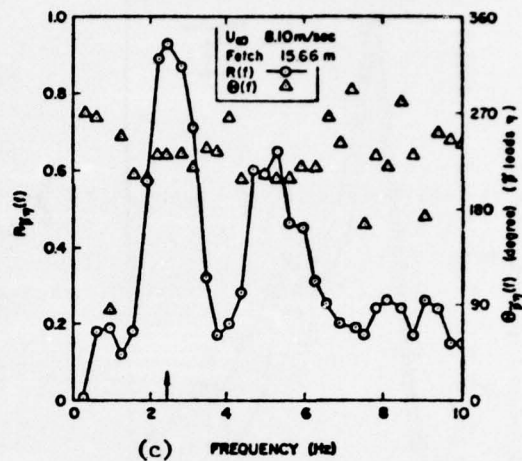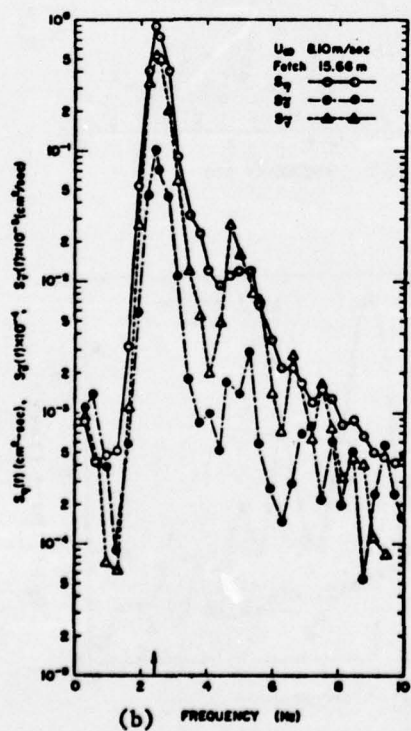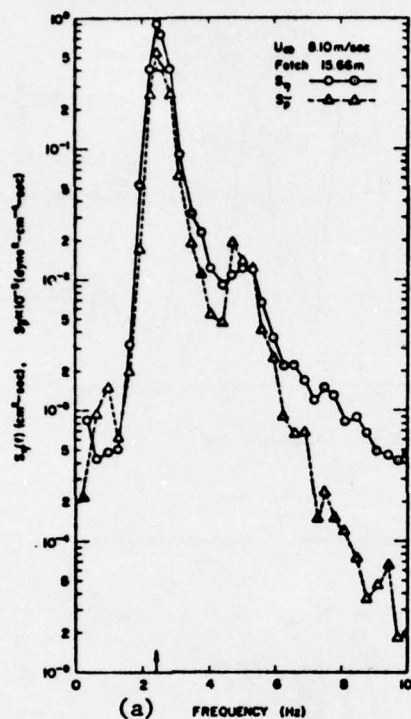
Figure 5.13   Power spectra of wave-induced pressure $\tilde{p}$ and velocity components $\tilde{u}$ and $\tilde{v}$, and spectra of coherence (R) and phase angle (θ) between $\tilde{p}$, $\tilde{u}$, $\tilde{v}$ and η at fetch of 15.66 m and wind speed of 8.10 m/sec
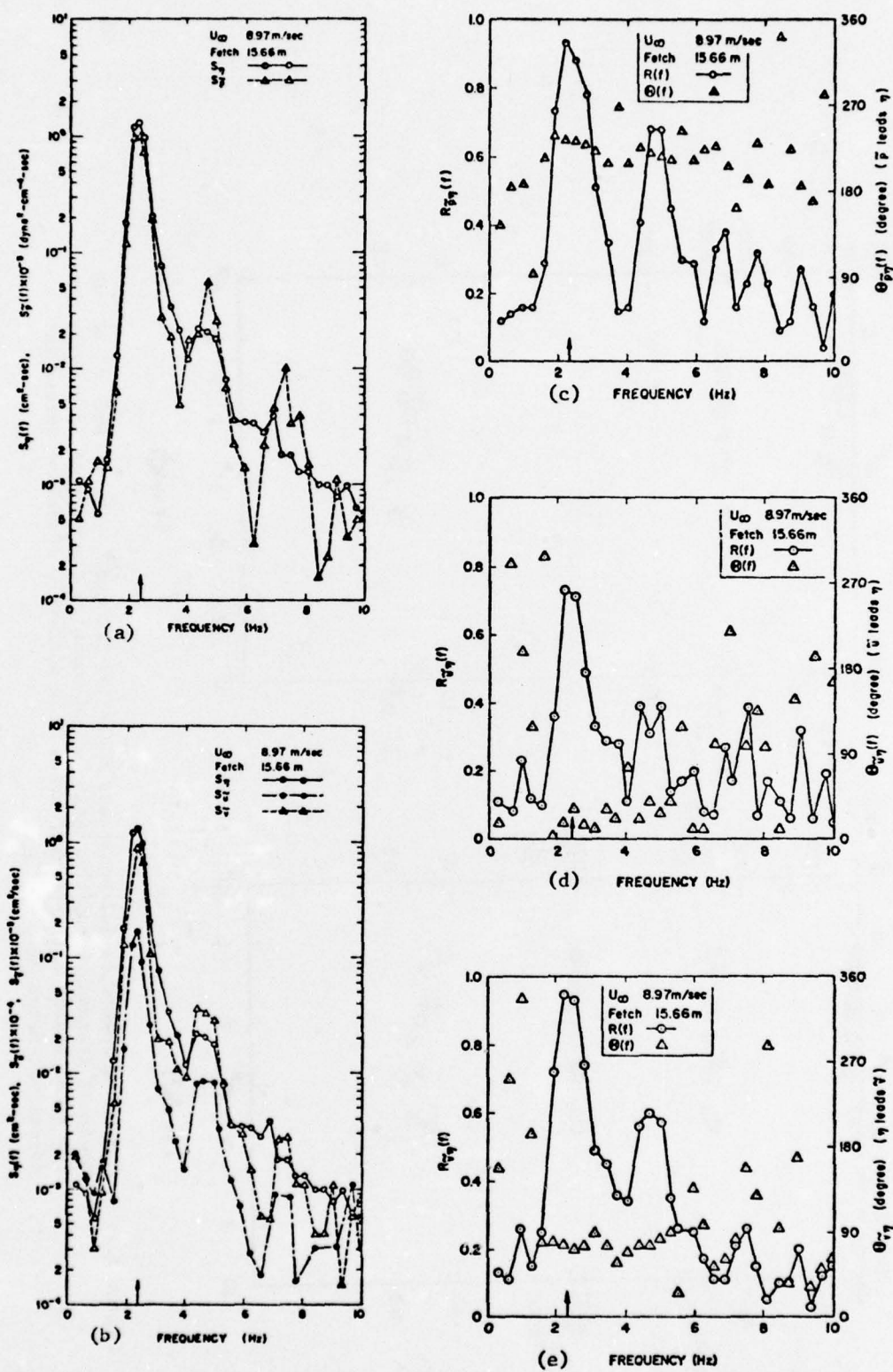
Figure 5.14 Power spectra of wave-induced pressure $\tilde{p}$ and velocity components $\tilde{u}$ and $\tilde{v}$, and spectra of coherence (R) and phase angle (θ) between $\tilde{p}$, $\tilde{u}$, $\tilde{v}$ and η at fetch of 15.66 m and wind speed of 8.97 m/sec

-141-
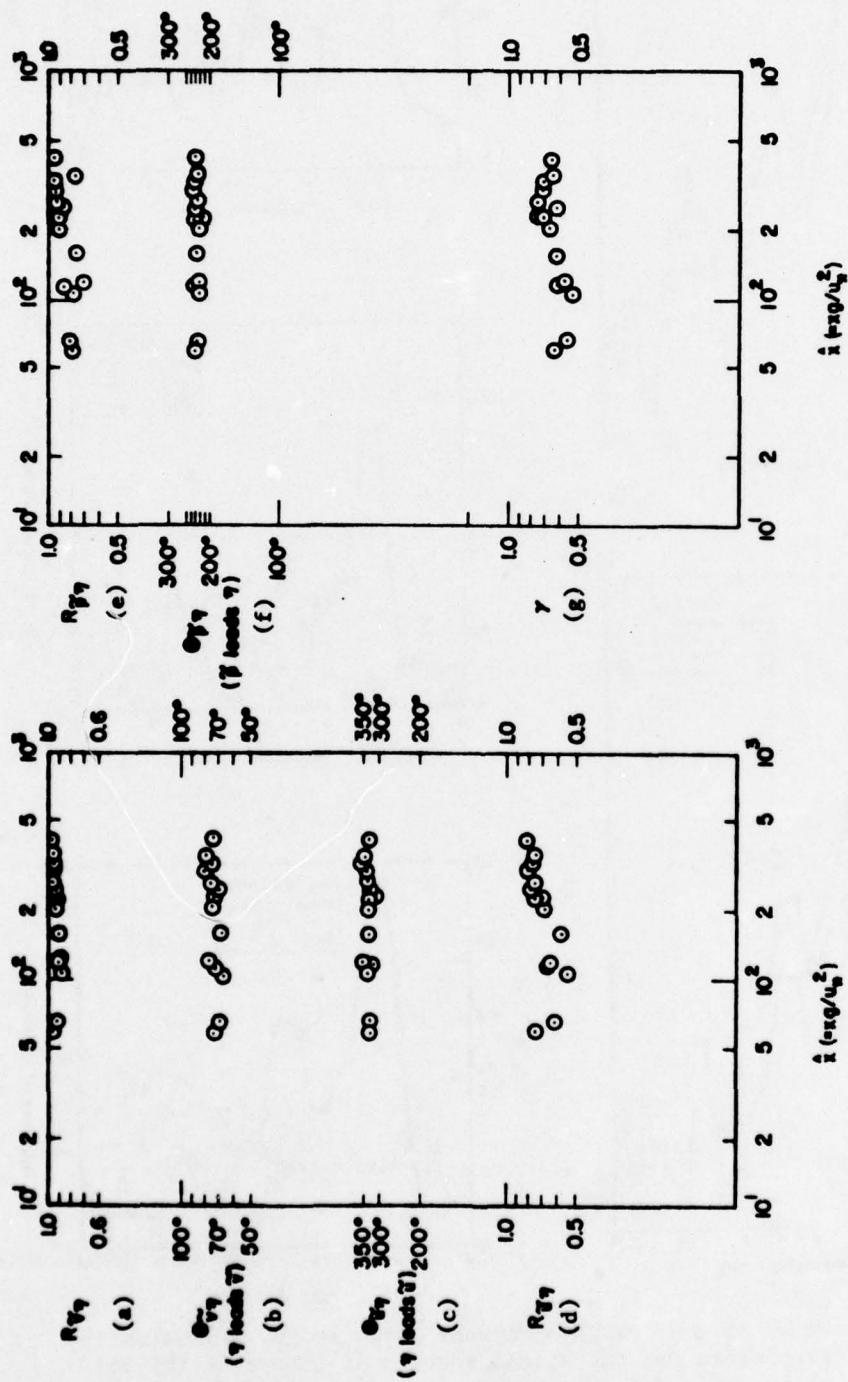
Figure 5.15 Curves of coherence (R) and phase angle (θ) between $\tilde{p}$, $\tilde{u}$, $\tilde{v}$ and η at the dominant frequency, and the ratio γ of momentum transferred into waves over the total momentum transferred across the wind-wave interface versus the normalized fetch $\hat{x}$
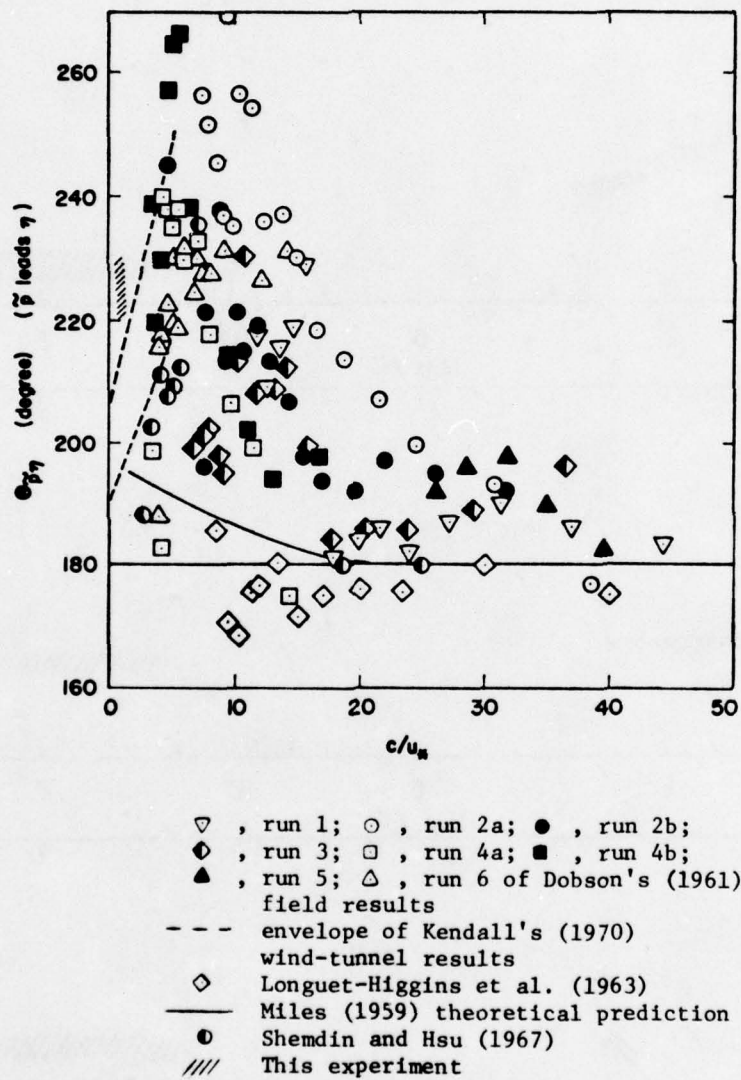
Figure 5.16   Comparisons of the present (////) and previous
results of phase angle between $\tilde{p}$ and η
(after Dobson, 1971)
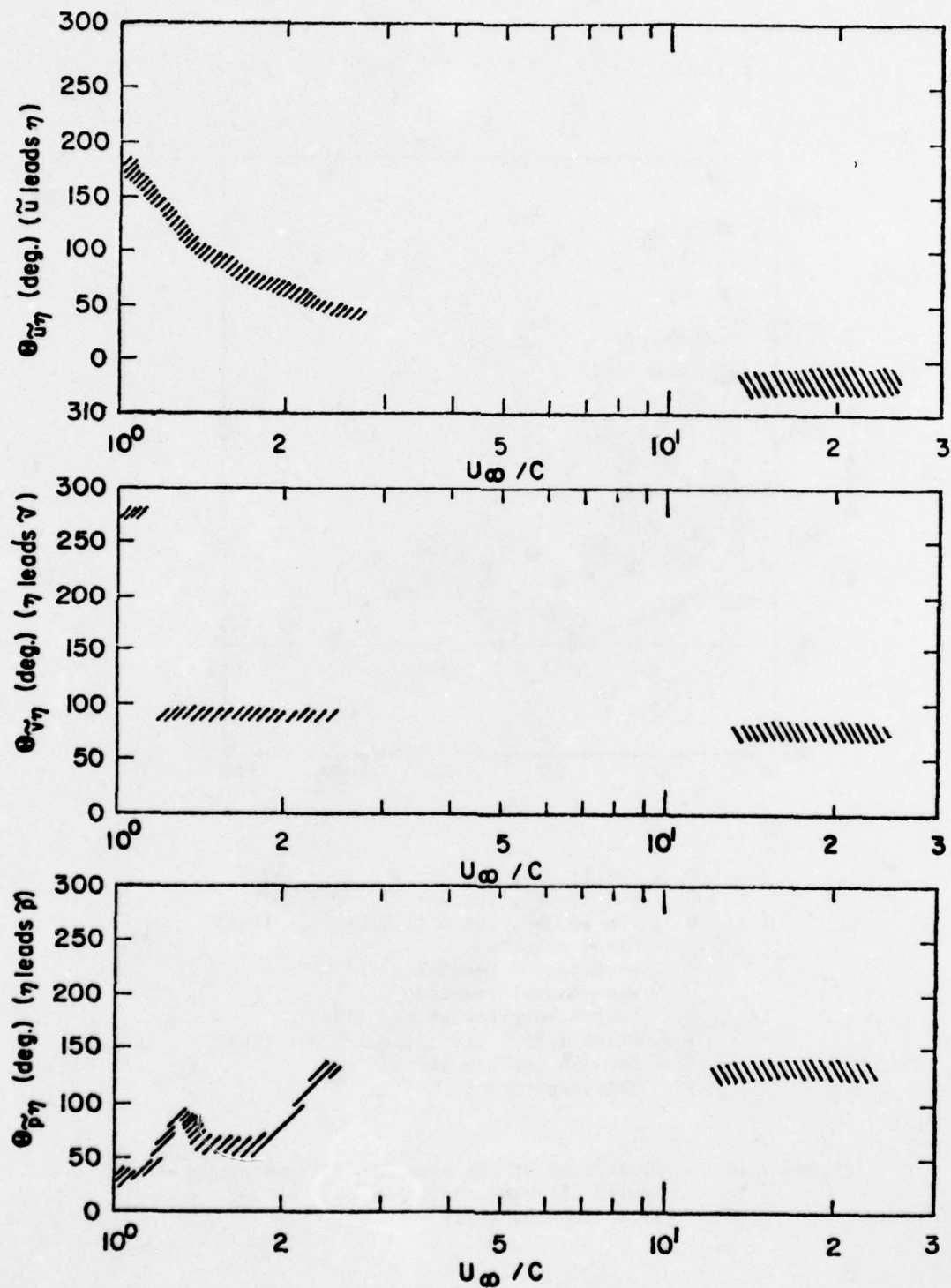
Figure 5.17   Comparisons of the present (\\\) and Yu's (///) results of
phase angle between $\tilde{p}$, $\tilde{u}$, $\tilde{v}$ and η (after Yu, et al.,
1973)
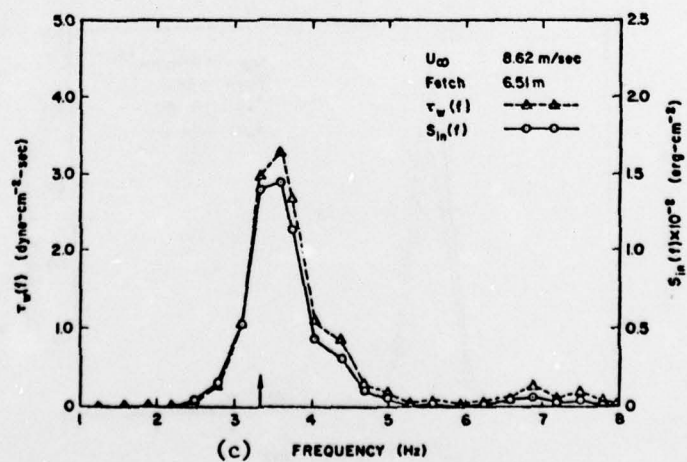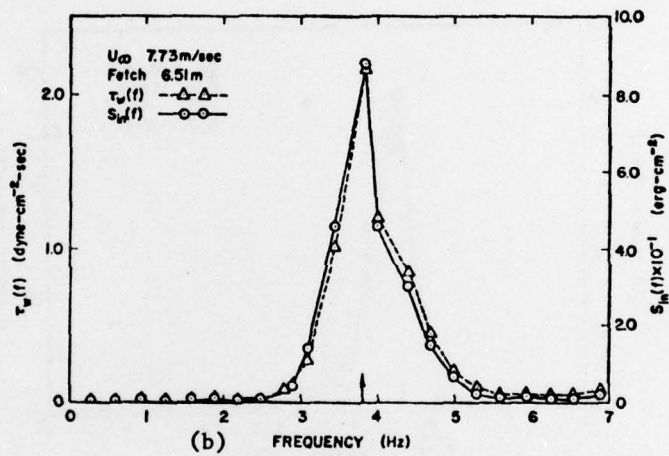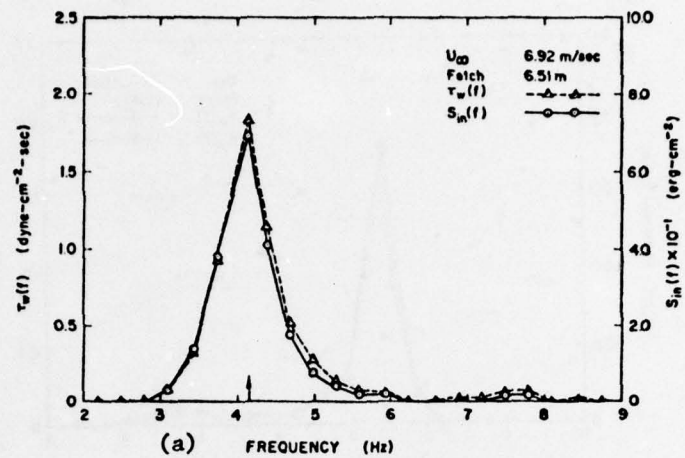
Figure 5.18   Spectra of energy and momentum transfer from wind to
waves due to normal pressure acting on water surface
at fetch of 6.51 m for wind speeds of   (a) 6.92,
(b) 7.73 and (c) 8.62 m/sec

-145-
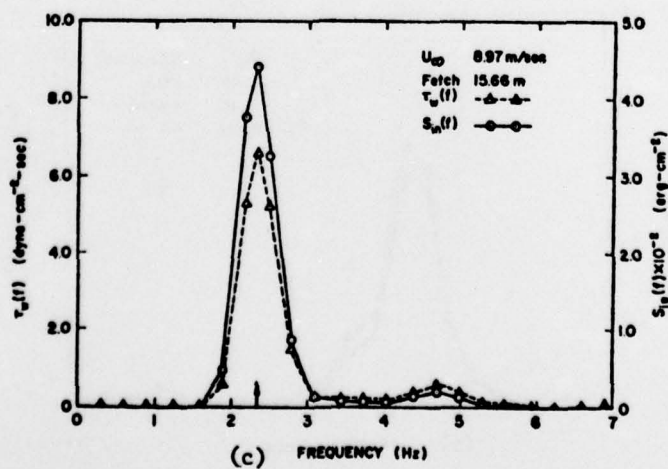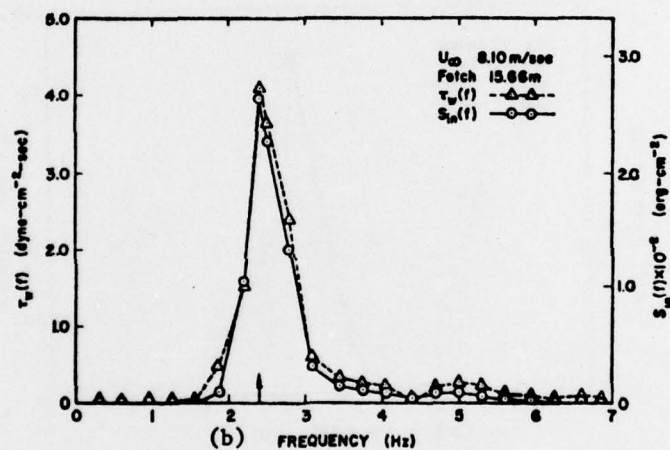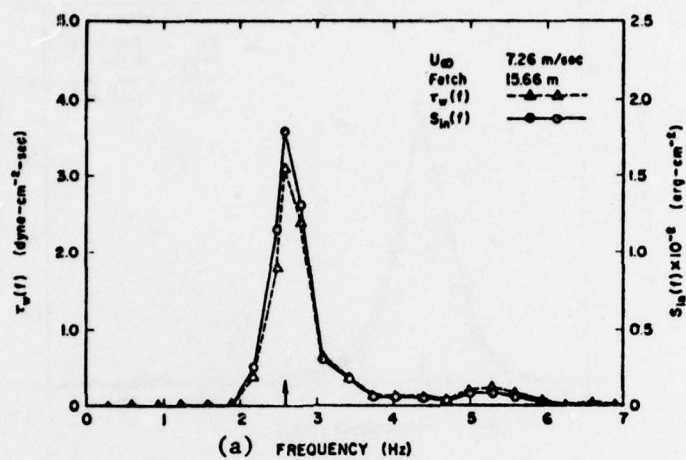
Figure 5.19   Spectra of energy and momentum transfer from wind to waves
due to normal pressure acting on water surface at fetch
15.66 m for wind speeds of   (a) 7.26,   (b) 8.10   and
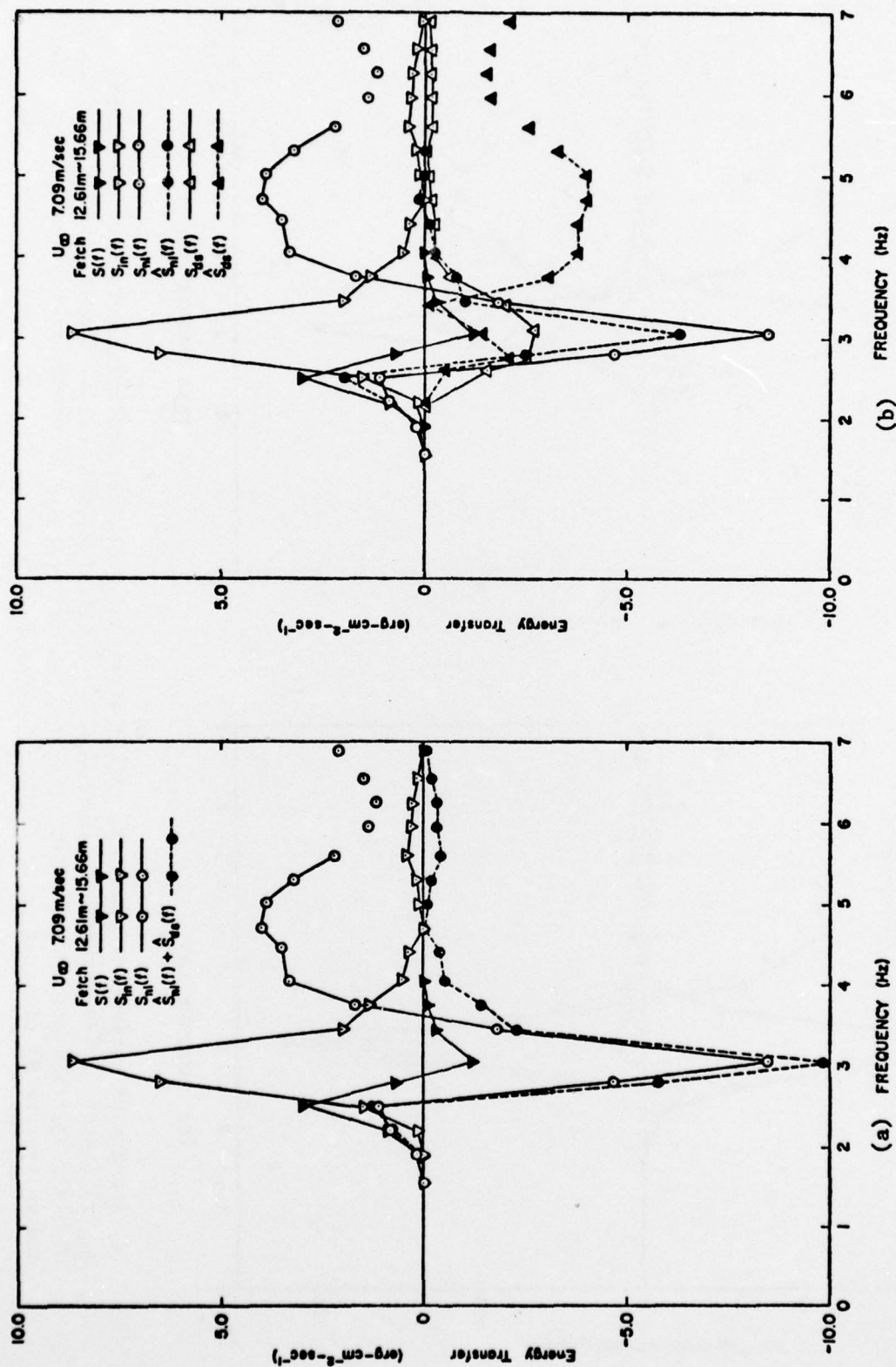(c) 8.97 m/sec
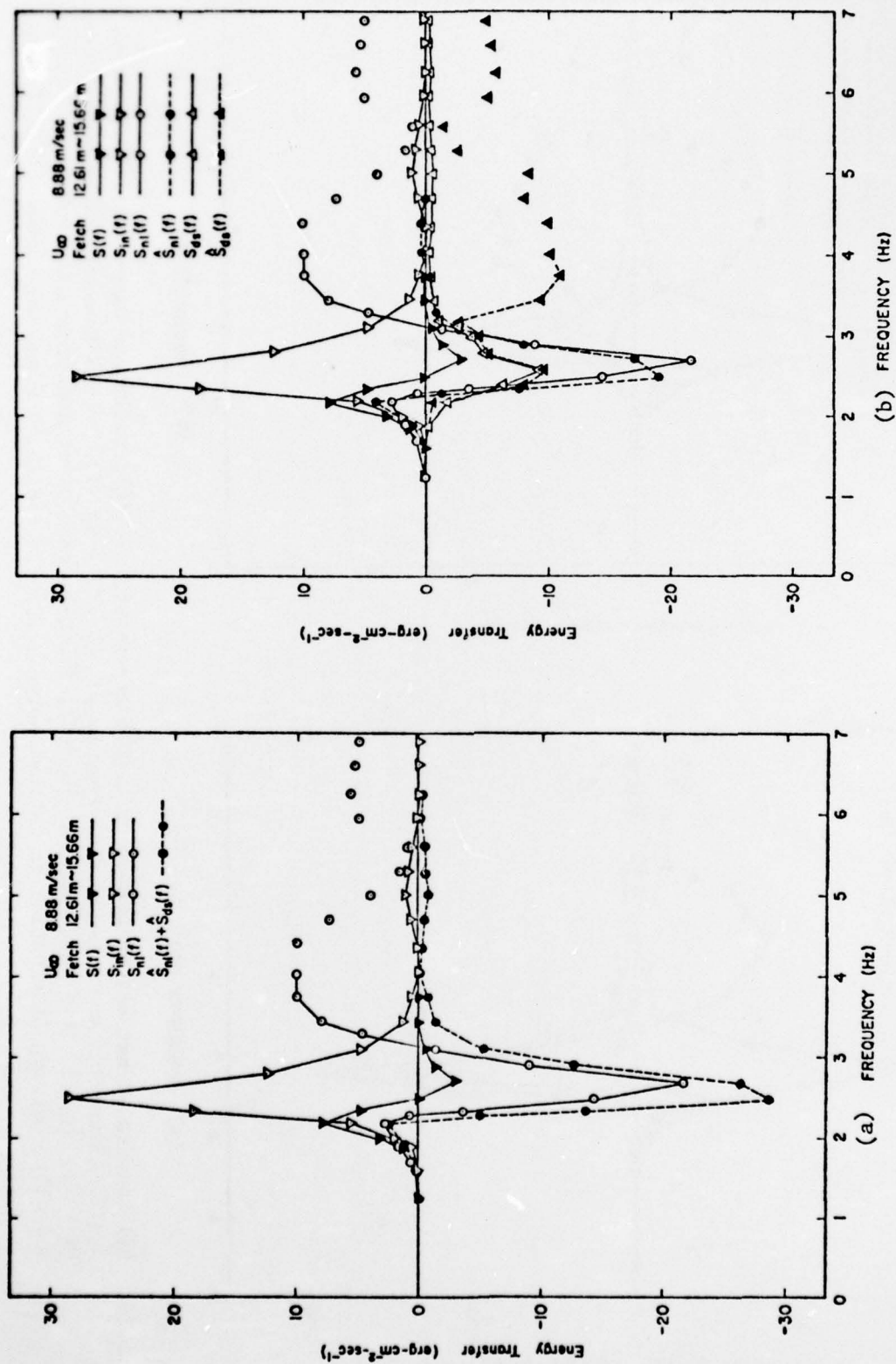
Figure 5.20 (a) Spectra of net energy transfer, $S(f)$; air-input, $S_{in}(f)$; nonlinear wave-wave interactions, $S_{nl}(f)$ [Barnett]; and experimental results of $\hat{S}_{nl}(f) + \hat{S}_{ds}(f)$. (b) Comparisons between theoretical $[S_{nl}(f), S_{ds}(f)]$ and experimental $[\hat{S}_{nl}(f), \hat{S}_{ds}(f)]$ results of nonlinear wave-wave interactions and white-capping dissipation at fetches between 12.61 m and 15.66 m and wind speed of 8.88 m/sec
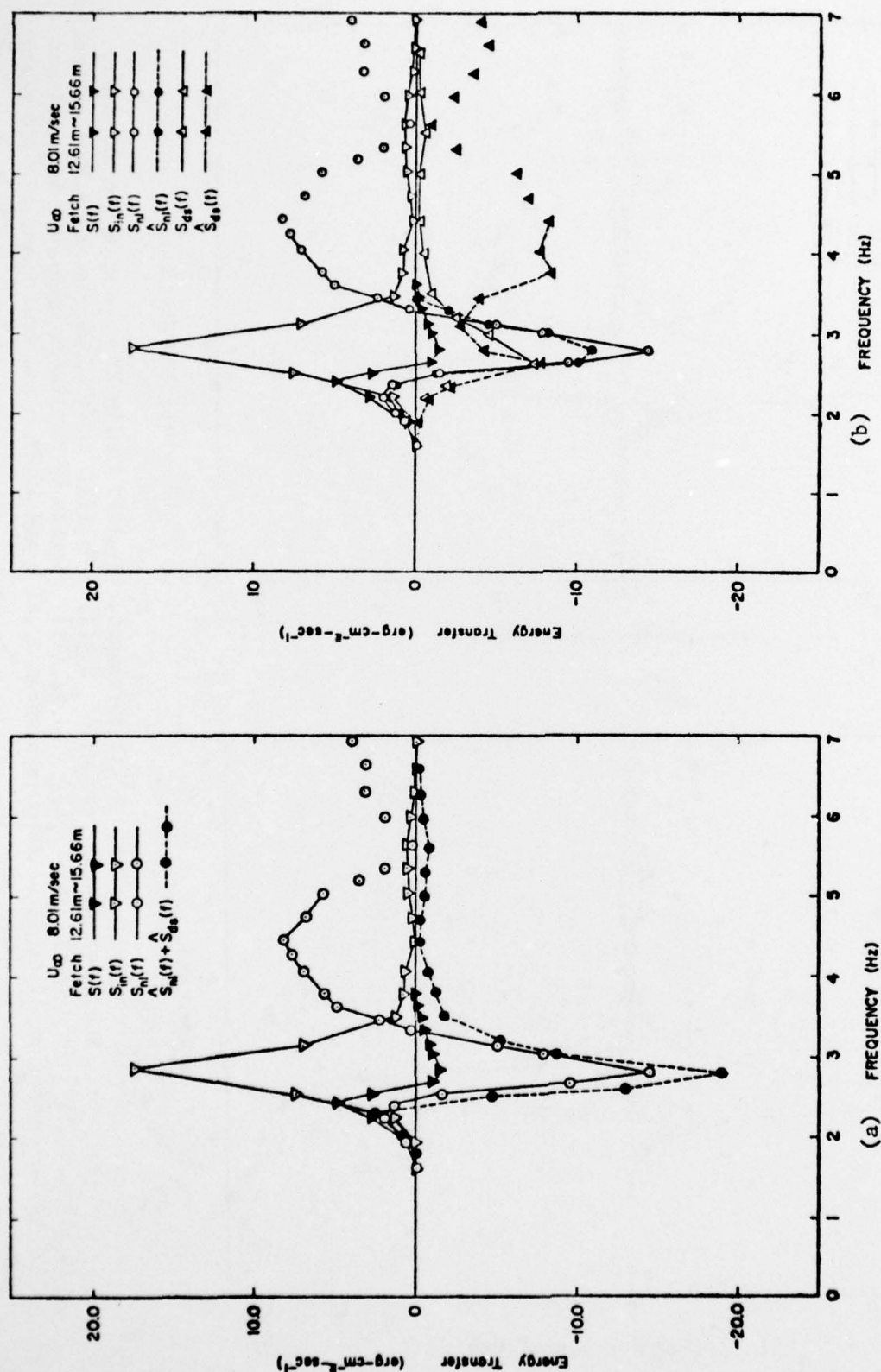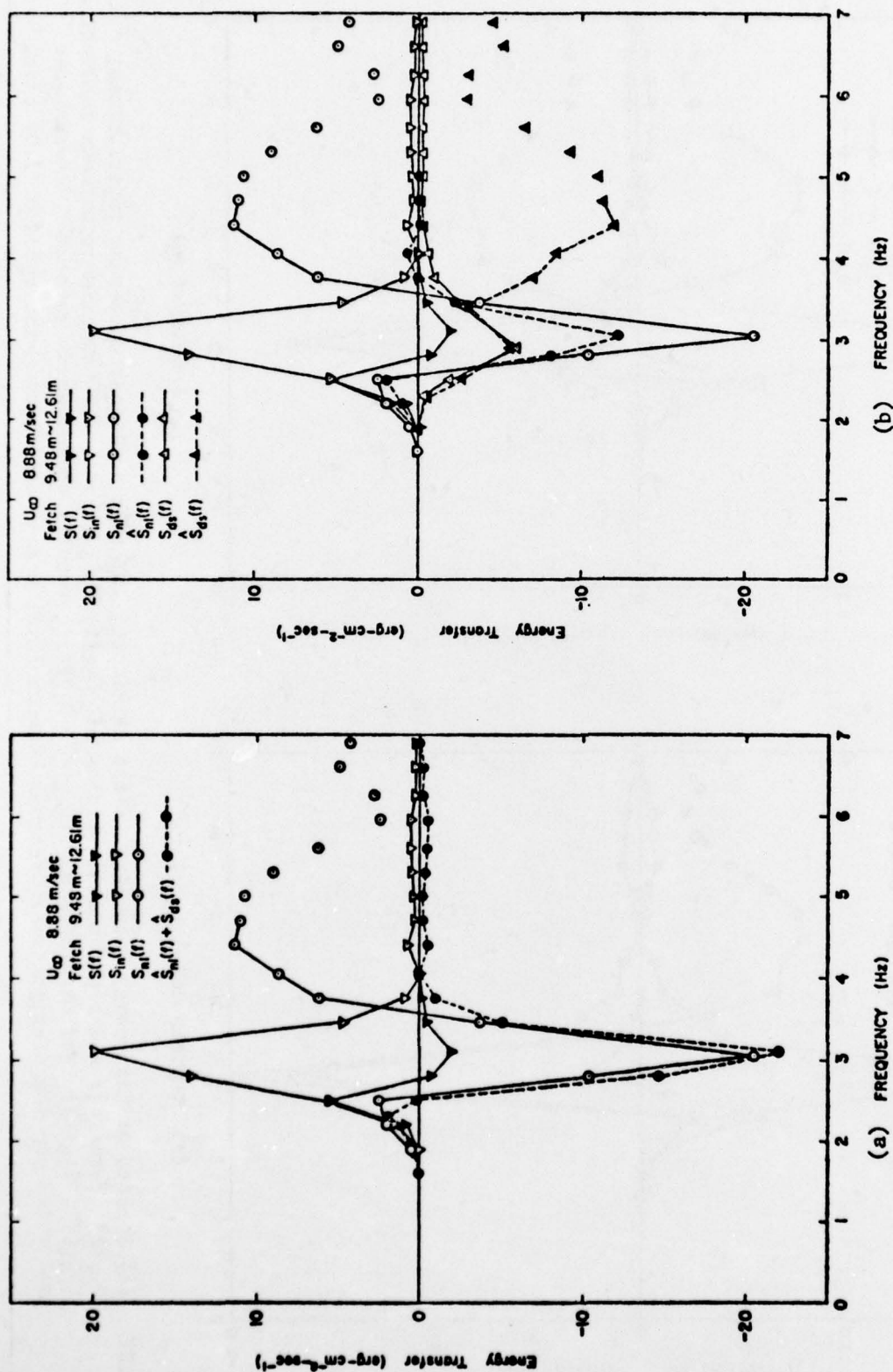
Figure 5.21   (a) Spectra of net energy transfer, S(f); air-input, $S_{in}(f)$; nonlinear wave-wave interactions, $S_{nl}(f)$ [Barnett]; and experimental results of $\hat{S}_{nl}(f) + \hat{S}_{ds}(f)$.   (b) Comparisons between theoretical [$S_{nl}(f)$, $S_{ds}(f)$] and experimental [$\hat{S}_{nl}(f)$, $\hat{S}_{ds}(f)$] results of nonlinear wave-wave interactions and white-capping dissipation at fetches between 12.61 m and 15.66 m and wind speed of 8.01 m/sec
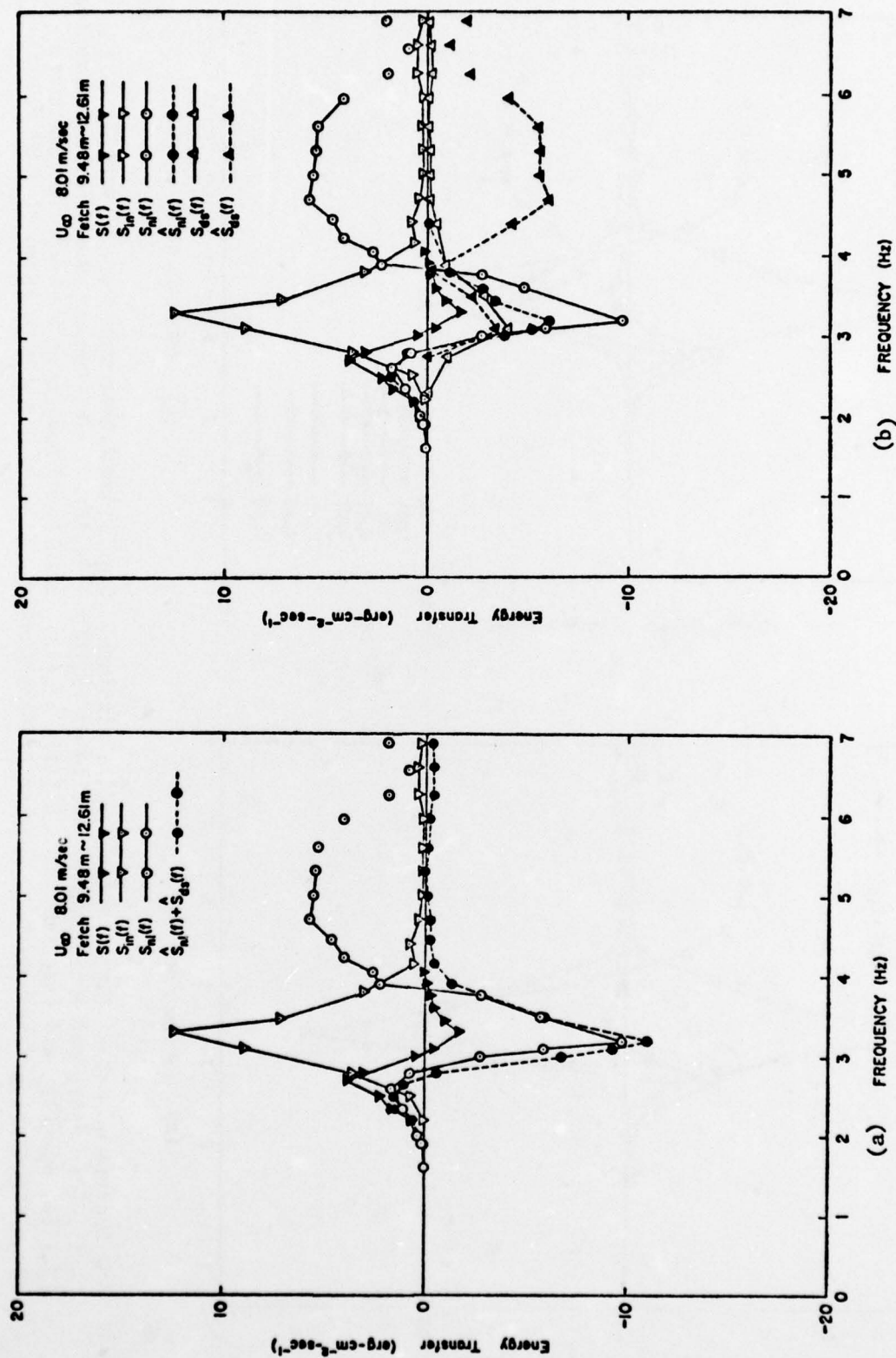
Figure 5.22 (a) Spectra of net energy transfer, $S(f)$; air-input, $S_{in}(f)$; nonlinear wave-wave interactions, $S_{nl}(f)$ [Barnett]; and experimental results of $\hat{S}_{nl}(f)$, $\hat{S}_{ds}(f)$. (b) Comparisons between theoretical $[\hat{S}_{nl}(f), \hat{S}_{ds}(f)]$ and experimental $[\hat{S}_{nl}(f), \hat{S}_{ds}(f)]$ results of nonlinear wave-wave interactions and white-capping dissipation at fetches between 12.61 m and 15.66 m and wind speed of 7.09 m/sec
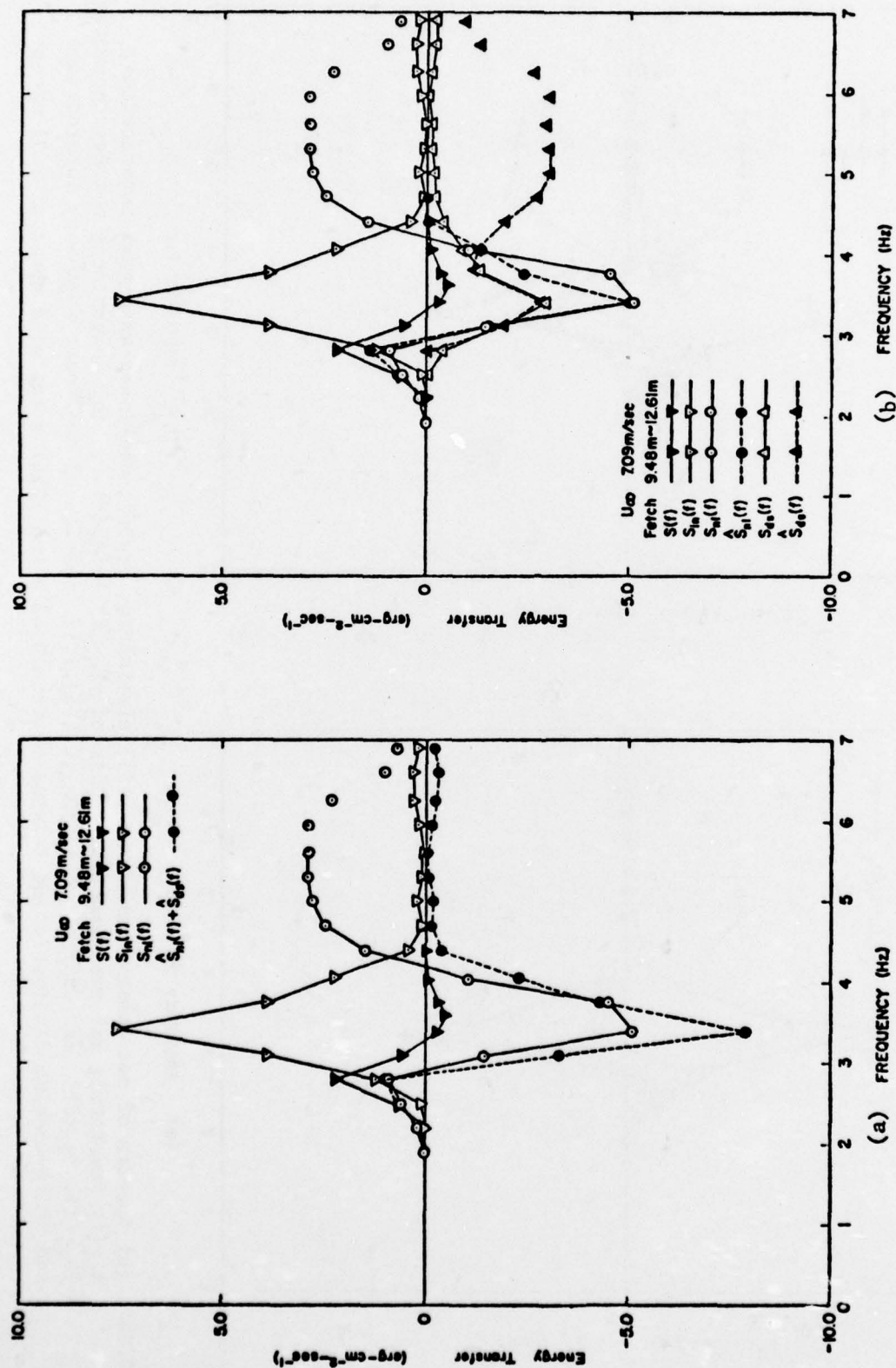
Figure 5.23 (a) Spectra of net energy transfer, S(f); air-input, $S_{in}(f)$; nonlinear wave-wave interactions, $S_{nl}(f)$ [Barnett] ;and experimental results of $\hat{S}_{nl}(f) + \hat{S}_{ds}(f)$. (b) Comparisons between theoretical [$S_{nl}(f)$, $S_{ds}(f)$] and experimental [$\hat{S}_{nl}(f)$, $\hat{S}_{ds}(f)$] results of nonlinear wave-wave interactions and white-capping dissipation at fetches between 9.48 m and 12.61 m and wind speed of 8.88 m/sec

-150-

Figure 5.24 (a) Spectra of net energy transfer, S(f); air-input, $S_{in}(f)$; nonlinear wave-wave interactions, $S_{nl}(f)$ [Barnett]; and experimental results of $\hat{S}_{nl}(f) + \hat{S}_{ds}(f)$. (b) Comparisons between theoretical $[S_{nl}(f), S_{ds}(f)]$ and experimental $[\hat{S}_{nl}(f), \hat{S}_{ds}(f)]$ results of nonlinear wave-wave interactions and white-capping dissipation at fetches between 9.48 m and 12.61 m and wind speed of 8.01 m/sec
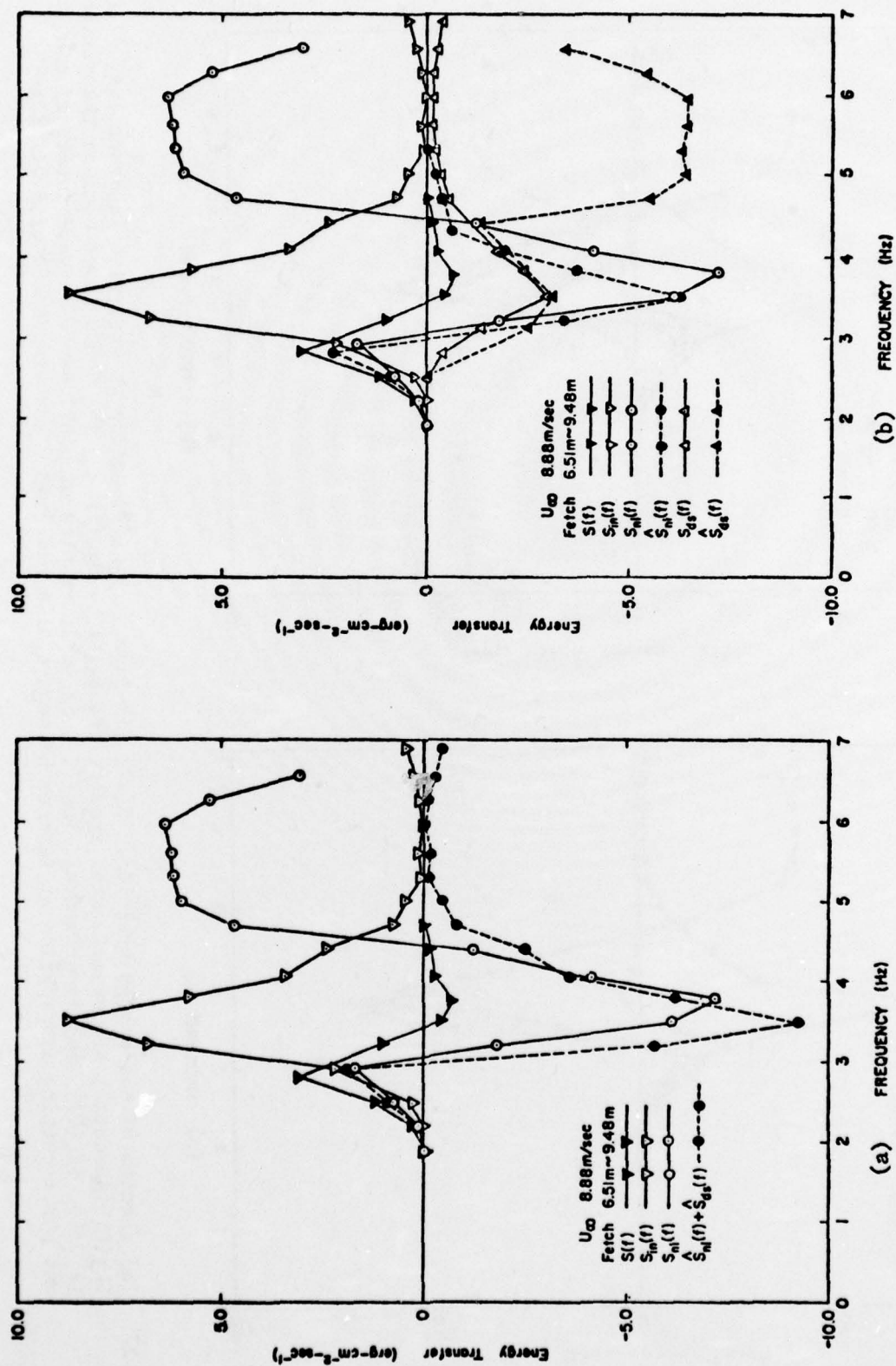
-151-

Figure 5.25 (a) Spectra of net energy transfer, S(f); air-input, $S_{in}(f)$; nonlinear wave-wave interactions, $S_{nl}(f)$ [Barnett]; and experimental results of $\hat{S}_{nl}(f) + \hat{S}_{ds}(f)$. (b) Comparisons between theoretical [$S_{nl}(f)$] and experimental [$\hat{S}_{nl}(f)$, $\hat{S}_{ds}(f)$] results of nonlinear wave-wave interactions and white-capping dissipation at fetches between 9.48 m and 12.61 m and wind speed of 7.09 m/sec
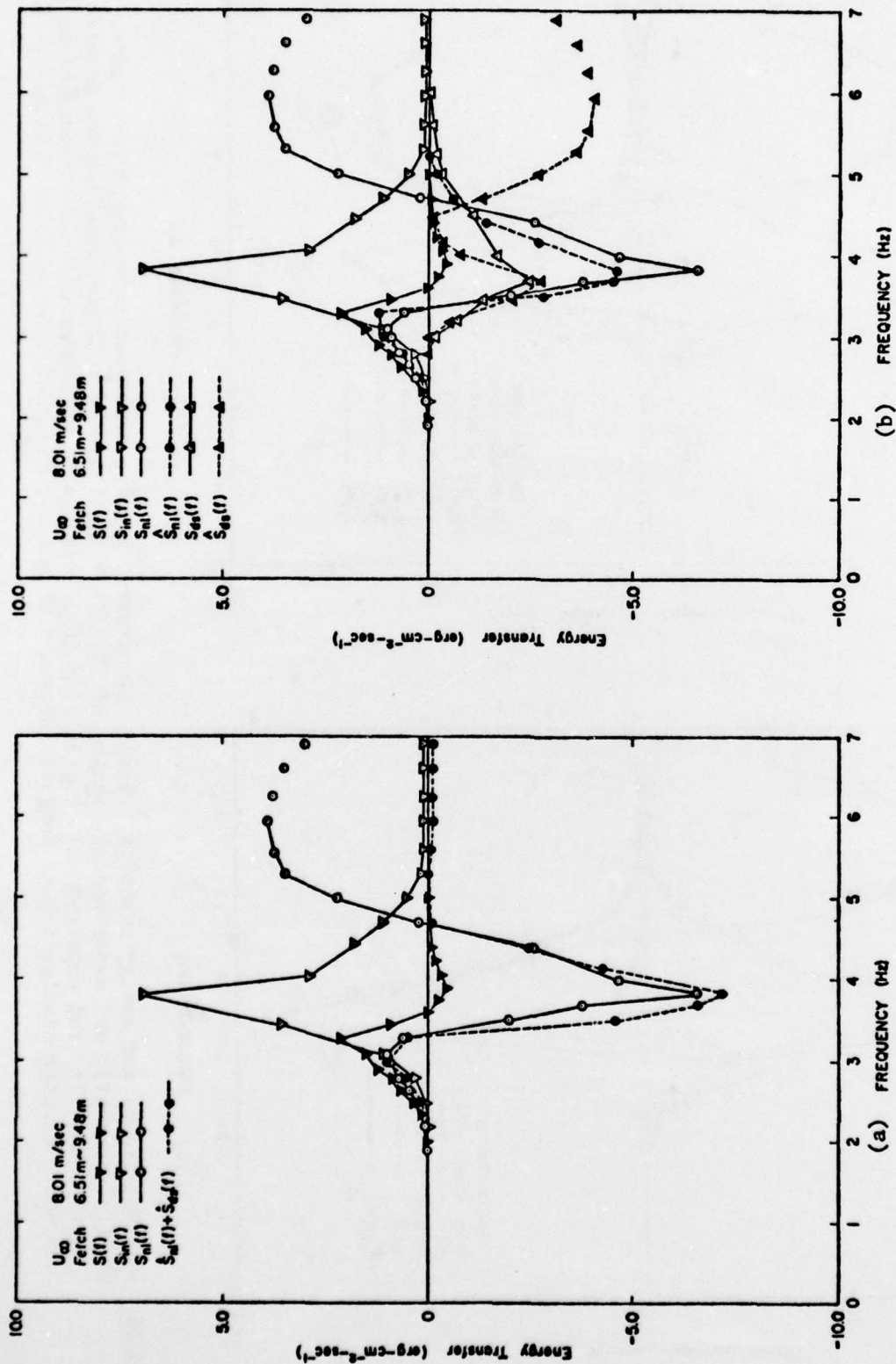
-152-

Figure 5.26 (a) Spectra of net energy transfer, $S(t)$; air-input, $S_{in}(f)$; nonlinear wave-wave interactions, $S_{nl}(f)$ [Barnett]; and experimental results of $\hat{S}_{nl}(f) + \hat{S}_{ds}(f)$. (b) Comparisons between theoretical $[S_{nl}(f), S_{ds}(f)]$ and experimental $[\hat{S}_{nl}(f), \hat{S}_{ds}(f)]$ results of nonlinear wave-wave interactions and white-capping dissipation at fetches between 6.51 m and 9.48 m and wind speed of 8.88 m/sec
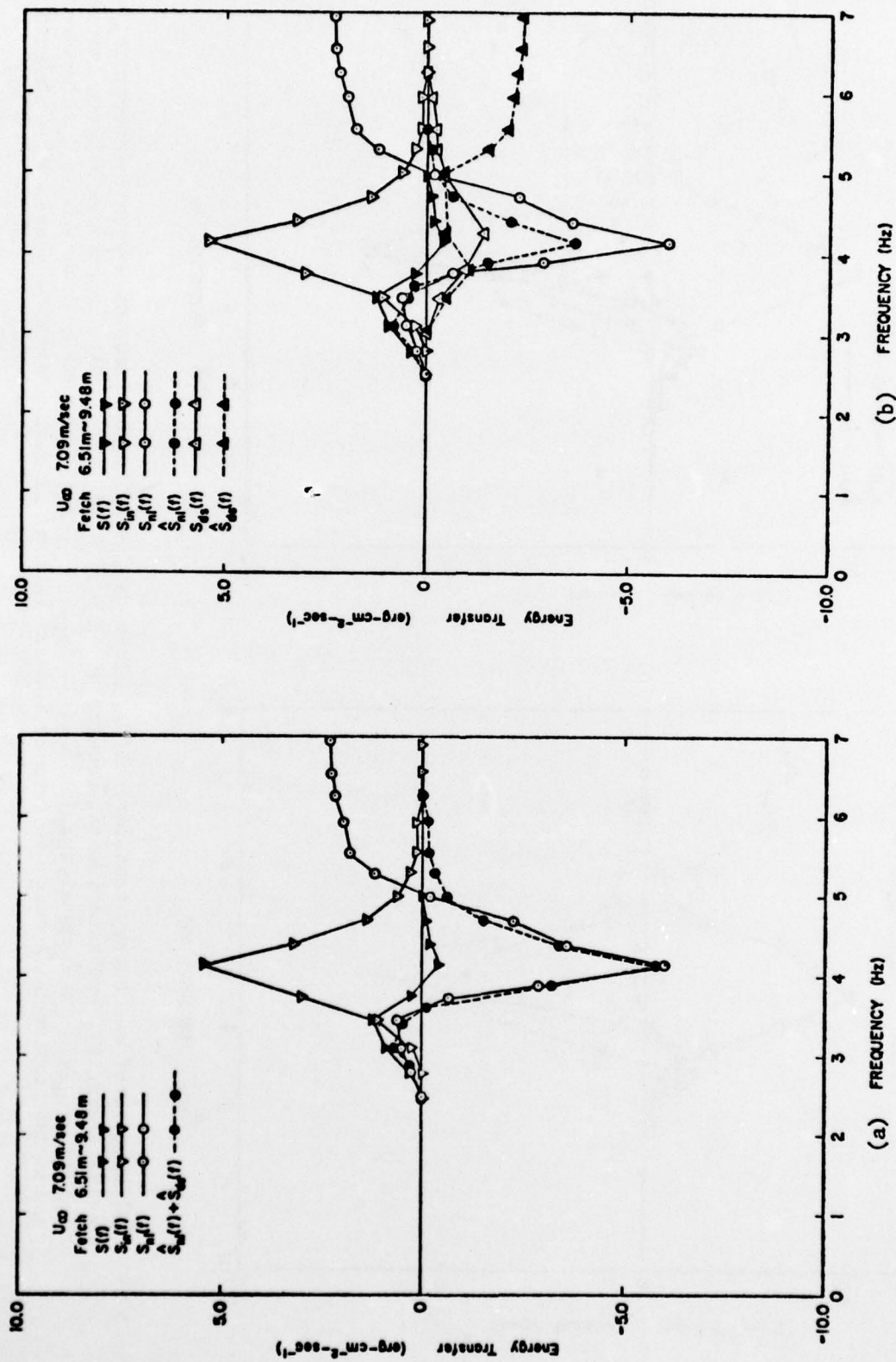
Figure 5.27   (a) Spectra of net energy transfer, S(f); air-input, $S_{in}(f)$; nonlinear wave-wave interactions, $S_{nl}(f)$ [Barnett]; and experimental results of $\hat{S}_{nl}(f) + \hat{S}_{ds}(f)$.   (b) Comparisons between theoretical $[S_{nl}(f), S_{ds}(f)]$ and experimental $[\hat{S}_{nl}(f), \hat{S}_{ds}(f)]$ results of nonlinear wave-wave interactions and white-capping dissipation at fetches between 6.51 m and 9.48 m and wind speed of 8.01 m/sec

-154-

Figure 5.28 (a) Spectra of net energy transfer, S(f); air-input, $S_{in}(f)$; nonlinear wave-wave interactions, $S_{nl}(f)$ [Barnett]; and experimental results of $\hat{S}_{nl}(f) + Sds(f)$. (b) Comparisons between theoretical [$S_{nl}(f)$, $Sds(f)$] and experimental [$\hat{S}_{nl}(f)$, $\hat{S}_{ds}(f)$] results of nonlinear wave-wave interactions and white-capping dissipation at fetches between 6.51 m and 9.48 m and wind speed of 7.09 m/sec
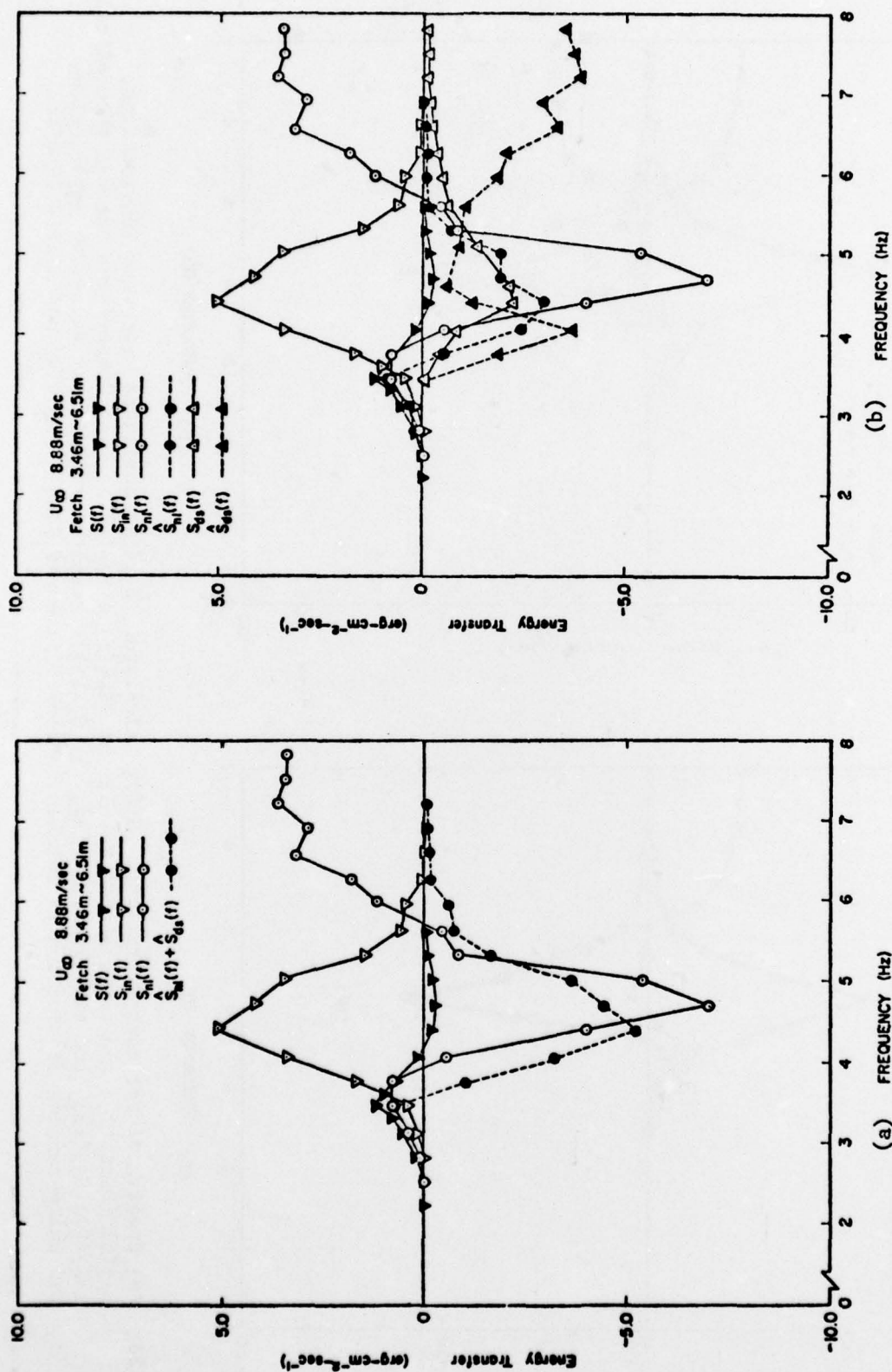
-155-

Figure 5.29 (a) Spectra of net energy transfer, $S(f)$; air-input, $S_{in}(f)$; nonlinear wave-wave interactions, $S_{nl}(f)$ [Barnett]; and experimental results of $\hat{S}_{nl}(f) + \hat{S}_{ds}(f)$. (b) Comparisons between theoretical [$S_{nl}(f)$, $S_{ds}(f)$] and experimental [$\hat{S}_{nl}(f)$, $\hat{S}_{ds}(f)$] results of nonlinear wave-wave interactions and white-capping dissipation at fetches between 3.46 m and 6.51 m and wind speed of 8.88 m/sec
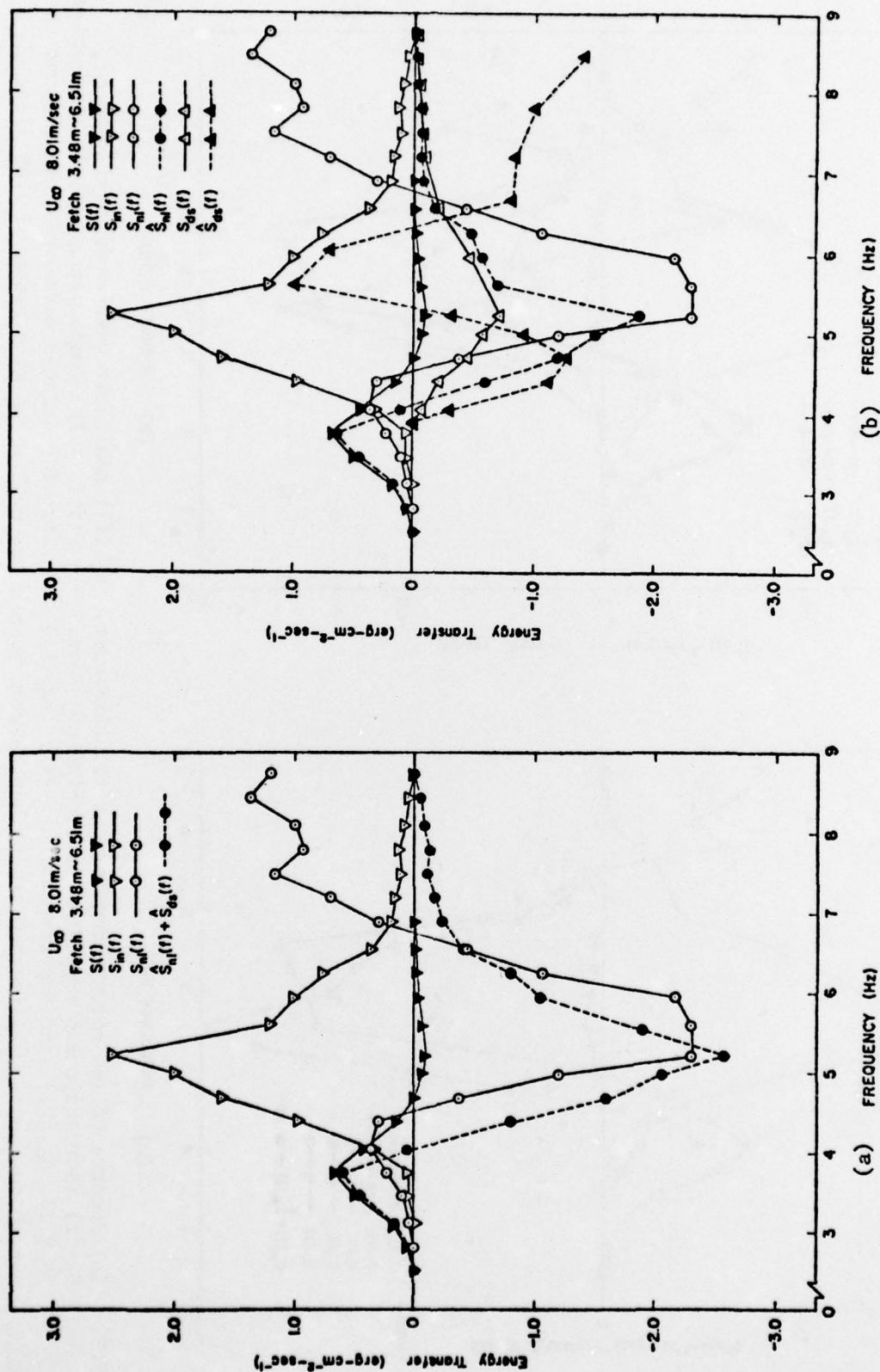
-156-

Figure 5.30 (a) Spectra of net energy transfer, $S(f)$; air-input, $S_{in}(f)$; nonlinear wave-wave interactions, $S_{nl}(f)$ [Barnett]; and experimental results of $\hat{S}_{nl}(f) + \hat{S}_{ds}(f)$. (b) Comparisons between theoretical $[S_{nl}(f), S_{ds}(f)]$ and experimental $[\hat{S}_{nl}(f), \hat{S}_{ds}(f)]$ results of nonlinear wave-wave interactions and white-capping dissipation at fetches between 3.46 m and 6.51 m and wind speed of 8.01 m/sec
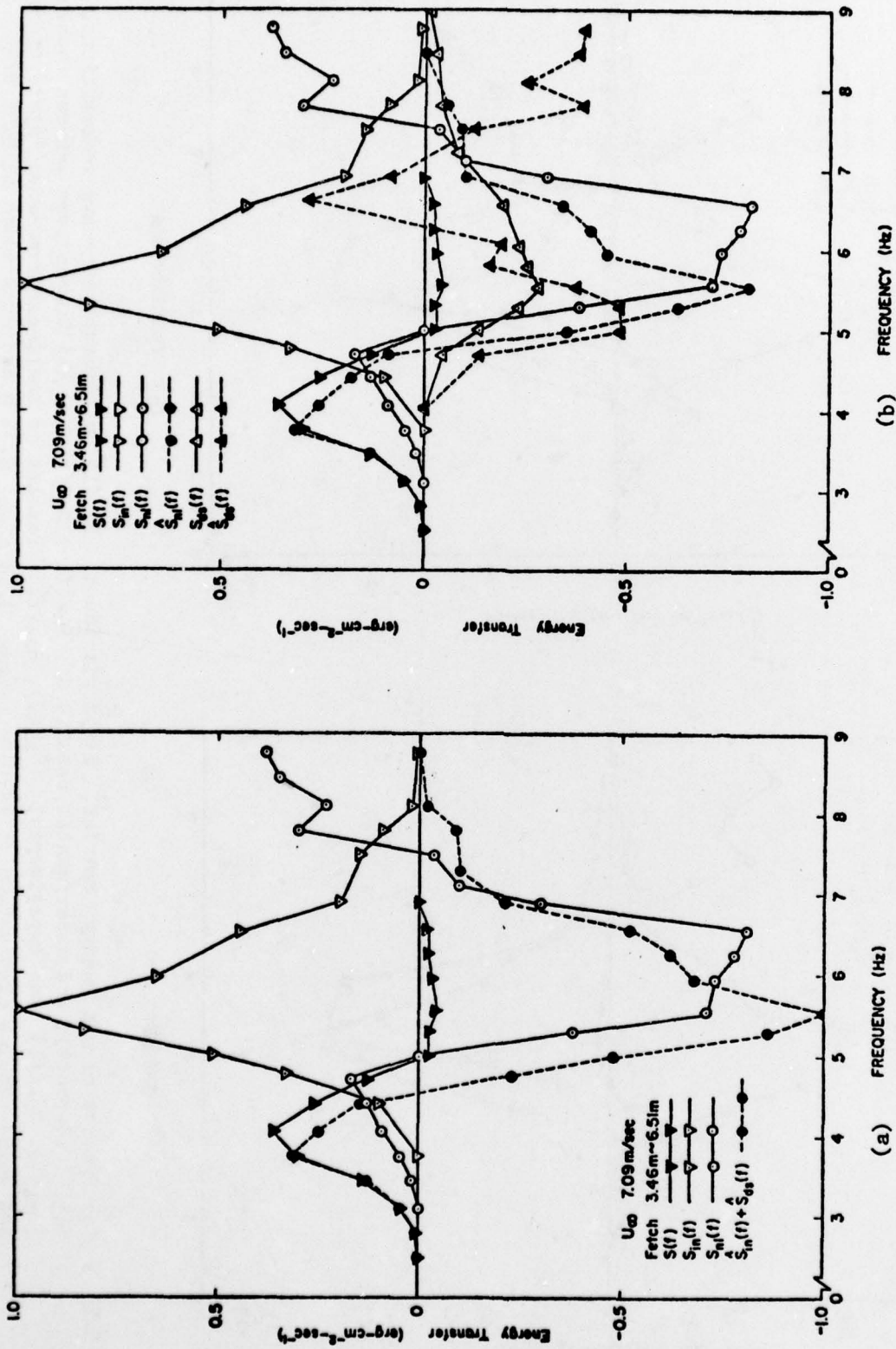
Figure 5.31 (a) Spectra of net energy transfer, $S(f)$; air-input, $S_{in}(f)$; nonlinear wave-wave interactions, $S_{nl}(f)$ [Barnett]; and experimental results of $\hat{S}_{nl}(f) + \hat{S}_{ds}(f)$. (b) Comparisons between theoretical [$S_{nl}(f)$, $S_{ds}(f)$] and experimental [$\hat{S}_{nl}(f)$, $\hat{S}_{ds}(f)$] results of nonlinear wave-wave interactions and white-capping dissipation at fetches between 3.46 m and 6.51 m and wind speed of 7.09 m/sec

-158-